

In compliance with the
Canadian Privacy Legislation
some supporting forms
may have been removed from
this dissertation.

While these forms may be included
in the document page count,
their removal does not represent
any loss of content from the dissertation.

**INFLUENCE OF STRUCTURE OF PALLADIUM AND NICKEL
BASED MEMBRANES ON HYDROGEN PERMEATION**

By

Yang Cao

Department of Mining and Metals and Materials Engineering,

McGill University, Montreal, Quebec, Canada

October, 2002



A thesis submitted to the Faculty of Graduate and Postdoctoral Studies in partial fulfillment of the requirements of the degree of Doctor of Philosophy.

© Yang Cao, 2002.



National Library
of Canada

Bibliothèque nationale
du Canada

Acquisitions and
Bibliographic Services

Acquisitons et
services bibliographiques

395 Wellington Street
Ottawa ON K1A 0N4
Canada

395, rue Wellington
Ottawa ON K1A 0N4
Canada

Your file *Votre référence*

ISBN: 0-612-88432-5

Our file *Notre référence*

ISBN: 0-612-88432-5

The author has granted a non-exclusive licence allowing the National Library of Canada to reproduce, loan, distribute or sell copies of this thesis in microform, paper or electronic formats.

L'auteur a accordé une licence non exclusive permettant à la Bibliothèque nationale du Canada de reproduire, prêter, distribuer ou vendre des copies de cette thèse sous la forme de microfiche/film, de reproduction sur papier ou sur format électronique.

The author retains ownership of the copyright in this thesis. Neither the thesis nor substantial extracts from it may be printed or otherwise reproduced without the author's permission.

L'auteur conserve la propriété du droit d'auteur qui protège cette thèse. Ni la thèse ni des extraits substantiels de celle-ci ne doivent être imprimés ou autrement reproduits sans son autorisation.

Canada

ABSTRACT

The effects of Ni, Pd and Pd₇₇Ag₂₃ alloy membrane microstructures on hydrogen permeation have been investigated using the electrochemical permeation method. Deformation, annealing and electrodeposition have been used to modify the membrane microstructure.

The delay for hydrogen permeation in palladium is increased when the degree of deformation increases. The annealing of deformed palladium and Pd₇₇Ag₂₃ at 250⁰C or 850⁰C accelerates hydrogen diffusion. The annealed metals release hydrogen more rapidly than the deformed metals. The Pd₇₇Ag₂₃ alloy needs more time to release hydrogen. The solubility increases in both palladium and Pd₇₇Ag₂₃ when deformation increases. A hydrogen-trapping model has been developed, which allows the prediction of trends in the experimental data.

The nickel electrodeposits exhibit fiber texture with two components (100) and (110). Low current densities yield a dominant (100) texture. High current densities develop a strong (110) fiber texture. There is a texture transition region between 30 and 50A/dm². After annealing at 800⁰C for 1h, the (100) texture is transformed to (111) texture. Diffusion coefficients increase as texture is transformed from (001) to (011) and (111). The diffusion coefficient of a sample without a dominant texture is lower than the values measured for the samples with (001), (110) and (111) textures. Diffusion coefficients of (001) and (011) polycrystalline membranes are higher than (001) and (011) single crystal membranes. However, in both cases the (011) diffusion coefficient is greater than the (001). By using absorption energies of (001), (011) and (111), the three basic planes in nickel, adsorption energies for other orientations have been estimated using the weighted average method. Adsorption energies for different orientations have been shown in the form of an inverse pole figure.

The diffusivity of hydrogen increases six times from single crystal membranes to polycrystalline membranes, and increases six times again from polycrystalline membranes to nanocrystalline membranes. When nanocrystalline nickel membranes have been annealed between 200⁰C and 900⁰C, they yield a texture change in the nickel membrane from (100) fiber texture to a mixture of (100) fiber texture and (111) texture,

and then only one recrystallization (111) texture component is observed. During annealing from 200⁰C to 900⁰C, a slight increase in the number of high angle (45⁰-65⁰) grain boundaries occurs and a percentage of the low (0⁰-15⁰) and middle angle (30⁰-45⁰) grain boundaries decreases slightly. After annealing at 800 ⁰C and 900 ⁰C, changes in the grain size do not affect the rate of diffusion of hydrogen.

There are four major microstructural factors: deformation defects, grain size, texture and grain misorientation, which affect hydrogen permeation in metals. In the polycrystalline materials studied, the importance of crystal defects, grain size, texture and grain misorientation on hydrogen permeation has been established.

In the developed multilayer membranes when hydrogen charging is from the nano-Ni side of the nano-Ni and poly-Ni composite membrane, the permeation current rises rapidly. When hydrogen charging is from the poly-Ni side of the same composite membrane, the permeation current gradually rises and it takes longer to reach a steady state. The permeability of the nano-poly-Ni membranes charging from the nano-Ni side is eight times higher than that of the same composite membrane charging from the poly-Ni side. The diffusivity of the nano-poly-Ni membranes charging from the nano-Ni side is two times higher than that of the same composite membrane charging from the poly-Ni side. The nano-poly-Ni membranes charging from the nano-Ni side release hydrogen faster than the same composite membrane charging from the opposite side. The diffusivity and permeability of the nano-poly-Ni membrane are smaller than those for a single nano-Ni membrane, but larger than those for a single poly-Ni membrane. The hydrogen permeation model for a bilayer membrane is built to simulate diffusion in the nano-Ni layer and the poly-Ni layer. The model can generate concentration profiles of hydrogen. The experimental data are in good qualitative agreement with the model.

RÉSUMÉ

Les effets de la microstructure de membranes d'alliage de Ni, Pd et Pd₇₇Ag₂₃ sur la perméation d'hydrogène ont été étudiés à l'aide de méthode de perméation électrochimiques. La déformation, le recuit et l'électrodéposition on tout été utilisé pour modifier la microstructure de membrane d'alliage de Ni, Pd et Pd₇₇Ag₂₃.

Le retard de perméation hydrogène dans le palladium augmente quand le degré de déformation augmente. Le recuit de palladium déformé et du Pd₇₇Ag₂₃ à 250°C et 850°C accélère la diffusion hydrogène Les métaux recuit dispose plus rapidement hydrogène que les métaux déformés. Le Pd₇₇Ag₂₃ prend plus de temps pour disposé d'hydrogène La solubilité augment dans le palladium et le Pd₇₇Ag₂₃ quand le degré de déformation augmente. Un modèle de trappage hydrogène a été établi qui permet de prédire les tendances dans les résultats expérimentales.

Le nickel électrodéposé à une texture de fibre et comprend deux orientations de (100) et (110). De basses densités de courant mènent à une texture dominante de (100); de hautes densités de courant mene a une texture fibre de (110). Il y a une région de transition entre 30 et 50A/dm². Après un recuit à 800°C pour une heure, la texture de (100) est transformée à une de (111). Les coefficients de diffusion augmentent quand la texture se transforme de (001) à (011) et (111). Le coefficient de diffusion du spécimen sans aucune texture dominante est plus bas que ceux dont la texture est de (001), (011) et (111). Les coefficients de diffusion de membranes poly cristalline de (001) et (011) sont plus élevés que ceux des membranes mono cristallines de même texture. Néanmoins, dans les deux cas précédents, le coefficient de diffusion (011) et plus élevé que celui de (001). En utilisant les énergies d'absorption de (001), (011) et (111), les trois planes élémentaires du nickel, les énergies d'absorption d'autres orientations ont été estimées par la méthode de moyenne pesée. Les énergies d'absorption correspondantes aux orientations respectives ont été illustrées en forme de projection stéréographique inversée.

La diffusion de l'hydrogène augment de six fois an changeant de membrane mono cristalline à une poly cristalline, et six fois encore de poly cristalline à nano cristalline. Quand les membranes nano cristallines de nickel sont recuites entre 200 et 900°C, il y a un changement de texture du fibre (100) à une combinaison de (100) et (111) et après recristallisation, la texture devient uniquement (111). Durant le recuit entre 200 et 900°C,

il y a une augmentation légère de frontière de grain a grand angle (45° - 65°), et une diminution de nombre de frontières de grain a bas (0° - 15°) et moyen (30° - 45°) angle. Après un recuit entre 800°C et 900°C , les changements de grosseur des grains ont aucun effet sur le taux de diffusion d'hydrogène.

Il y a quatre facteurs microstructuraux qui affect la perméation hydrogène dans les métaux: les défauts de déformation, la grosseur des grains, la texture et la mésorientation. Dans le cas des matériaux poly cristallins étudiés, l'importance des défauts, de grosseur des grains, de la texture et de mésorientation sur la perméation d'hydrogène a été établi.

Dans les membranes a couche multiple, quand le chargement hydrogène est fait du coté nano-Ni de la membrane composite nano-Ni et poly-Ni, le courant de perméation augment rapidement. Quand le chargement hydrogène est fait du coté poly-Ni du même composé, le courant de perméation augmente graduellement et prend longtemps avant d'atteindre l'équilibre. La perméabilité de membranes nano-poly-Ni est huit fois plus élevée que celle de poly-nano-nickel. Les membranes nano-poly-Ni relâche plus facilement hydrogène que les membranes poly-nano-Ni. La diffusion de membranes nano-poly-Ni est deux fois plus haute que celles de poly-nano-Ni. La diffusion et perméabilité de membranes nano-poly-Ni sont plus petites que celle de nano-Ni, mais plus grandes que celles de poly-Ni. Un modèle de perméation hydrogène a été construit pour une membrane a deux couches pour simuler la diffusion dans les membranes de nano-Ni et de poly-Ni dans deux directions de chargement. Le modèle peut générer des profils de concentrations hydrogène. Les données expérimentales sont en bon agrément qualitatif avec le modèle proposé.

ACKNOWLEDGEMENTS

First, my great thanks go to my supervisor, Professor J. A. Szpunar, for being a wonderful mentor, for all his guidance, enthusiasm, inspiration, support, and patience. I thank him for being very flexible and understanding.

I appreciate the valuable advice and help from Dr. W. T. Shmayda.

I would like to thank Dr. Hualong Li for stimulating discussion and helping out whenever he could, especially in computer modeling. My appreciations go to Alexandre Blander for his thesis polishing and the French translation of the abstract. Thanks are due to Dr. Frank Czerwinski for some electrodeposit specimens. I wish to thank Dr. G. Palumbo for nanomaterial specimens used in permeation measurements. Thanks are also due to Slavek Poplawski for his assistance with x-ray measurements.

I would like to thank the staff and students from Texture Lab for their friendship and assistance. This includes: Jianlong Lin, Jae-Young Cho, Jongtae Park, Baekyun Kim, Brain Morris, Kitae Lee, Askar Sheikh-Ali, Vladimir Basabe, Raj Narayanan, Kabir Mirpuri, Neil D'Souza, Byeouny-Soo Ahn, Andy Wen, Xiaohuai Cao, Hotae Jeong, Raed Hasaisheh, James Vaugh, Jae-Young Park, Seongjun Park, Peter Blandford, Mike Glavicic, Val Gertsman and Sasha Zhilyaev.

I also would like to thank Hydro-Ontario and the Natural Science and Engineering Research Council of Canada (NSERC) for their financial support of this project. I want to thank NSERC for the Scholarship.

My special thanks go to my families: my wife Qing Zhu for her love through all these years, for her being there; my daughter Henan Cao for bringing sweet music to my life, and for her being understanding; my whole families for being my strong backing.

TABLE OF CONTENTS:

ABSTRACT	i
RÉSUMÉ	iii
ACKNOWLEDGEMENTS	iv
TABLE OF CONTENTS	v
LIST OF FIGURES	xi
LIST OF TABLES	xvi
CHAPTER 1:	INTRODUCTION 1
CHAPTER 2:	LITERATURE REVIEW 6
2.1 Microstructure and texture of metal membranes	7
2.1.1 Membranes prepared by cold rolling	8
2.1.2 Membranes prepared by deposition	9
2.2 Hydrogen permeation methods and analysis	12
2.2.1 Gas phase permeation methods	13
2.2.2 Liquid solution permeation methods	14
2.2.3 Analysis of permeation results	16
2.3 Metal-Hydrogen Systems	19
2.3.1 Palladium-Hydrogen system	19
2.3.2 Nickel-Hydrogen and Copper-Hydrogen system	22
2.4 Effects of microstructures on hydrogen permeation in metal membranes	23
2.4.1 Effect of grain size and grain boundary structure on hydrogen permeation	24

2.4.2	Effect of orientation on hydrogen permeation	28
2.4.3	Effect of defects on hydrogen permeation	29
2.4.4	Hydrogen trapping and diffusion mechanism	30
2.5	Effects of interfaces on hydrogen permeation in multi-layer membranes	34
2.5.1	Effect of metal/oxide interface on hydrogen permeation	35
2.5.2	A role of metal/metal interface in hydrogen permeation	35
2.5.3	Hydrogen diffusion mechanism in multi-layer membranes	37
2.6	Summary	39
CHAPTER 3	RESEARCH METHOD AND MATERIALS		40
3.1	The scenario of the study	40
3.2	Description of research materials	43
3.2.1	Cold Rolling process for Pd and Pd ₇₇ Ag ₂₃ alloy membranes	43
3.2.2	Electrodeposition process for nickel membranes	44
3.3	Experimental techniques	45
3.3.1	Hydrogen permeation techniques	45
3.3.2	Measurements of microstructure and texture	49
CHAPTER 4	EFFECTS OF DEFORMATION ON HYDROGEN PERMEATION IN PD AND PD-AG MEMBRANES		53
4.1	Introduction	53

4.2 Microstructure and texture of Pd and Pd-Ag membranes	54
.....	54
4.2.1 Microstructure in Pd and Pd-Ag membranes	54
4.2.2 Deformation Texture of Palladium and Palladium-Silver Alloys	56
4.2.3 Annealing Texture of Palladium and Palladium-Silver Alloys	60
4.2.4 Summary	62
4.3 Optimization of hydrogen permeation in palladium membranes	63
4.3.1 Hydrogen permeation measurements	63
4.3.2 Optimization of Hydrogen permeation	64
4.4 Effect of deformation of Pd and Pd₇₇Ag₂₃ alloy on hydrogen permeation	65
4.4.1 Effects of cold rolling on hydrogen permeation	65
4.4.2 Hydrogen trapping analysis for metals with defects	69
4.4.3 Summary	70
4.5 Simulation of hydrogen trapping in metal membranes	71
4.5.1 Trap mechanism analysis and trapping map	71
4.5.2 The model description of hydrogen trapping	74
4.5.3 Simulation details and process of hydrogen permeation	75
4.5.4 Comparison of hydrogen trapping behaviors with the model	80
4.5.5 Summary	82

CHAPTER 5	EFFECTS OF GRAIN SIZE ON HYDROGEN PERMEATION IN NI MEMBRANES	84
5.1 Introduction	84
5.2 Microstructure and orientation in nickel membranes	85
5.2.1 Effect of annealing temperatures on grain sizes of nickel membranes	85
5.2.2 Effect of annealing temperatures on grain orientation in nickel membranes	86
5.3 Effects of grain size on hydrogen permeation in membranes	91
5.3.1 Effects of charging current on hydrogen permeation in membranes	91
5.3.2 Effects of grain size on hydrogen permeation in membranes	94
5.3.3 Effects of grain boundary on hydrogen permeation in membranes	95
5.4 Summary	97
CHAPTER 6:	EFFECTS OF TEXTURE ON HYDROGEN PERMEATION IN NI MEMBRANES	99
6.1 Introduction	99
6.2 Microstructure and texture of nickel membranes	100
6.2.1 Microstructure and texture of nickel deposits	100
6.2.2 Analysis of texture formation in nickel deposits	105
6.3 Effects of texture on hydrogen permeation in membranes	107
6.3.1 Textures of nickel deposits and annealing membranes	107

6.3.2 Hydrogen permeation through differently textured membranes	109
6.4 Summary	112
CHAPTER 7:	ANALYSIS OF MICROSTRUCTURAL FACTORS ON HYDROGEN PERMEATION IN NICKEL, PALLADIUM AND Pd₇₇Ag₂₃ MEMBRANES	114
7.1 Introduction	114
7.2 Grain misorientations in Pd and Pd-Ag membranes	115
7.3 Effects of misorientation on hydrogen permeation in membranes	117
7.4 Microstructure control factors of hydrogen diffusion through Nickel, Palladium and Pd ₇₇ Ag ₂₃ Membranes	122
7.5 Summary	124
CHAPTER 8:	HYDROGEN PERMEATION IN MULTI-LAYER MEMBRANES	126
8.1 Introduction	126
8.2 Hydrogen permeation in nano-nickel and poly-nickel membranes	127
8.2.1 Hydrogen charging for nano-nickel and poly-nickel membranes	127
8.2.2 Hydrogen permeation in nano-nickel and poly-nickel bilayer membranes	128
8.3 Simulation hydrogen permeation in multi-layer membranes	132
8.3.1 Multilayer diffusion mechanism and concentration profile	132

8.3.2 Description of the simulation model	136
8.3.3 Simulation process of hydrogen permeation in bilayer membranes	138
8.3.4 Simulation steps of hydrogen permeation in bilayer membranes	140
8.4 Comparison of hydrogen permeation behaviors in two directions	143
8.5 Summary	145
CHAPTER 9: CONCLUSIONS AND FURTHER RESEARCH		147
9.1 Summary and conclusions	147
9.2 Contribution to original knowledge	154
9.3 Suggestions for future work	156
REFERENCE	158

LIST OF FIGURES:

Figure 2.1	Classification of various membrane preparing techniques	7
Figure 2.2	The schematic microstructure of a cold rolled metal after a larger deformation	9
Figure 2.3	Schematic representation of cross-section microstructure of the electrodeposit	11
Figure 2.4	Schematic diagram of the gas permeation facility	13
Figure 2.5	Schematic of electrochemical permeation cell	15
Figure 2.6	Typical transient record of current vs time	16
Figure 2.7	Phase diagram of Pd-H with bulk palladium	20
Figure 2.8	Diffusion coefficient in a Nano-Pd and single crystal Pd as a function H concentration	24
Figure 2.9	The three types of grain boundary diffusion coefficient in a polycrystal with a stationary grain boundary	27
Figure 3.1	The flowchart of the research scenario	41
Figure 3.2	The flow chart of the study procedure	42
Figure 3.3	Schematic illustration of the electrochemical permeation equipment	46
Figure 3.4	Schematic representation of a typical time-lag curve	49
Figure 4.1	OIM microstructure of palladium	54
Figure 4.2	TEM image of dislocation substructure of deformed Pd	55
Figure 4.3	Pole figures of palladium after 82% cold rolling	56

Figure 4.4(a)	Orientation distribution functions (ODF) of palladium after 40% cold rolling	57
Figure 4.4(b)	Orientation distribution functions (ODF) of palladium after 60% cold rolling	57
Figure 4.4(c)	Orientation distribution functions (ODF) of palladium after 82% cold rolling	58
Figure 4.5	Pole figures of Pd ₇₇ Ag ₂₃ after 80% cold rolling	59
Figure 4.6	Orientation distribution functions (ODF) of Palladium after 82% cold rolling and annealing at 850 ⁰ C, 1.5h	61
Figure 4.7	Orientation distribution functions (ODF) of Pd ₇₇ Ag ₂₃ after 80% cold rolling and annealing at 850 ⁰ C, 1.5h	61
Figure 4.8	Hydrogen permeation in palladium	63
Figure 4.9	Hydrogen permeation efficiency in palladium	64
Figure 4.10	Hydrogen build-up permeation for Pd ₇₇ Ag ₂₃ membranes	66
Figure 4.11	Hydrogen build-up permeation for palladium membranes	66
Figure 4.12	Hydrogen decay for Pd ₇₇ Ag ₂₃ membranes	67
Figure 4.13	Hydrogen decay permeation for palladium membranes	68
Figure 4.14	TEM microstructure of Pd with hydrogen trapped in dislocations	72
Figure 4.15	Energetic schematic of hydrogen diffusion with trapping	73
Figure 4.16	Schematic of hydrogen trapping map in the metal membrane	74
Figure 4.17	Procedure of hydrogen diffusion simulation	79
Figure 4.18	Simulation results of metal membranes with trapping	80

Figure 4.19	Effect of binding energy on hydrogen permeation	81
Figure 4.20	Comparison of simulation with experiment data for Pd hydrogen permeation	82
Figure 5.1	Grain sizes change with annealing temperature	85
Figure 5.2	Texture (ODF) of nano-nickel membranes	86
Figure 5.3	Texture (ODF) of nickel membranes annealed at 400 ⁰ C	87
Figure 5.4	Texture (ODF) of nickel membranes annealed at 700 ⁰ C	88
Figure 5.5	Texture (ODF) of nickel membranes annealed at 900 ⁰ C	89
Figure 5.6	Grain boundary character distributions (GBCD) of nano-nickel membrane and nickel membranes after different annealing temperatures	90
Figure 5.7	Percentage of different classes of grain boundaries in nano-nickel and annealed nickel membranes after different annealing temperatures for 1h	89
Figure 5.8	Permeation transients for nano-nickel membranes with different charging current	91
Figure 5.9	Relationship between diffusivity, efficiency and permeation current for nano-nickel membranes with different charging currents	92
Figure 5.10	Decay transients for nano-nickel membranes with different charging	93
Figure 5.11	Hydrogen diffusivity changes with annealing temperature	94
Figure 5.12	Comparison of hydrogen diffusivities among single, poly and nano-nickel with the same orientation	95
Figure 5.13	Calculation of grain boundary volumes and diffusivities for different grain sizes in nickel membranes	96

Figure 6.1	Cross-section optical microstructure of a nickel deposit	101
Figure 6.2	Orientation imaging microscopy (OIM) microstructure of the cross-section in a nickel membrane	101
Figure 6.3	Orientation distribution function (ODF) of a titanium substrate	102
Figure 6.4	Orientation distribution function (ODF) of a nickel deposit	103
Figure 6.5	The strength of (200) texture of electroplated nickel as a function of with the thickness	104
Figure 6.6	Changes of strength of textures in electroplated nickel membranes with the current density	104
Figure 6.7	The annealing texture of a nickel deposit	108
Figure 6.8	Hydrogen permeation curves for nickel deposits with different textures	109
Figure 6.9	Hydrogen absorption energies represented in the form of inverse pole figure for Ni crystal	111
Figure 7.1	Grain boundary distribution character in Pd	115
Figure 7.2	Grain boundary distribution character in Pd ₇₇ Ag ₂₃	116
Figure 7.3	Hydrogen build-up (a) permeation and (b) decay for Pd ₇₇ Ag ₂₃ membranes	117
Figure 7.4	Hydrogen diffusivity and total hydrogen accumulated in specimens as a function of deformed reductions in Pd	118
Figure 7.5	Hydrogen diffusivity and total hydrogen accumulated in specimens as a function of annealing temperature for Pd ₇₇ Ag ₂₃	119
Figure 8.1	Schematics of layer structures and hydrogen charging modes for a nano-poly-Ni multilayer membrane	127

Figure 8.2	Hydrogen decay for poly-nano-Ni membranes in two directions	128
Figure 8.3	Hydrogen concentration profile for poly-nano-Ni membrane	130
Figure 8.4	Hydrogen concentration profile for PN charging in a poly-Ni and nano-Ni composite membrane	133
Figure 8.5	Hydrogen concentration profile for NP charging in a poly-Ni and nano-Ni composite membrane	134
Figure 8.6	Flow chart of hydrogen permeation simulation	142
Figure 8.7	Hydrogen buildup curves from the simulation approach for different ratios of nano-Ni layer and poly-Ni layer in a poly-nano-Ni membrane with NP charging and PN charging conditions	143
Figure 8.8	Hydrogen decay curves from the simulation approach for different ratios of nano-Ni layer and poly-Ni layer in a poly-nano-Ni membrane with NP charging and PN charging conditions	145

LIST OF TABLES:

Table 2.1	Microstructures of Copper Films Deposited by different Techniques	10
Table 2.2	Diffusion parameters of hydrogen isotopes in palladium	21
Table 2.3	Hydrogen permeability and selectivity of differently deposited Pd membranes	22
Table 2.4	Diffusion parameters of hydrogen in palladium alloys	22
Table 2.5	Diffusion parameters in nickel and copper	23
Table 4.1	Dislocation densities in Pd and Pd ₇₇ Ag ₂₃ alloys	56
Table 4.2	Cold-Rolling Texture of Palladium and Pd-Ag alloys after large deformation	58
Table 4.3	Recrystallization Texture of Palladium and Pd-Ag alloys	62
Table 4.4	Hydrogen diffusion and trapping parameters of palladium and Pd ₇₇ Ag ₂₃ alloys	70
Table 6.1	Surface energies of nickel metals	107
Table 6.2	Hydrogen permeation data in nickel membrane with different textures	110
Table 7.1	Summary of microstructure factors for hydrogen permeation	123
Table 8.1	Hydrogen permeation data in single layer and multilayer membranes	132

CHAPTER 1

INTRODUCTION

Metal-Hydrogen systems are playing a crucial role in solving the world's environmental and energy problems. Research on these systems may help to develop novel energy production and applied technology. The use of hydrogen as an energy source is becoming increasingly attractive because fossil fuel reserves are steadily being depleted (Alefeld and Volkl 1978, Armor 1992, Bellanger 1997). Large-scale application of hydrogen energy and technology is widely expected to come to life in the future. This has created, in the last decade, a permanent interest in developing economically viable methods for hydrogen separation, purification and storage (Govind 1991, Armor 1995, Bellanger 1997). Meanwhile, the high concentration of hydrogen in metals affects their mechanical, electrical and optical properties (Barbieri et al 1997, Wipf 1997). The studies of hydrogen in metals are of significant importance in basic and applied research for modern technology.

Since Graham first discovered that palladium could absorb large amounts of hydrogen gas a century ago (Alefeld and Volkl 1978, Wipf 1997), the Pd-H system has been most extensively investigated. In fact, the ability to absorb hydrogen is common to all metals because the hydrogen atom is the lightest and smallest of the solute elements and therefore diffuses easily. Pd, Ti and V metals have high concentrations of hydrogen at low temperatures because of a large positive heat of solution, which favors such high hydrogen concentrations. Ni, Fe and Cu metals have low hydrogen concentrations at low temperatures because of a negative heat of solution. As a matter of fact, the actual hydrogen concentrations in a metal differ from the equilibrium values since the absorption and desorption processes of a hydrogen molecule are usually seriously impeded at the metal surface.

Hydrogen related degradation of structural materials is a serious problem that has received much attention in the past fifty years because much of the corrosion related failures are due to hydrogen damage. Most of the research was focused on solving urgent technical problems. A number of details in the mechanism of hydrogen diffusion, absorption or desorption in materials have not been fully understood. In the meantime, microstructural parameters and their influences on hydrogen transport have received considerably less attention. Since hydrogen absorption and diffusivity are dependent on the structures of materials, one can expect that it is possible to optimize hydrogen transport via control of microstructural characteristics. Control of crystallographic texture and multilayer structures may contribute to the optimization of hydrogen transport.

Although metal-hydrogen research and technical literature on the subject is extensive, some phenomena are still not fully understood. Most of the research has

primarily focused on varying chemical composition and environmental characteristics. At the same time, effects of microstructural factors on the hydrogen transport have not systematically been investigated. The influence of hydrogen trapping on fundamental properties such as hydrogen diffusivity and solubility has been often discussed, but mostly in bcc iron alloys. In fcc alloys, where the solubility of hydrogen is higher and the diffusivity much lower than in bcc alloys, the role of the trapping phenomena is more difficult to demonstrate and to characterize. The knowledge of the hydrogen microstructure interaction is a necessary step for the comprehension of nearly all the elementary phenomena possibly involved in hydrogen embrittlement and hydrogen permeation. All of these phenomena would require optimization of the microstructure so that it is easily penetrated by hydrogen.

The proposed research will focus on the microstructural optimization of hydrogen absorption and transport. The objective of this research is to determine the role of microstructural factors, such as grain orientation (crystallographic texture), grain size and grain boundaries in the absorption and permeation of hydrogen in metallic materials. In this project, various microstructures of palladium, nickel, and Pd-Ag alloy are controlled by different processes. Hydrogen diffusion will be simulated in order to get predictive models for controlling hydrogen permeation. Microstructural manipulation to reduce specific types of traps has led to improved hydrogen diffusivity. The ultimate goal of the project is to propose methods to improve and optimize transport of hydrogen in palladium and nickel films. The methods mentioned above will be used to control the rate of hydrogen diffusion in different directions.

Chapter 1: Introduction

This thesis is organized into the following chapters:

Chapter 2 presents a review on the microstructure and its effect on hydrogen permeation. This chapter starts with microstructure and texture of metal membranes and follows hydrogen permeation methods and analysis. Then, palladium, nickel and copper hydrogen systems are presented. In the latter part of chapter 2, effects of microstructures on hydrogen permeation in single layer metal membranes as well as effects of interfaces on hydrogen permeation in multilayer membranes are reviewed.

In chapter 3, the scenario of the study is explained. The cold rolling process for Pd and Pd₇₇Ag₂₃ alloy membranes and the electrodeposition process for nickel membranes are presented. Experimental techniques used to run hydrogen permeation and measure microstructure and texture of metals are also presented in this chapter.

Microstructural effects are presented in chapter 4. Microstructure and texture of Pd and Pd-Ag membranes are analyzed in deformed and annealed states. Then, effects of deformation on hydrogen permeation are characterized. The trapping of hydrogen in metals with defects is featured. In the last part of chapter 4, the trapping of hydrogen in metal membranes is simulated by a trapping model and is calculated by the computer procedure.

In chapter 5, the effects of annealing temperatures on grain sizes and grain orientations of nickel membranes are investigated. Then, effects of grain sizes on hydrogen permeation in membranes are presented.

In chapter 6, microstructure and texture of nickel membranes are analyzed. Using the weighted average method, absorption energies for different orientations are shown in

Chapter 1: Introduction

the form of an inverse pole figure. Effects of texture on hydrogen permeation in membranes are also characterized.

In chapter 7, the effects of misorientation on hydrogen permeation in membranes are presented. Then, microstructure control factors of hydrogen diffusion through nickel, palladium and Pd₇₇Ag₂₃ membranes are summarized.

In chapter 8, the nano-nickel and poly-nickel membranes with anisotropic hydrogen permeation characters are developed. Based on the analysis of the concentration profiles in nano-nickel and poly-nickel membranes, a model for simulation hydrogen permeation in a bilayer membrane is proposed.

Chapter 9 presents the conclusions and recommendations for future research.

CHAPTER 2

LITERATURE REVIEW

Hydrogen in metals has been a subject of research for more than a hundred years. There has been a steady improvement in our understanding of the ways in which hydrogen interacts with metallic microstructure in a large number of metals and alloys. The interactions of hydrogen with vacancies, voids, grain boundaries, dislocations and impurity atoms have profound consequences on the mechanical behavior and chemical properties of materials. Understanding the permeation of hydrogen through thin metallic membranes is essential for the development of hydrogen selective materials or protecting coatings. This chapter provides a review on the literature of hydrogen permeation in metal membranes. Since hydrogen absorption and diffusion are influenced by the microstructure of metallic membranes, it is important to understand and describe the microstructural characteristics of these membranes. Normally, metal membranes are made in two ways: metallurgical process or deposition. In this chapter, the microstructure

and texture of metallic films will briefly be introduced, followed by a discussion of hydrogen permeation methods and hydrogen-metal systems. Finally, the effects of microstructure on hydrogen permeation in metal membranes will be presented.

2.1 Microstructure and texture of metal membranes

Metal membranes can be prepared by a variety of methods (Biswas 1986, Dini 1997, Neumann 2000, Tosti 2000). In general, different methods can be classified into two categories: normal metallurgical process methods and deposition methods as shown in Fig. 2.1. Conventional cold rolling is a traditional and cheap method to get metallic

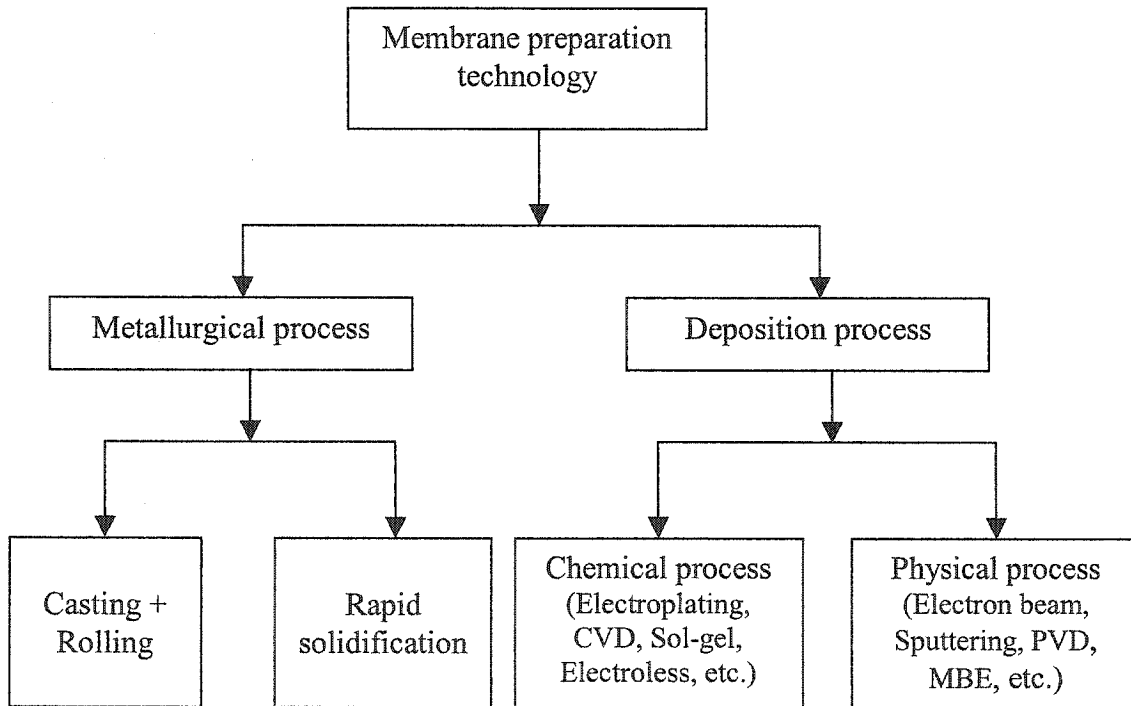


Fig. 2.1 Classification of various membrane preparing techniques

membranes, and is used in the mass-production of thin metal membranes on a large scale. Rapid solidification method that cools melts at very high speed (10^5 - 10^9 K/s) can get amorphous membranes, which have good mechanical properties and superior catalytic

activities (Molnar et al.1989). The deposition method can produce thin films with a thickness on the nanometer scales. The deposition of metal membranes is carried out mainly by using physical deposition and chemical deposition. The methods based on physical processes include physical vapor deposition (PVD) and sputtering. The chemical deposition methods include chemical vapor deposition (CVD), electroplating and electroless plating. The following discussion will focus mainly on palladium-based and nickel-based membranes.

2.1.1 Membranes prepared by cold rolling

Cold rolling of metals produces dislocations. A fully annealed metal can have dislocation densities on the order of 10^6 - 10^8 cm^{-2} . As the degree of cold rolling increases, the dislocation density increases. Heavily cold worked metals can have dislocation densities of approximately 10^{11} - 10^{12} cm^{-2} (Reed-Hill 1973, Hull 1975). During metal deformation, the microstructure changes in several ways. With increasing deformation, the dislocations form a dense cell structure. The grains change their shape and there is a large increase in the total grain boundary area. The location of the original grain boundaries remains clearly visible at small to medium strain. However, distinguishing their location within the overall structure becomes more difficult with increasing strain. Original grain boundaries become a misnomer when considering the large number of dislocations that have been absorbed by the boundaries and the large crystal rotations that have taken place. The new grain boundary area has to be created during deformation and this is done by the incorporation of some of the dislocations that are being continuously created during the deformation process.

The rate of increase of grain boundary area depends on the mode of deformation. At large strain, these boundaries are nearly parallel to the extension direction (Fig. 2.2), e.g. the rolling plane. The average deformed grain contains sets of nearly parallel-extended planar boundaries. A few of these may span nearly the whole grain (Hughes

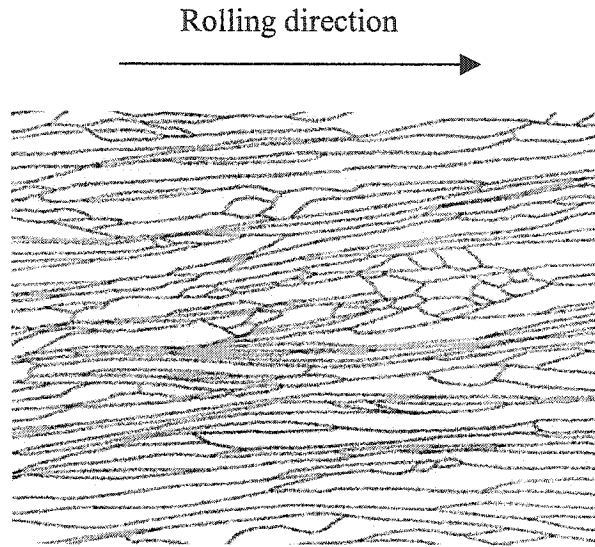


Fig. 2.2 The schematic microstructure of a cold rolled metal after a larger deformation. (Hughes 2001)

2001). The grains of a rolled membrane become laths (Fig. 2.2). The average shape factor of grains (width/length) can be used to describe the shape of grains. Average shape factors of annealed samples were around 1. The average shape factor was 0.21 after a 60% reduction in rolling deformation (Martinez-Madrid et al 1985).

2.1.2 Membranes prepared by deposition

The microstructures of deposits are dependent on the deposition method, substrates, deposition conditions and environment. Microstructural differences in copper

Chapter 2: Literature Review

deposited by four techniques have been summarized in Table 2.1(Walsh et al 1992). The major differences are in grain size and texture.

Grain size in the evaporate membranes is larger than the sputtered (PVD). The reason is that PVD methods employ lower deposition temperatures and higher deposition rates, which impose kinetic limitations on grain growth, yielding finer grain size. The temperature of vapor deposition is greater than 100 °C and that of electrodeposition is less than 100 °C (Dini 1997).

Table 2.1 Microstructures of Copper Films Deposited by different Techniques

Coating method	Thickness (μm)	Average grain size (μm)	Texture
Electroless	8	2.6	(100)
Electroplate	50	0.5	(100)
Evaporate	8	1.8	(111)
Sputtered	8	1	(111)

In electrodeposition, the microstructure of electrodeposits is dependent on plating conditions, substrates and the composition of the electrolyte. By adjusting the pH value, the additive type, the concentration, and the metal ion concentration of the bath, it is possible to obtain a fine grain microstructure or amorphous membranes (Bergenstorf et al 1997, Dini 1997). To control plating condition in practice, various polycrystalline substrates and varying the current density are employed. Using pulse-plating technique can yield nanocrystalline nickel electrodeposits or palladium electrodeposits (El-Sherik 1996, Natter 1996). Metallurgical studies of electrodeposits have proved that the usual

processes of crystal growth occur during electrodeposition. A typical schematic microstructure is presented in figure 2.3 (Fleischmann 1963, Winand et al 1997). The schematic cross-section presented below shows that there are very fine grains near the substrate (region I) and elongated grains are observed toward the electrolytic solution side (region III). The elongated large grains grow as a result of competition between grains. In the middle of the electrodeposit, there is a transition region (region II) with mixed grains of size and shape. If the growth mode is selective, a fiber texture will be obtained (Fleischmann 1963, Bergenstorf et al 1997, Winand et al 1997).

There are two major theories to explain nucleation and crystal growth of metal deposits during deposition processes. The geometrical selection theory regards the rate of

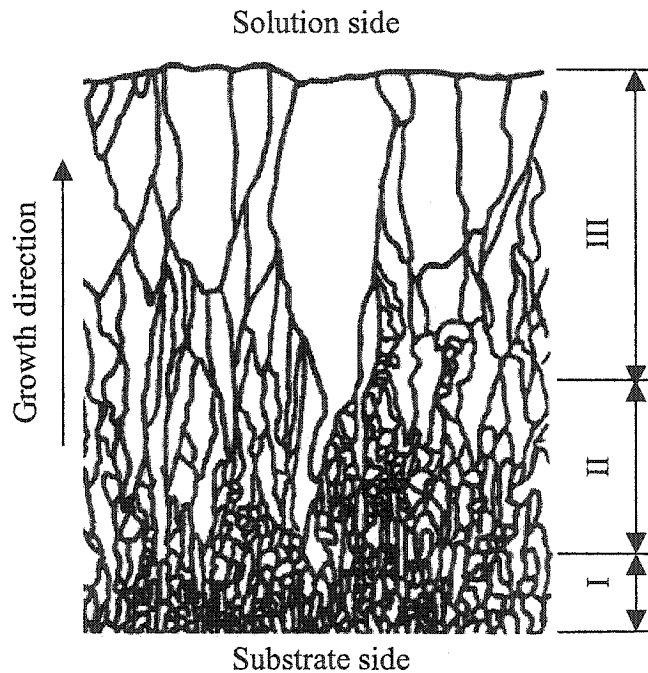


Fig. 2.3 Schematic representation of cross-section microstructure of the electrodeposit (Winand 1997)

growth of the different grain faces as a primary factor in determining the orientation axis. Two-dimensional nucleation theory states that the two-dimensional nucleus, formed on a

low energy plane, decides what texture of the crystallites is developed as a result of the deposition conditions.

Textures of nickel deposits can be (100) or (110) or (112) fiber texture depending on electrolyte, pH value and electroplating parameters (Karayannis 1995, Bergenstorf et al 1997, Czerwinski 1997). Textures of metal membranes can be changed by different deposition techniques or various deposition conditions.

2.2 Hydrogen permeation methods and analysis

There are many sources of hydrogen in metals. Hydrogen can be introduced into metals during cleaning, pickling, cathodic protection, electroplating process and pumping hydrogen gas. Hydrogen presence, hydrogen absorption or transport can be characterized or measured by several methods such as: permeation, electrochemical measurement, resistivity relaxation, quench-recovery methods, mechanical relaxation, magnetic disaccommodation, nuclear magnetic resonance (NMR) and quasi-elastic neutron scattering (QNS). For hydrogen permeation measurements, hydrogen gas and a liquid solution containing hydrogen sources have been widely used (Alefeld and Volkl 1978, Johnson 1988, Fukai 1993, Wipf 1997). They are categorized as gas phase permeation method and liquid solution permeation method. Both methods employ samples in the form of a membrane, which separates either two solutions or two hydrogen gases. Methods involve the introduction of hydrogen into one side of a metal membrane and measuring the rate at which it arrives at the opposite side of the membrane. Those two methods will be briefly described below. All permeation techniques measure the time necessary for hydrogen, introduced on one surface, to enter into the metal, migrate through the thickness of the specimen, and then be detected on the output side.

2.2.1 Gas phase permeation method

Gas phase charging offers attractive advantages for permeation experiments (Kumnick 1975, Flanagan 1976, Lалуze 1988, Hamilton 1996). The apparatus sketch is shown in Fig.2.4. The input hydrogen concentration is known, which can be controlled by the temperature and pressure of the gas. The equipment contains two stainless steel reactor chambers separated by a thin foil. Chamber I is directly connected to an inlet system necessary for introduction of the gas and Chamber II is connected to a mass spectrometer. Chambers I and II are pumped by two turbomolecular pumps to maintain a certain pressure (Lалуze 1988). The mass spectrometers are connected to the computer, which is used to record data and determine both permeability and diffusivity as a function

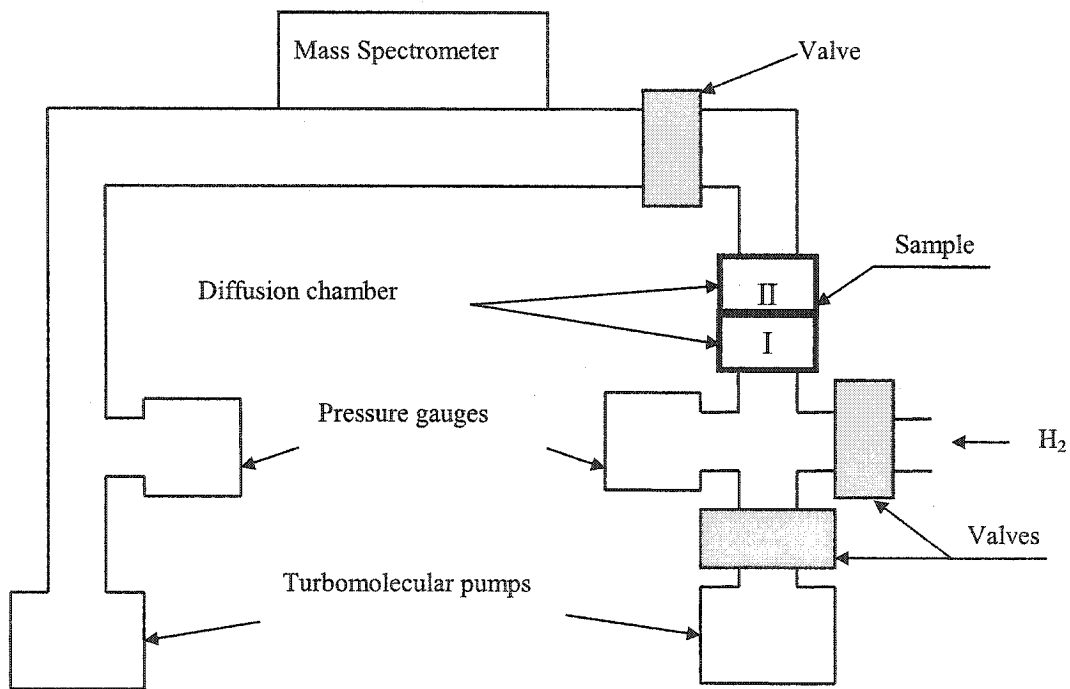


Fig. 2.4 Schematic diagram of the gas permeation facility (Lалуze 1988)

of time.

When hydrogen gas is used, hydrogen permeation through a Pd film takes place in several steps. It includes: hydrogen chemisorption, dissolution into the Pd lattice,

diffusion in the film, which is driven by the concentration gradient, and desorption from the opposite surface (Park 1995). In a pure hydrogen gas environment at moderate pressures, the lattice solubility is proportional to one half the power of the pressure from Sievert's law (Flanagan 1976).

Introduction of hydrogen into a metal from a gaseous phase has the advantage of easy control of relative inlet fluxes and it has been widely used in the study of elevated temperature hydrogen permeation in metals. However, this technique cannot duplicate the high hydrogen flux levels of interest in low temperature stress corrosion and hydrogen embrittlement studies (Kimmnick 1974, Van Leeuwen 1973).

2.2.2 Liquid solution permeation method

Hydrogen entry into metals from aqueous solutions has been studied extensively by hydrogen permeation experiments of thin samples using the Devanathan-Stachurski cell (Devanathan 1962, Boes 1976, Kirchheim 1980, DeLuccia 1981, El-Sherik 1992). The electrochemical cell is shown diagrammatically in figure 2.5. It has two identical units terminating in the standard pipe flanges. Each flange has a Teflon gasket and is connected to the membrane. The assembly was then bolted on with the membrane sample between the gaskets to ensure a tight waterproof seal. Respective units carry either a platinum rod as a counter electrode or a capillary-calomel reference electrode. The membrane sample also functions as a working electrode in the system. Facilities for bubbling nitrogen can also be provided. Each cell is filled with a deaerated electrolyte, normally using 0.1-1N sodium hydroxide (NaOH) solution, thermostatically controlled at the desired temperature for measurements. Hydrogen production is carried out by

cathodic polarization at a constant current density or a constant potential according to equation 2.1.

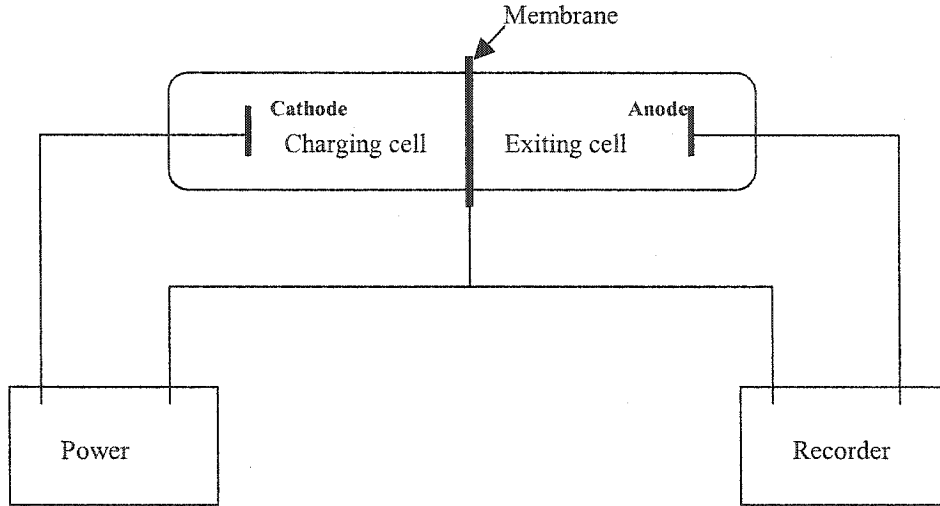


Figure 2.5 Schematic of electrochemical permeation cell



The reaction takes place in alkaline solutions. The hydrogen generated in one compartment will be adsorbed at the surface of the sample, penetrate and diffuse through the sample by solid-state diffusion until it reaches the opposite face of the sample. In the detection (anodic cell) compartment, the output face of the sample is polarized in the passive range in 0.1N NaOH so that the reaction shown in equation 2.2 takes place.



The thickness of a membrane specimen should have a ratio of a specimen thickness to the diameter of charging area, which is larger than 1:10 for a reliable hydrogen permeation measurement (Hutchings 1993).

Electrochemical charging is commonly used to introduce hydrogen into metals. It has the advantage of simplicity for measuring hydrogen through metals, and has a low

cost of the equipment for hydrogen permeation. However, it is difficult to determine the value of the hydrogen concentration. The input hydrogen concentration is determined by many factors, including the nature of the electrolyte, surface condition of the specimen, current, voltage, etc (Johnson 1988).

2.2.3 Analysis of permeation results

The typical curve of hydrogen permeation in metals is shown in Fig. 2.6 (Devanathan 1962, Boes 1976, Alefeld and Volkl 1978, DeLuccia 1981, Johnson 1988). Figure 2.6 is a curve showing the relationship between anodic permeation current i_A and time, t . $i_{A\infty}$ represents the steady-state permeation current. Diffusion is the process by which matter is transported from one part of a system to another as a result of random molecular or atom motions. The diffusion coefficient can be calculated by the time lag method or breakthrough time method. Starting from zero time, the point marked t_b represents the breakthrough time. The breakthrough time is defined as the time between the beginning of the charging cathodic current at the entry side and the onset of the anodic current at the exit side. The time required for the permeation to reach 0.63 times the steady-state value is marked t_L , the time lag (Devanathan 1962, Boes 1976, Johnson

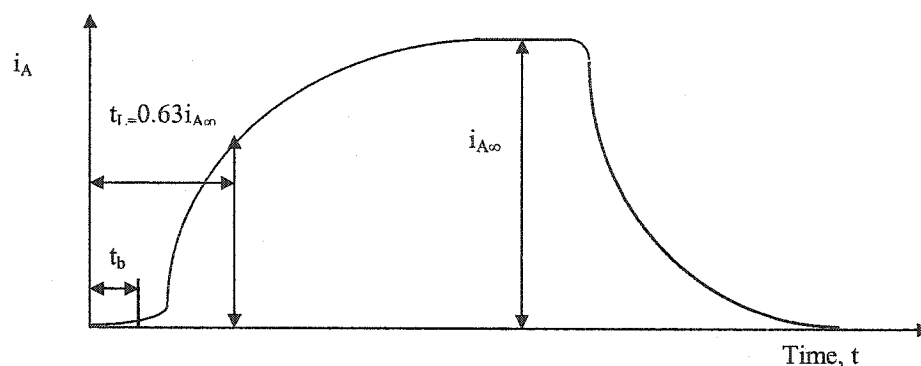


Figure 2.6 Typical transient record of current vs. time

1988). t_L is the intercept on the time axis of the extending straight line of the time integral of permeation current in the integrated flux vs. time figure. The time-dependent equation of hydrogen concentration, $c(x,t)$, in the metal is described by Fick's second Law (equation 2.3).

$$\frac{\partial c}{\partial t} = \frac{\partial}{\partial x} \left(D \frac{\partial c}{\partial x} \right) \quad (2.3)$$

where x is the distance into specimen from the charging surface measured in the thickness direction. t is the time started from commencement of hydrogen charging. For certain techniques it is necessary to know the variation of the anodic current with time, $i(t)_{x=L}$, L is the thickness of the specimen. The hydrogen flux, $J(L, t)$, at the anode surface at time t can be given in terms of the measured anodic current $i(t)$ by equation 2.4.

$$J(L, t) = \frac{i(t)}{Fq} \quad (2.4)$$

where F is the Faraday's constant and q is the number of electrons transferred at the exit side. The anodic current is obtained from Fick's first Law by differentiation of the concentration $c_L(t)$ and yields equation 2.5

$$i(t)_{x=L} = - D q F \left[\frac{\partial c_L(t)}{\partial x} \right] \quad (2.5)$$

In order to evaluate the results obtained electrochemically, solutions to the equation given above must be found, which satisfy the boundary conditions required in the experiment. C_0 is defined as the sub-surface concentration of atomic hydrogen at the charging side of the specimen. C_L is defined as the concentration of hydrogen at exit side of the specimen. Two such methods are illustrated below:

a. Galvanostatic charging is when a constant hydrogen flux is established at the entry surface while a constant hydrogen concentration $C_L = 0$ is maintained at the exit surface. The boundary conditions are:

$$t = 0 ; c \equiv 0 \text{ for } 0 \leq x \leq L$$

$$t > 0: J_0 = D C_\infty / L, C_L = 0$$

Using Fourier transforms and the boundary conditions given above (Alefeld and Volkl 1977, Boes 1976, DeLuccia 1981), the solution which satisfies equation (2.3) and (2.5) is given by equation (2.6).

$$i(t) = i_0 \left\{ 1 - \frac{4}{\pi} \sum_0^{\infty} \frac{(-1)^n}{2n+1} \exp \left[- \frac{(2n+1)^2 \pi^2 D t}{4L^2} \right] \right\} \quad (2.6)$$

The elapsed time measured extrapolating the linear portion of the rising permeation current transient to $i(t)$ at the inflection point yields the break-through time, t_b , which is shown in equation (2.7). Another measure of permeation is based on integrating equation (2.6) over the whole range of time. As a result, the total hydrogen flux can be obtained. An extrapolation of the plot of total quantity for hydrogen flux against time gives the time lag, t_L , in equation (2.8).

$$t_b = 0.76 [L^2 / \pi^2 D] \quad (2.7)$$

$$t_L = L^2 / 2 D \quad (2.8)$$

b. Potentiostatic charging is when a constant hydrogen concentration (C_0) is established at the entry surface while a constant hydrogen concentration $C_L = 0$ is maintained at the exit surface. The boundary conditions are:

$$t = 0 ; c \equiv 0 \text{ for } 0 \leq x \leq L$$

$$t > 0: C_0 = \text{constant}, C_L = 0$$

Using the potentiostatic boundary conditions and Fourier transforms, the solution to equations (2.3) and (2.5) is given by equation (2.9).

$$i(t) = i_0 \left\{ 1 + 2 \sum_1^{\infty} (-1)^n \exp \left[-\frac{n^2 \pi^2 D t}{L^2} \right] \right\} \quad (2.9)$$

The break-through time, t_b (2.10) and the time lag, t_L (2.11) can be obtained in the same way as above. Refer to equation 2.10 in the text

$$t_b = 0.5 [L^2 / \pi^2 D] \quad (2.10)$$

$$t_L = L^2 / 6 D \quad (2.11)$$

The diffusion coefficient can be determined from the equation (2.8) or (2.11) depending on the method used.

2.3. Metal-hydrogen systems

2.3.1 Palladium-Hydrogen system

Palladium is a monomorphic metal with an FCC crystal structure. It is a noble metal in the platinum group. Like other platinum group metals, palladium has high stability, adequate heat resistance, and good deformation characteristics and corrosion resistance in many aggressive media. The recrystallization temperature for palladium at 60-90 percent deformation is about 400-500⁰C (Savitskii 1969). Palladium-silver alloys crystallize to form a continuous series of solid solutions. Pd-Ag alloys are plastic and easily worked by rolling, drawing and pressing. Palladium alloys with around 20-25 at. % Ag have high hardness and strength and very good ability for hydrogen permeation (Metals Handbook 1980, Sakamoto et al 1982).

The palladium-hydrogen system has been extensively investigated (Lewis 1967, Alefeld and Volkl 1978, Fukai 1993). Palladium dissolves large amounts of hydrogen

measured by the atomic ratio $n_H = C_H / C_{Pd}$. The phase diagram of Pd-H is shown in Fig 2.7 (Alefeld and Volkl 1978, Fukai 1993). When palladium absorbs hydrogen below 298°C depending on the concentration of hydrogen, there are two phases, α and β both having an FCC structure. At room temperature, hydrogen is sparingly soluble in the α phase, corresponding to a maximum in Fig. 2.7 of PdH_{0.015}, and the lattice parameter extends slightly from 0.3889 nm for pure Pd to 0.3894 nm for PdH_{0.015}. When the hydrogen content is higher than PdH_{0.6}, the β phase with lattice parameter of 0.4025 nm is formed.

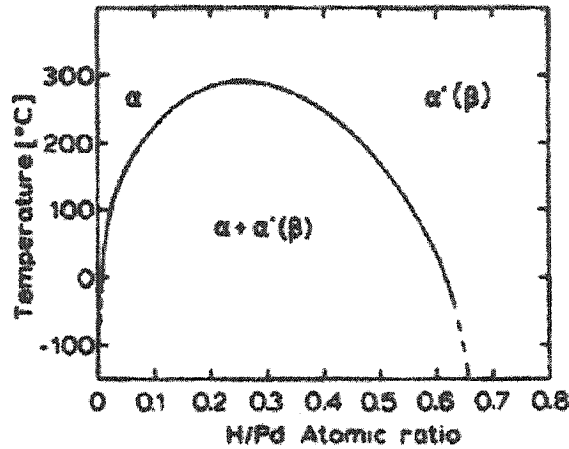


Fig. 2.7 Phase diagram of Pd-H with bulk palladium (Alefeld and Volkl 1978)

Between the α and β single-phase regions, there is an $\alpha + \beta$ mixture phase region separated by a spinodal curve from α and β phase region.

Much of the experimental data (Lewis 1967, Alefeld and Volkl 1978, Fukai 1993, Wipf 1997) concerning hydrogen diffusion and permeation are well represented by straight lines on the Arrhenius plot in a wide temperature range (200-1200K). The diffusion coefficient can be expressed in the form shown in equation 2.12.

$$D = D_0 \exp(-E_a/kT) \quad (2.12)$$

Chapter 2: Literature Review

The diffusion constant D_0 and activation energy E_a are listed in Table 2.2. From this table, it can be seen that the diffusion coefficient varies depending on the temperature. The diffusion coefficient is also dependent on the phase structure of palladium as well as differs for different hydrogen isotopes (H, T, D).

Table 2.2 Diffusion parameters of hydrogen isotopes in palladium

Isotope	Phase (Pd-H)	T K	D_0 $10^{-3}\text{cm}^2\text{s}^{-1}$	E_a kJ/mol	Reference
H	α	230-760	2.9	22.2	Mackor 1981
	α	742-1237	2.83	21.7	Nishikawa 1996
	$\alpha + \beta$	293-335	1.82	22.2	Czerwinski 1997
	β	296-373	7.76	26.9	Hamilton 1996
T	α	290-322	10.5	26.6	Mackor 1981
D	α	218-333	1.7	19.9	Mackor 1981

The permeation characteristics of CVD and electroless-plated Pd membranes are shown in table 2.3 (Kikuchi 2000). The CVD and electroless-plated Pd membranes have similar hydrogen permeation characteristics, but different hydrogen selectivities. This means that different deposition methods affect hydrogen selectivity in palladium membranes.

The diffusion constant D_0 and activation energy E_a for palladium alloys are listed in Table 2.4. In general, the diffusion coefficient of Pd alloys is smaller than that of pure

Pd. The activation energy and diffusion coefficient of Pd with 23-25%Ag are nearly the same as those of pure palladium.

Table 2.3 Hydrogen permeability and selectivity of differently deposited Pd membranes

Membrane	Permeance (mol / m ² s atm)	Selectivity H ₂ /N ₂	CH ₄ conversion (%)	Permeated dry- gas composition (vol. %)
CVD	0.35	13.0	70.8	95.4
Electroless plating	0.35	∞	86.4	100

T=773K, p=1 atm

Table 2.4 Diffusion parameters of hydrogen in palladium alloys

Alloys	T K	D ₀ 10 ⁻³ cm ² s ⁻¹	E _a kJ/mol	Reference
Pd ₇₇ Ag ₂₃	313-473	2.56	21.2	Pietrzak 1997
Pd ₇₅ Ag ₂₅	353-673	2.68	21.4	Nishikawa 1996
Pd ₉₀ Ce ₁₀	625-1250	1.58	19.3	Yoshihara 1988

2.3.2 Nickel-Hydrogen and Copper-Hydrogen systems

Like palladium, diffusion coefficients of hydrogen in copper and nickel metals also follow Arrhenius behaviors in a large temperature range (Robertson 1973, Alefeld and Volkl 1978, Fukai 1993, Wipf 1997). Table 2.5 shows the diffusion parameters of copper and nickel in a wide temperature range. The diffusion coefficients of hydrogen in nickel gathered from different sources are in good agreement. This good agreement may reflect the fact that nickel has somewhat higher hydrogen solubility than copper. The

diffusion coefficients of nickel and copper are not much dependent on the type of hydrogen isotopes (H, T, D).

Table 2.5 Diffusion parameters in nickel and copper

Materials	Isotope	T °C	D ₀ 10 ⁻³ cm ² s ⁻¹	E _a kJ/mol
Ni	H	25-400	4.0	39.3
		380-986	4.5	36.0
		970-1313	5.5	37.3
	D	250-350	4.2	40.2
		410-650	4.8	38.5
		450-1000	5.3	38.9
T	450-1000	4.3	38.1	
Cu	H	250-500	6.8	47.3
	D	430-640	6.2	37.6
		450-800	7.3	36.9
	T	450-800	6.1	36.5

2.4. Effects of microstructures on hydrogen permeation in metal membranes

The permeation of hydrogen through metals is a multi-step process. There are three typical steps of hydrogen permeation: 1) Absorption of hydrogen on the film surface; 2) hydrogen diffusion and mass transportation through metals; 3) hydrogen desorption from the exit side of metallic films. Among those steps, only one or two plays an important role in hydrogen permeation depending on materials and hydrogen sources. In an aqueous environment, hydrogen permeation through metal membranes is controlled

In an aqueous environment, hydrogen permeation through metal membranes is controlled primarily by the electrochemistry of the hydrogen evolution reaction at the solid-liquid interface. The process involves the hydrogen discharge reaction of the electrolyte onto the metal electrode. It is followed by the recombination of the discharged hydrogen atoms into molecular hydrogen or permeation of hydrogen atoms into the solid metal electrode, both of these can occur in parallel.

2.4.1 Effect of grain size and grain boundary structure on hydrogen permeation

When compared to a single nickel crystal, polycrystalline nickel has higher hydrogen solubility. The implication of this result is that fast diffusion takes place at

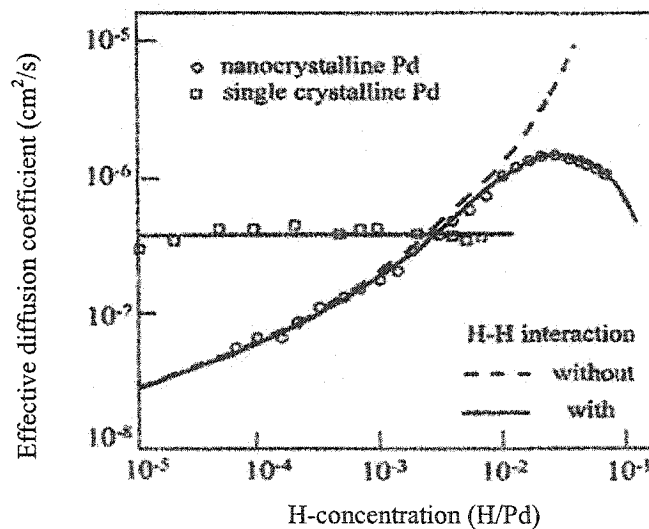


Fig. 2.8 Diffusion coefficient in a Nano-Pd and single crystal Pd as a function hydrogen concentration (Mutschele 1987a)

grain boundaries and the grain boundaries act as sites for absorbing hydrogen, all of which increases the hydrogen solubility (Lee 1985, Stafford 1974). Solid solubility of nanocrystalline materials is higher than in polycrystalline materials. It is worth noting

that the solubility of hydrogen in nanocrystalline palladium increases by 1-2 orders of magnitude because hydrogen segregates at grain boundaries (Mutschele 1987b). The local concentration of hydrogen within the grain is the same as in the single crystal for a given equilibrium pressure of hydrogen (Mutschele 1987a). Nanocrystalline palladium has a larger α phase region than that of polycrystalline palladium (average grain diameter, 20 μm) because the solubility in the grain boundaries is larger. Nanocrystalline palladium has a smaller two-phase region than that of polycrystalline palladium (Kirchheim 1988). For grain sizes of a few micrometers, the effect of grain boundary diffusion on the permeation of hydrogen seems to be negligible when compared to polycrystalline materials (Hirscher 1995, Yao 1991). Since nanomaterials contain a very large fraction of atoms at the grain boundaries and triple junction, the numerous interfaces provide a high density of interfaces. This is expected to enhance diffusivity in comparison to a single crystal or conventional polycrystalline materials (coarse grain) with the same chemical composition (Mutschele 1987a, Harris 1991, Janssen 1997, Bryden 1997). This enhanced diffusivity is responsible for lower temperature of sintering and creep or superplasticity in nanomaterials.

Hydrogen can diffuse quickly through nanostructured palladium and nickel because there are many grain boundaries in the nano-Pd and the nano-Ni, which provide the path for hydrogen diffusion (Harris 1991, Palumbo 1991). Hydrogen diffusion in the grains of the nanocrystalline Pd is similar to its diffusion in the grains of conventional coarse-grained Pd. The hydrogen atoms in the grain boundaries undergo a diffusion process that is locally restricted and has jump rates that are 100 times higher than those of diffusion in the grain (Stuhr 1997). The grain boundary diffusion constant of hydrogen in

nickel is higher than that of lattice diffusion (Arantes 1993). The hydrogen in nano grain nickel diffuses faster than in large grain nickel (Palumbo 1991). For the nano-Ni, hydrogen transports rapidly because there is a relatively large volume of triple junctions and grain boundaries, which contribute to hydrogen diffusion (Marte 1997). The diffusion coefficient of hydrogen in Pd and Ni is related to the hydrogen concentration (Fig.2.8) (Mutschele 1987a, Arantes 1993). The diffusion coefficients of hydrogen are larger for nano-Pd than for single crystalline Pd at large hydrogen concentrations.

Hydrogen diffusion in nanocrystalline Palladium has been investigated by means of quasielastic neutron scattering (QENS) in the temperature range 220-300K within the α phase. The QENS-results reveal broad and narrow line widths, with the first lines being significantly broader than those obtained from the coarse grained PdH reference sample, indicating the presence of a fast diffusion process within the grain boundaries. The narrow line width seems to result from the diffusion within the nanocrystalline grains. A large elastic contribution to the spectra reveals hints on hydrogen traps due to internal surfaces and defects obtained from pulsed electrodeposition and inert gas condensation (Bryden 1997).

Nanostructured palladium films delaminated from the substrates (Bryden 1995, Marte 1997) when exposed to hydrogen at room temperature, owing to the phase transition from α to β . Stabilization against the phase transition and grain coarsening is critical to applications of nanostructured membranes in hydrogen separations, and can be achieved by the alloying of palladium with iron (Janssen 1997, Marte 1997). In nanostructured Pd-Fe alloys, increasing the iron content resulted in grain size refinement.

The Pd-Fe nanoalloys also did not experience the $\alpha \rightarrow \beta$ phase transition when exposed to hydrogen and had fast hydrogen absorption kinetics at room temperature (Janssen 1997).

There are three basic cases for atoms diffusing through metal membranes (Fig. 2.9 from Harrison 1961). Case A corresponds to the condition $(D_G t)^{1/2} \gg d$, where D_G is the diffusion coefficient within the grains, d is the distance between grain boundaries and t is the time. The diffusion length $(2(D_G t)^{1/2})$ within the grains is larger than the grain size. In case B, significant lattice diffusion occurs, but the diffusion length in the lattice is smaller than the grain size. In case C, the diffusion length in the lattice is negligible, and

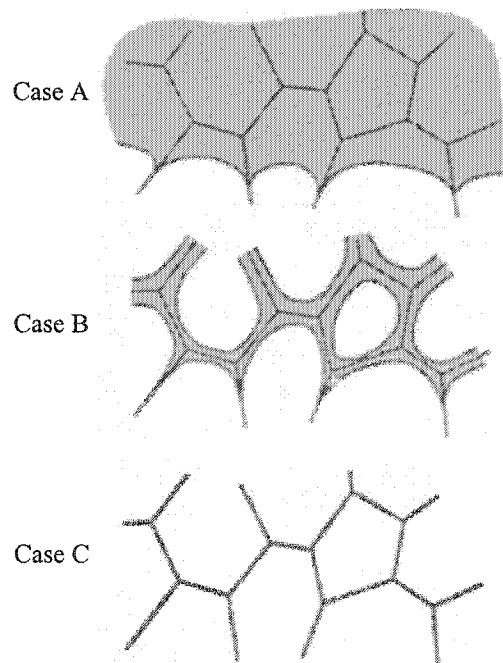


Fig. 2.9 The three types of grain boundary diffusion coefficient in a polycrystal with a stationary grain boundary (Harrison 1961)

diffusion occurs only along the grain boundary network. The overall diffusion (lattice and grain boundary diffusion) in the polycrystals can be described by an effective diffusion coefficient, D_{eff} . The effective diffusion coefficient is given in equation 2.13 (Hart 1957).

$$D_{\text{eff}} = f D_{\text{GB}} + (1-f) D_{\text{G}} \quad (2.13)$$

Where f is the volume fraction of grain boundaries and D_{GB} is the diffusion coefficient along the grain boundaries. For an equiaxed boundary network, $f = 3\delta / d$ where δ is the thickness of grain boundaries. Considering hydrogen segregations, the formula can be modified as shown in equation 2.14.

$$D_{\text{eff}} = s^* f D_{\text{GB}} + (1-f) D_{\text{G}} \quad (2.14)$$

Where s is the segregation factor, which is given in equation 2.15.

$$s = \alpha \exp(E_{\text{GB}} / RT) \quad (2.15)$$

Where the pre-exponential factor (α) is considered to be equal to 1. E_{GB} is the binding energy of hydrogen with grain boundaries.

2.4.2 Effect of orientation on hydrogen permeation

The diffusion of interstitial atoms in single crystal is not random. The experiment by Johnson (1964) indicated that diffusion along some directions is several orders faster than that along other directions. Molecular dynamic embedded-atom method has been used to calculate hydrogen adsorption on nickel and palladium (Daw 1984). Among (100), (110) and (111) planes, the (111) planes of both Ni and Pd have the lowest adsorption energy, which is in agreement with experiment data (Christmann 1974). The theoretical analysis indicates that the diffusion of interstitial atoms in a crystal is related to the structure of the crystal, atomic numbers of the atoms of the host crystal, and the mass of the diffusing atom (Wu 1994). The diffusivity also depends on orientations of grain in polycrystalline nickel (Ebisuzaki 1967, Brass 1996b). A difference is noted for the (001) and (110) single crystal orientations in nickel membranes (Ebisuzaki 1967, Brass 1996a, Brass 1996b).

There is little data for textured polycrystalline materials. As the major texture component in cold rolled iron has a $\langle 110 \rangle$ axis parallel to the direction of deformation, the surface layer consisted of (100) planes facing outward and the close-packed {111} planes inclined at 45° to the surface. It may be possible that this kind of crystallographic arrangement reduces the permeability of hydrogen (Martinez-Madrid et al 1985). Rath et al (1971) found that the crack path in hydrogen-charged iron was related to grain boundary orientation. Boundaries with angular misorientation of up to about 20° never showed any cracking. These results are independent of the boundary type or the common rotation axis. A large proportion of grain boundaries having higher misorientation angles cracked.

2.4.3 Effect of defects on hydrogen permeation

Defects in the host lattice of metals influence both the solubility and diffusivity of hydrogen. These defects may include dislocations, grain boundaries, vacancies and voids. In metals, hydrogen is not homogeneously distributed. Not only is hydrogen found in the host lattice, but is also attached to atomic and microstructural imperfections such as: vacancies, solute atoms, dislocations, grain boundaries, voids and second phase particles. The generic term for this phenomenon is trapping. The fraction of the lattice containing defects acts as a trapping region where the mean residence time of hydrogen atoms is sensibly longer than in the defect-free regions. A trapped atom must acquire energy substantially greater than the lattice migration energy to escape the trap. This creates an overall lower mobility of hydrogen.

The rate-controlling step for permeation in metals can be governed either by bulk diffusion or surface effects, depending on the hydrogen diffusivity in the materials.

Defects, introduced by deformation and heat treatment of materials, can play a role in both cases.

Phase boundaries of coherent precipitates in metals and alloys are known to act as strong traps for hydrogen (Turnbull 1990, Kirchheim 1990). For nickel alloys, the γ' precipitate developed during aging significantly reduces the diffusivity of hydrogen atoms. This phenomenon is attributed to trapping and is associated with the γ' /matrix interface. Significant segregation of hydrogen atoms to the γ' /matrix interface coupled with the high local volume fraction of the precipitates at the grain boundary is thought to provide an explanation for the enhanced cracking observed after the heat treatment. Aluminum oxide precipitates were produced in a palladium matrix by internal oxidation. After charging with hydrogen, irreversible hydrogen trapping was observed in Pd/Al₂O₃. Obviously, hydrogen is trapped by the interphase boundaries, which results in decrease of hydrogen activity and mobility because there is no solubility of hydrogen within Al₂O₃ at room temperature (Huang 1991). Even after an annealing treatment of 24h at 800⁰C in a high vacuum, only a small fraction of trapped hydrogen was removed from Pd/Al₂O₃. The binding of hydrogen atoms to the Pd / Al₂O₃ interface is much stronger than to the grain boundaries. The majority of reversible traps in Pd-Al₂O₃ and in Pd-ZnO materials are the same as in pure Pd. For Pd-MgO and Pd-ZrO₂ materials, the number of reversible traps is greater than in pure Pd (Huang 1991).

2.4.4 Hydrogen trapping and diffusion mechanism

Hydrogen trapping in metals has been extensively studied both experimentally and theoretically. The most prominent results of hydrogen trapping focused on the increase of the hydrogen solubility and the decrease the diffusivity. Trapping sites

include dislocations, grain boundaries, voids, and particle-matrix interfaces (Pressouyre 1978, Hirth 1980, Wert 1983).

When equilibrated in a fixed external chemical potential of hydrogen, a metal will absorb hydrogen to the solubility of the host lattice, and additional hydrogen will occupy the traps. Equilibrium is established when the lattice and trap hydrogen populations are jointly equilibrated to each other at the certain external chemical potential. Thus, the solubility, or total hydrogen concentration, will be significantly greater than the lattice solubility.

Trapping decreases the diffusivity, because the mean residence time of a hydrogen atom in an atomic or microstructural trap is considerably longer than in an interstitial lattice site. A trapped atom must acquire energy that is substantially greater than the lattice migration energy to escape the trap and contribute to measured transport parameters. Consequently, if there is presence of trapping, the diffusivity will be less than the lattice diffusivity.

In the case of hydrogen in nickel, trapping at grain boundaries has been found to be negligible and its contribution is probably less than that of dislocations or vacancies (Baskes et al 1985). Apparent hydrogen trapping at dislocation cores in palladium has been evaluated from the measurements of resistivity (Rodrigues et al 1983). Small angle neutron scattering (SANS) techniques have been used to investigate hydrogen and deuterium trapping in palladium. SANS is particularly sensitive to hydrogen, which is very difficult to locate by other techniques. Also, SANS can distinguish between hydrogen and deuterium, which is useful in determining where the hydrogen is trapped in the metal membranes. For single crystal and polycrystalline palladium materials,

hydrogen atoms are mainly trapped around dislocations (Heuser et al 1998, Ross et al 1999).

McNabb and Foster developed a physical model of hydrogen trapping. A mathematical formation of trapping was derived from Fick's law (McNabb 1963). They used a set of two coupled nonlinear differential equations that describe the time evolution of the mobile and trapped hydrogen in materials with a uniform density of traps. Those traps are saturable, which means each site is capable of trapping only a single hydrogen atom. The diffusion equation in the presence of microstructural or lattice trapping may be written as per equation 2.16.

$$\frac{\partial c_L}{\partial t} + N_T \frac{\partial n}{\partial t} = D_L \nabla^2 c_L \quad (2.16)$$

D_L is the lattice diffusivity

C_L is the lattice concentration

N_T is the trap density, which is the number of trapping sites per unit volume.

n is the fractional occupancy of traps, $0 \leq n \leq 1$. n is defined on equation 2.17.

$$\frac{\partial n}{\partial t} = kc_L (1 - n) - pn \quad (2.17)$$

Where k is the capture parameter, which is the transition probability for hydrogen transport from lattice sites to trap sites, and p is the escape parameter, which is the transition probabilities for hydrogen transport from trap sites to lattice sites. If each trap can accommodate one hydrogen atom, then the saturation of traps is equal to the trap density. With a local equilibrium, the trapped and lattice concentrations are related to the equilibrium constant K shown in equation 2.18 (Oriani 1970).

$$K = N_L \frac{k}{p} = \exp\left(\frac{E_b}{RT}\right) \quad (2.18)$$

E_b is the binding energy. For local equilibrium boundary condition in permeation, the time lag t_T is given in equation 2.19.

$$t_T = \frac{a^2}{6D_L} \left\{ 1 + \frac{3\alpha}{\beta} + \frac{6\alpha}{\beta^2} + \frac{6\alpha}{\beta^3} (1 + \beta) \ln(1 + \beta) \right\} \quad (2.19)$$

$$\alpha = N_T \frac{k}{p} \quad (2.20)$$

$$\beta = c_0 \frac{k}{p} = \frac{n}{1-n} \quad (2.21)$$

where α is the trapping parameter described by equation 2.20. The parameter β is a quantitative measure of trap occupancy and is shown in equation 2.21. Without trapping, N_T approaches zero, therefore α is zero, which is the normal case. When there is trapping, N_T increases and α increases too. The hydrogen permeation will be delayed accordingly.

Various scientists have obtained numerical solutions for different values of the trapping parameters for several geometries. Since the differential equations for the concentrations of hydrogen at interstitial lattice sites and trapped hydrogen contain nonlinear terms, they have to be solved numerically. For given trapping parameters, a computer calculation is used to fit the measured permeation transient to numerical solutions of the full nonlinear trapping equation. Standard computer programs for least squares fitting may be combined with the Caskey-Pillinger solutions to obtain the best fits to the measured transients and the best values for the trapping parameters (Caskey

1975). The capture parameter, the escape parameter, and the trap density can be obtained from the least squares fitting.

To deal with more than one kind of trapping site (in terms of binding energy), Myers et al (1979) numerically solved the modified diffusion equation from McNabb-Foster with two trapping terms. The solution of the numerical method has been used to interpret deuterium diffusion in stainless steel and iron. For multiple kinds of trapping sites, Kasuya's solution shows that the average value of calculated diffusion coefficient equals that of local equilibrium treatment (Kasuya 1999). The form has been extended to include non-saturable trapping and stress effects.

With the presence of local equilibrium, the influence of traps on the effective diffusivity (D_{eff}) can be given by equation 2.22(Young 1998).

$$D_{eff} = \frac{D_L}{1 + \sum \frac{N_T}{N_L} \exp\left(\frac{E_b}{RT}\right)} \quad (2.22)$$

D_L is the true lattice diffusivity, and N_T is the number of trap sites per N_L , the number of lattice sites. E_b is the binding energy defined for a specific trap type. The summation is made over different trap types, such as dislocations and vacancies.

The above discussion presents the most important work on the concept of trapping. The effect of trapping on the diffusivity of hydrogen can be presented by an effective or apparent diffusion coefficient, which is not an intrinsic diffusion coefficient.

2.5 Effects of interfaces on hydrogen permeation in multi-layer membranes

Multilayer metals are composite materials. The thermodynamics and diffusion of hydrogen could play a very important role in determining the mechanical properties in such materials. Interactions between hydrogen and interfaces in multilayer metals are

critical. Until now, there were only a few studies on hydrogen transport in multilayer metal membranes, especially Pd/Ni/Cu-H system. Palladium coatings have improved hydrogen permeation of multilayer metals (Kumnick 1975, Johnson 1988, Yoon 1996, Yu 1991). To avoid oxidation and to enable hydrogen charging, multilayer films are often covered with an additional Pd surface.

2.5.1 Effect of metal/oxide interface on hydrogen permeation

Oxide films deposited onto a Pd foil are an effective way to study hydrogen permeation in brittle oxides because a pure oxide sample is easily broken. The Pd foil in the entrance side not only acts as a support, but also as a hydrogen absorber (Yoon 1997). Palladium metal-oxide-semiconductor (Pd-MOS) devices are used in sensitive hydrogen sensors. The hydrogen adsorbed at the Pd surface of the Pd/SiO interface gives a fast response. The outer and inner surface of the Pd film had similar hydrogen adsorption properties (Eriksson 1998).

Various investigations demonstrated that the metal oxide films have dramatically retarded the hydrogen ingress into the metals (Yen 1999). Hydrogen permeation flux through the bi-layers of the palladium substrate covered with Ni(OH)₂ or TiO₂ film decreases when compared with those through the Pd layer alone (Yoon 1997, Pyun 1996). Sputtered layers of TiO₂ or Al₂O₃ on PH stainless steel can reduce hydrogen embrittlement by preventing hydrogen ingress (Yen 1999).

2.5.2 A role of metal/metal interface in hydrogen permeation

The influence of thin films of Pd, Pt, Ni, Cr, and Cu on the hydrogen permeation through Fe was investigated (Matsushmia 1966, Chatterjee 1978, Takano 1995). The

hydrogen permeation through Ni/Fe and Cu/Fe films was retarded when compared to single layer metals (Takano 1995). The Pt coating on iron retarded hydrogen permeation more than Ni and Cu coatings (Chatterjee 1978). Pd-Au alloy coatings electrodeposited on Pd have similar effects (Pyun 1997). Palladium was plated on the exit surface of the iron to inhibit corrosion and increase the hydrogen sensitivity of the measurement at the exit side (Kumnick 1975, Johnson 1988). Andrew (1991) found that depositing palladium onto the entrance side of an iron membrane enhanced the rate of hydrogen transport across that membrane. The exit surface coated with a thin layer of copper (less than 0.1 μm) had no measurable effect on the diffusion-limited permeation, but reduced the surface-limited permeation rate. Pick et al (1981) have shown that palladium and platinum films on niobium and tantalum increase the rate of hydrogen absorption. The effective hydrogen diffusivity and permeability in Pd-coated Ni-based superalloys are consistently higher than for uncoated alloys (Perng 1988). As the Pd film thickness deposited on the Ta surface increased beyond one monolayer, the chemisorption for the composite film increased (Heitzinger 1993).

To protect steels from hydrogen embrittlement, a thin layer of an effective barrier should be placed on steels to decrease or prevent hydrogen ingress. Nickel was electroplated on steels to lower hydrogen permeability (Song 1990, Luu 1997). Increasing the thickness of coatings cannot significantly enhance the barrier effect, because hydrogen diffusivity in the electrodeposited Ni increased with increase of the thickness of the Ni layer (Song 1990). Electrodepositing Pt on AISI 4135 steel and laser surface melting produced Fe-Pt surface alloy. Hydrogen permeation experiments showed reduced hydrogen absorption compared with the untreated conditions, which means that

laser surface alloying with Pt impedes hydrogen ingress into AISI 4135 steel (Manohar 1995). Electroplated Ni (16 μm) on steel can produce a good hydrogen barrier in terms of permeability. Electroless Ni (6 μm) with 400 $^{\circ}\text{C}$ annealing would have a better hydrogen barrier (Luu 1997).

2.5.3 Hydrogen diffusion mechanism in multi-layer membranes

The steady state hydrogen flux, J_{∞} , through the sample's thickness (L) can be given according to Fick's first law:

$$J_{\infty} = \frac{D_{eff} \Delta C}{L} \quad (2.23)$$

where D_{eff} is the effective hydrogen diffusion coefficient for the composite materials.

ΔC is the gradient of hydrogen concentration through the sample and can be taken as a sum of concentrations in different layers $\Delta C_1, \Delta C_2, \dots, \Delta C_n$.

$$\Delta C = \Delta C_1 + \Delta C_2 + \dots + \Delta C_n \quad (2.24)$$

At steady state, the fluxes through each layer are equal, yielding equation 2.25.

$$\frac{L}{D_{eff}} = \frac{L_1}{D_1} + \frac{L_2}{D_2} + \dots + \frac{L_n}{D_n} \quad (2.25)$$

Where $D_1, D_2, \dots, D_n; L_1, L_2, \dots, L_n$ are the respective diffusion coefficients and the thicknesses of different layers.

If a composite material with thickness (L) has a single coating layer (L_c) and a substrate, equation (2.25) can be rewritten for the composite material by taking $\beta = L_c / L$, as (Miranda 1993).

$$D_{eff} = 1 / \left(\frac{1 - \beta}{D_{sub}} + \frac{\beta}{D_{coat}} \right) \quad (2.26)$$

where D_{sub} and D_{coat} are the respective diffusion coefficients for the substrate and the coating. If the diffusivity in coated materials is lower than that of the substrate, the composite materials will have low diffusivity after coating. This means that the coating blocks the ingress of hydrogen into the coated materials.

For a composite with a thick substrate of thickness L_{sub} and $2N$ alternating layers of two metals of a thickness a , the time lag t_L required to reach steady state conditions is $Na \gg 1$. The solutions for various boundary conditions were proposed by Schmitz (1998) and are shown in the equation 2.27.

$$t_L = \frac{L_{sub}^2}{2D_{sub}} + \frac{1}{6} \frac{N^2 a^2}{kD_1} + \frac{N^2 a^2}{6D_1} + \frac{N^2 a^2}{6D_2} \quad (2.27)$$

where k is the ratio of hydrogen solubilities in both metals 1 and 2. D is the corresponding diffusion coefficient. For nanostructured multilayers usually $Na \ll L_{sub}$ applies and the last equation can be simplified into the following form.

$$t_L = \frac{L_{sub}^2}{2D_{sub}} + \frac{1}{6} \frac{N^2 a^2}{kD_1} \quad (2.28)$$

In the absence of an electric field, the time lag, t_L for the bilayer membrane under a galvanostatic hydrogen injection condition is given by Laplace transform in equation 2.29 (Song 1990).

$$t_L = \frac{L_1^2}{2D_1} + \frac{L_2^2}{2D_2} + \frac{KL_1L_2}{D_2} \quad (2.29)$$

where L_1 and D_1 respectively are the thickness and diffusivity of hydrogen for the first layer(Pd) and L_2 and D_2 represent the thickness and diffusivity of hydrogen for the second layer(oxide). K refers to the ratio of the hydrogen concentration of the Pd side to that of the oxide side just near the interface between them.

2.6 Summary

Methods used to prepare metal membranes can be classified into two categories: normal metallurgical process and deposition. Heavy cold rolling will produce rolling textures and a high density of dislocations in metals. Deposition also can produce different textures in metals. Hydrogen gas and liquid solution permeation methods are widely used for hydrogen permeation measurements. Gas phase permeation methods have the advantage of an easy control of relative inlet fluxes. Liquid solution permeation methods have the advantage of simplicity, low cost of the equipment involved, and the possibility for measuring hydrogen transport through metals. Palladium is a model metal for hydrogen permeation. Palladium alloys with around 20-25 at. % Ag have both high formability and good hydrogen permeation abilities. Microstructural factors, which affect hydrogen permeation in single-layer metal membranes, include grain size and grain boundary structure, orientation of grains, and various defects. The trapping is considered a very important factor affecting hydrogen permeation in deformed metals. For multilayer membranes, the interface between two layers plays a crucial role in control of hydrogen permeation.

The review shows that microstructure factors, which affect hydrogen permeation, have been examined in different ways and for different experimental conditions. It is difficult to compare the findings and determine their credibility. Thus, it is necessary to make more systematic investigations about the effect of microstructural factors on hydrogen permeation in metal membranes.

CHAPTER 3

EXPERIMENTAL METHOD AND MATERIALS

3.1 The scenario of the study

The goal of this research is to systematically investigate the effects of microstructural factors on hydrogen permeation. A schematic diagram of the flowchart of the research scenario is illustrated in Fig. 3.1. From the literature and previous work, these microstructural factors can be identified as: crystal defects, grain size, texture, grain boundaries and other interfaces. To examine the role of these factors, various processing methods should be used to prepare specimens having different microstructure.

Cold rolling was used to produce a high density of dislocations in metal samples. Then, the annealing process was applied to reduce number of defects in the deformed samples. The pulse electroplating method was used to obtain nanometer size grains in nickel electrodeposits. By annealing nano-nickel samples at different temperatures,

various grain size samples were obtained. Electrodeposition and annealing processes were modified to obtain different textures in nickel. Bilayer nickel membranes were produced by depositing polycrystalline nickel on nano-nickel substrates.

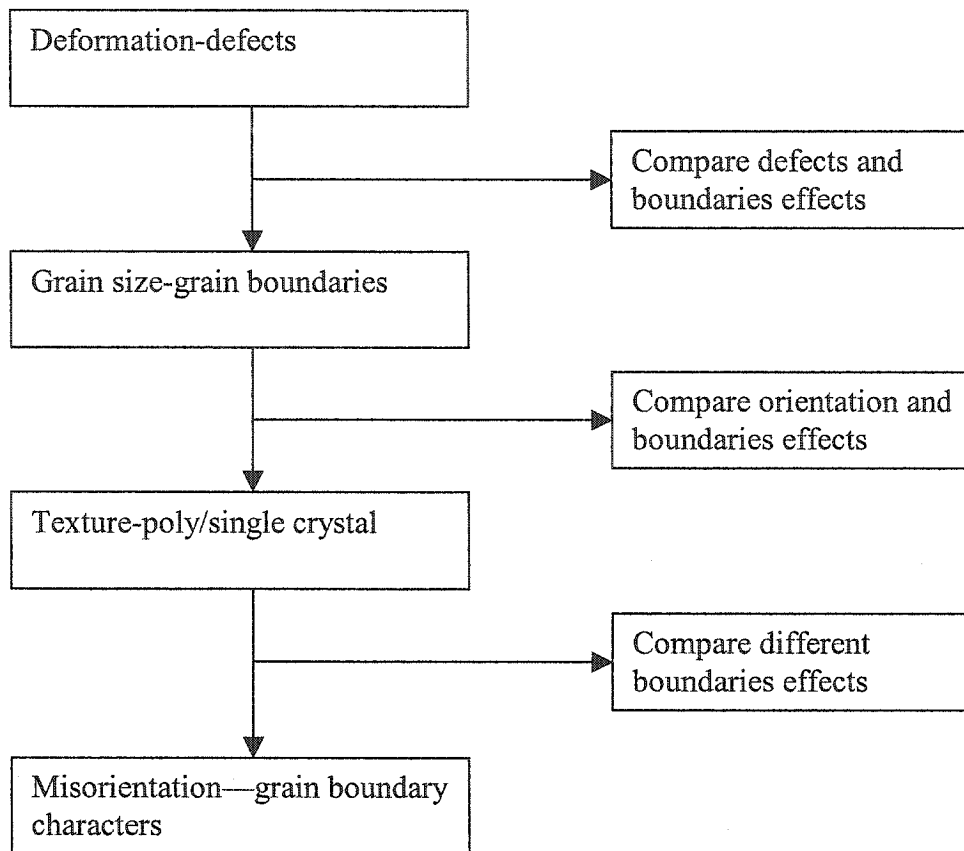


Fig. 3-1 Schematic diagram of the research scenario

The flow chart of the study procedure is shown in Fig. 3.2. The procedure of this study includes four parts: sample preparations to prepare the samples by deposition, cold rolling or annealing; microstructure characterizations to measure texture, grain size and to examine microstructure; hydrogen permeation to measure hydrogen transports. Hydrogen permeation analysis and modeling was done to analyze effects of microstructural factors on hydrogen permeation and to simulate hydrogen permeation in metal membranes.

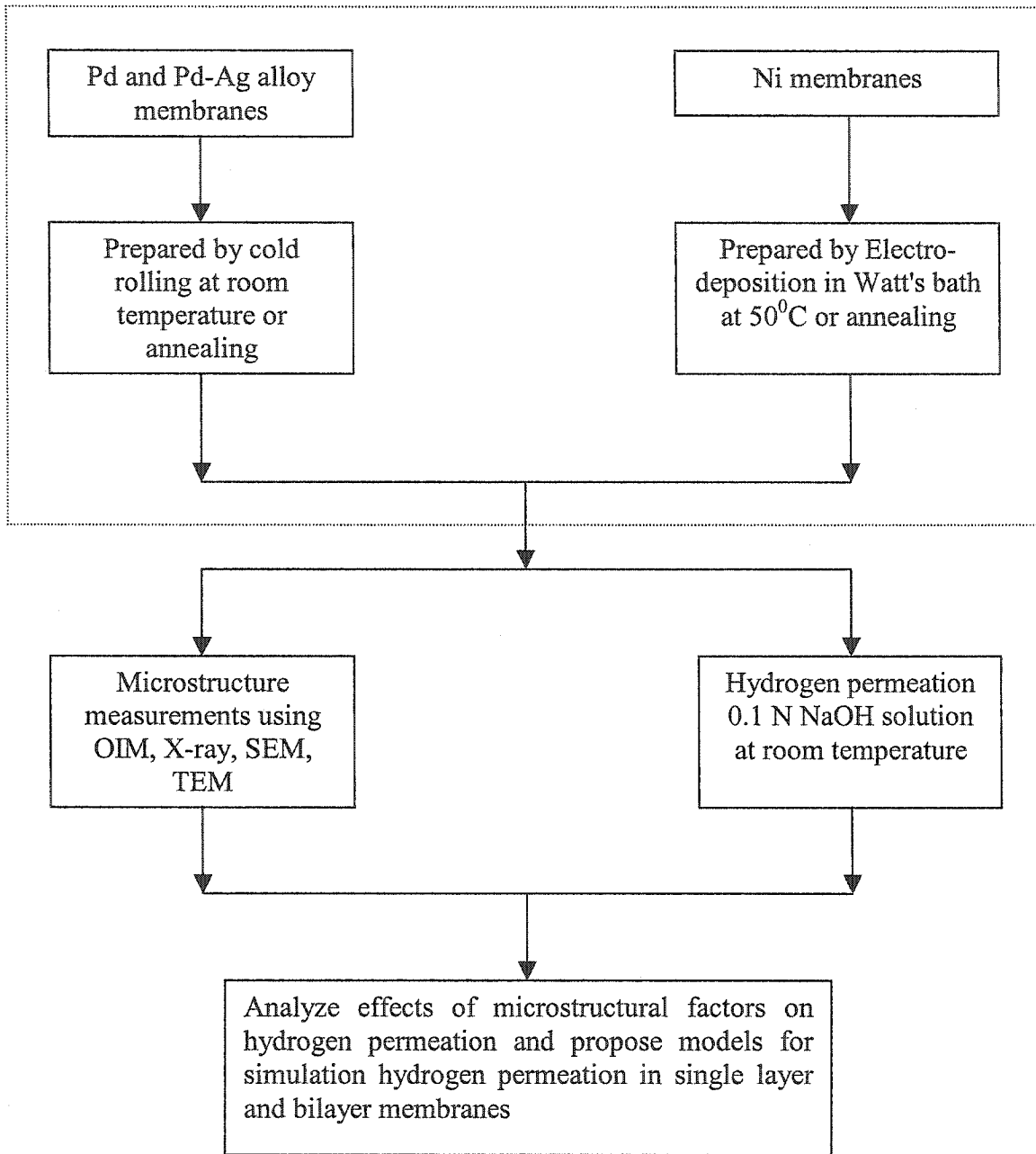


Fig. 3.2 The flow chart of the study procedure

3.2 Description of research materials

Palladium, Pd₇₇Ag₂₃ alloy and nickel were chosen for the investigation. There are several reasons for this selection. Palladium is an important model material for studying hydrogen sorption-desorption and diffusion. Palladium alloys with 20-30 at% Ag not only have high hardness and strength, but also have good hydrogen absorption ability and excellent hydrogen transport properties (Alefeld and Volkl 1978, Wipf 1997). In addition, membranes of palladium and Pd-Ag alloy are also easily formed into tubes, that are used to fabricate hydrogen extraction units, because palladium and Pd-Ag alloys can be formed by rolling and press-forming. Cold rolled sheets of palladium and palladium-silver alloys are widely used in the energy and chemical industries (Govind 1991). A thin membrane can be obtained by cold rolling with intermediate annealing. Cold rolling will produce defects and microstructure changes in palladium and palladium-silver alloys. Annealing will reduce the number of defects in palladium and palladium-silver alloys.

Nickel is the main element in nickel-based alloys and stainless steels with good ductility at cryogenic temperatures, which are often used as containment materials for liquid hydrogen (Nelson 1984). In addition, it is easy to modify textures in nickel by changing deposition parameters (Bergensstof et al 1997). Furthermore, the pulse-plating technique is available to get nanocrystalline nickel electrodeposits (El-Sherik, 1996). Thus, nickel is an ideal material to investigate effect of various microstructures on hydrogen permeation.

3.2.1 Cold rolling process for Pd and Pd₇₇Ag₂₃ alloy membranes

The materials used in the investigation were palladium and Pd₇₇Ag₂₃ alloy. Palladium was purchased from the Johnson Company. The Pd₇₇Ag₂₃ alloy was obtained

from Hydro Ontario. The Pd₇₇Ag₂₃ alloy foils were 80% cold rolled to the thickness of 127 μ m. The palladium membranes were annealed and then subjected to cold rolling in a rolling mill to different strains. The palladium samples were subjected to 20%-82% reductions, with thicknesses of approximately 100 μ m. Palladium membranes were annealed at 850⁰C for 1.5 hours. In addition, Pd₇₇Ag₂₃ alloy membranes were annealed respectively at 250⁰C for 3 hours and at 550⁰C, 700⁰C and 850⁰C for 1.5 hours.

3.2.2 Electrodeposition process for nickel membranes

The nickel electrodeposition membranes were produced from a Watt's bath at 50⁰C. The bath composition was NiSO₄ • 6H₂O 300 g/l, NiCl₂ • 6H₂O 35g/l and H₃CO₃ 35g/l with a pH of 3. The electroplating current was applied galvanostatically in a range of current densities between 10 and 80 A/dm². The anode was pure nickel plate with a purity of 99.5 wt% (Johnson Matthey Inc.). The cathode substrate was chosen as titanium, which can produce nickel membranes that can be easily peeled off. As a final step of the surface finishing preparation on the titanium plate substrate, mechanical polishing and chemical polishing were carried out. The thickness of deposits usually exceeded 50 μ m. It was verified that there was no influence of the substrate orientation on the deposits texture and the texture was an exclusive function of the electrodeposition parameters.

An electrodeposited nanocrystalline sheet of nickel with a thickness of 100 μ m was obtained from Ontario Power Technologies (OPT). From X-ray diffraction measurements, the grain sizes of nanocrystalline nickel were around 35 nm. The chemical analysis has shown that nanocrystalline nickel has 99.8 wt% nickel with major impurities, S-0.12 and C-0.08. The nickel samples with different grain sizes have been obtained by

annealing nano-nickel membranes. The annealing temperatures have been set between 200-900 °C and annealing was carried out at 100°C intervals for 1h.

Bilayer nickel membranes were produced by electrodeposition. The sheet of nanocrystalline nickel with a thickness of 70µm was used as a substrate, which was cleaned by acetone and washed by alcohol and distilled water prior to deposition. The deposition conditions for polycrystalline nickel were the same as above. The Watt's agent was used as the electrolyte at 50°C. The thickness of nickel coatings was around 30µm. The thickness of bilayer membranes was approximately 100µm.

All nickel membranes were sputtered a thin layer palladium for the entry and exit sides, which had a thickness of 50nm. It is important to have a thin layer palladium in the both sides for preventing oxidations at the surface of nickel membranes.

3.3 Experimental techniques

3.3.1 Hydrogen permeation techniques

Electrochemical methods are widely used for hydrogen permeation measurements (Devanathan 1962, Boes 1976, Kirchheim 1980) because of their simplicity and flexibility with regard to experimental conditions. An electrochemical permeation technique requires that a diffusion gradient exists within a metal membrane by producing hydrogen on one side, such as by cathodic charging, and removing it on the other side by anodic polarization with a potentiostat. The electrochemical cell was used for permeation measurements. An adaptation of the Devanathan (1962) two-compartment cell consists of an anode and a cathode cell as well as a control and measurement system (Fig. 3.3). The electrochemical system has two identical compartments that fill with 0.1 N NaOH

(pH=13) as the electrolytic solution. The 0.1N NaOH solution was chosen to meet the need of ensuring stability of the environment at the surface and in the solution over the period of the test. A metal membrane divides two electrochemical compartments clamped

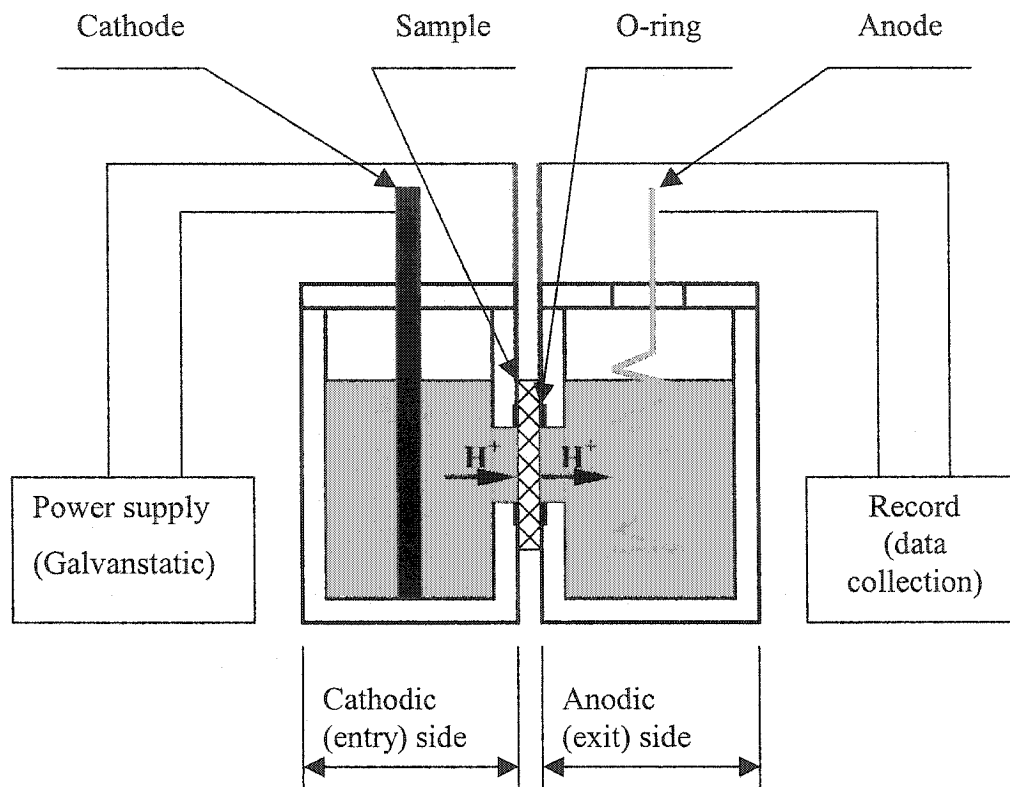


Fig. 3.3 Schematic illustration of the electrochemical permeation equipment

together and serves as a common electrode to both compartments. Nitrogen gas was bubbled into the solution in order to remove oxygen and hydrogen gas from the solutions of both compartments.

In the exit (anode) compartment, a Ni/NiO electrode served as a reference electrode and kept a constant potential of 0.3V vs. saturated calomel electrode (SCE). The potential on the anodic side of the membrane was maintained to oxidize all hydrogen atoms to hydrogen ions (H^+), and to decrease hydrogen concentration of the exit surface

to zero. The 0.3V potential was chosen to ensure that the hydrogen atom oxidation rate was limited for all charging conditions. One advantage is the use of the nickel/nickel oxide electrode to replace the potentiostat device and act as a stable, nonpolarizing power electrode (cathode), which is simple and convenient. Holding an anodic potential of 0.3V at the exit side for 24h will extract the residual hydrogen in the membrane electrode, which allows us to obtain a low background of permeation current density. The diameter of charging area in the cells is 8 mm. Two O-rings are used to seal the gaps between membrane specimen and compartments in order to ensure no leak for the electrolyte during measurements. A graphite rod served as a cathode electrode in the entry (cathode) compartment, which was polarized galvanostatically. A current density of 0.06-0.35 mA/cm² was applied on the cathode side to introduce hydrogen into the membrane. Hydrogen atoms that penetrated through the metal membrane were oxidized into water. The oxidation current recorded at the anodic side of the cell gave the hydrogen flux that permeated through the membrane. The hydrogen permeation current through the membrane was measured and recorded by a computer data collection unit with the DAS-800 Series instrument. The experiment was performed at room temperature.

At the cathodic charging side (entry side) of the membrane, the reactions given in equation 3.1 and 3.2 are expected to take place (Arantes 1993, Brass 1998):



Whereas, at the exit side of the membrane, the reaction shown in equation 3.3 is the expected result in the permeation current because an anodic potential ionizes

hydrogen atoms on the exit surface of the membrane (Brass 1998, Bruzzoni 1992, El-Sherik 1992, Tsubakino 2000):



It is important to choose an appropriate membrane thickness (Iyer and Pickering 1990). If membranes are too thin, the overall permeation process will be surface controlled, which is not representative of the bulk material. Therefore, the thickness of a membrane should be at least five to ten times the average grain diameter. To avoid edge effects causing significant hydrogen leakage laterally, ratios of the specimen thickness to the diameter of charging area should be larger than 1:10 for having a reliable hydrogen permeation measurement (Hutchings 1993). In this research, specimens of metal membranes have 1:40 to 1:200 ratios of the specimen thickness to the diameter of charging area, which are both larger than 1:10. Before the permeation experiment, samples were washed by water and detergent, and then dried. Then samples were cleaned by alcohol and acetone. Finally, after cleaning in distilled water, the samples were washed and dried because effectively cleaned surfaces do not impede the entrance or exit of hydrogen for nickel (Atrens 1980) and palladium as well as palladium-silver alloys (Early 1978, Bucur 1991) membranes.

The diffusion coefficient D is calculated by the time lag method (Devanathan 1962, Boes 1976). An extrapolation of the plot of total quantity for permeation hydrogen current against time gives the time lag, t_L (Fig. 3.4). When galvanostatic charging is considered, the time lag can be expressed as in equation 3.4 (Devanathan 1962, Boes 1976).

$$t_L = L^2/2D. \quad (3.4)$$

where L is the sample thickness. The steady-state flux of hydrogen through the foil is directly proportional to the diffusion coefficient. The concentration of absorbed hydrogen at the input surface, corresponding to a particular cathodic current density, was calculated from Fick's First Law in the permeation steady state. For hydrogen permeation, the relation is given by equation 3.5 (Early 1978, Arantes 1993).

$$C_o = I_{ss} L / FD. \quad (3.5)$$

where C_o is the concentration of absorbed hydrogen at the input surface. L is the thickness of the sample and F is Faraday constant. I_{ss} is the steady state permeation anode current density. With Faraday and Fick's First Law in steady-state permeation (Boes 1976, Early 1978), we can obtain the total amount of hydrogen in the sample (Q_{total}) as shown in equation 3.6.

$$Q_{total} = I_{ss} L^2 / 2FD \quad (3.6)$$

where Q_{total} corresponds to a particular charging current density.

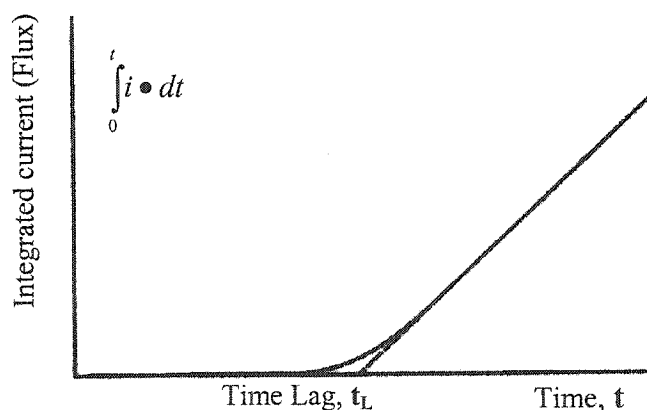


Fig. 3.4 Schematic representation of a typical time-lag curve

3.3.2 Measurements of microstructure and texture

The cross-sections of the nickel electrodeposits were observed with an optical microscope. After mounting in cold setting resin, samples were mechanically polished and etched in a mixture of nitric acid and acetic acid. Philips XL-30 FEG scanning electron microscope (SEM) was used to examine the interface in poly and nano nickel bi-layers. To prepare conductive samples, mounting with carbon powder and hot pressing at 250⁰C was used. Orientation imaging microscopy (OIM) included Philips XL-30 SEM with TSL orientation imaging system, which was used to observe the microstructure of deposition nickel and deformed palladium. Those microstructures are normally difficult to observe using optical and scanning electron microscopes. In order to get a good image from OIM, a vibration polishing equipment was used to polish automatically OIM samples for 10-20h after normal polishing. OIM analysis software of TSL was used to analyze OIM data. The microstructure of the deformed samples was observed using the Philips TM transmission electron microscope (TEM).

The grain size of nanocrystalline nickel was measured by a Rigaku diffractometer with Cu K α radiation. The diffraction broadening method was used to estimate the crystallite size in the nanometer range. Assuming the absence of lattice strains, the extent of the broadening is given by Scherrer's formula in equation 3.7(Cullity and Stock 2000).

$$B = 0.9 \lambda / t \cos\theta \quad (3.7)$$

Where B= FWHM (full width at half maximum) of the broadened diffraction line on the 2 θ scale (radians). λ , t, and θ are the wavelength of x-ray, diameter of the crystallites, and the diffraction angle respectively. In order to separate B from the measured breadth B_M of the diffraction line in the analyzed specimen, Warren's equation was used and is shown in equation 3.8(Cullity and Stock 2000).

$$B^2 = B_M^2 - B_S^2 \quad (3.8)$$

Where B_S is the measured breadth at half-maximum intensity of the standard specimen, which are well annealed or are made by powders.

The dislocation density N_d (line/cm²) in deformed Pd and Pd-Ag alloy membranes was calculated from the domain size (D) and lattice strain (ϵ) values obtained from analysis of broadening of x-ray diffraction lines. An equation used is deduced from the work by Williamson (1965) and Revay (1975) and gives approximate values of dislocation density. It has the following form (equation 3.9).

$$N_d = \frac{\epsilon(3K)^{1/2}}{bD} \quad (3.9)$$

K is a constant depending on strain distribution function (assumed = 12). b is the Burgers vector ($b = \frac{a}{\sqrt{2}}$, a = Pd or Pd-Ag lattice parameter).

The diffractometer method has been used in this experiment. The texture was measured on the outer surface by the Siemens X-ray diffractometer, using a Mo target. Pole figures were obtained using the reflection technique up to a maximum tilt of 80 deg in 5 deg polar and radial intervals. A pole figure is a stereographic projection, with a specified orientation relative to the specimen that shows the variation of pole density with pole orientation for a selected set of crystal planes. If preferred orientation (textures) is present, the poles will tend to cluster together into certain areas of the projection, leaving other areas virtually unoccupied. A pole figure can provide a complete description of preferred orientation. However, different orientations may have the same pole on the pole figure. In order to identify the orientations, one needs more information. Thus, more than one pole figures are measured and the symmetrical poles are analyzed. For crystals with

higher degree of symmetry, such as cubic structure crystals, fewer pole figures are necessary to identify the orientations. For each sample in the experiments, (111), (200), and (220) pole figures were obtained.

The orientation distribution function (ODF) describes the statistical distribution of orientation in a polycrystalline material, which presents textures in three dimensions. The ODF gives the probability of finding a grain with a particular orientation in a microstructure. It is difficult to get orientation information from pole figures since pole figures do not give the orientation distribution directly. The ODF provides a mathematical framework for overcoming this problem. Because it is not easy to measure ODF directly, ODF normally is calculated from pole figure data. The pole figures were then used to calculate the orientation distribution functions (ODF), according to the procedure described by Bunge (1982). Because computer programs are available, the calculation of ODF does not need to be concerned with the mathematics involved. Here, the orientation distribution functions (ODFs) were calculated by TexTools 3.0 software (ResMat Corp) from (111), (200), and (220) pole figures.

CHAPTER 4

EFFECTS OF DEFORMATION ON HYDROGEN PERMEATION IN Pd AND Pd-Ag MEMBRANES

4.1 Introduction

The most popular material for hydrogen storage and separation is palladium and its alloys (Wipf 1997). Palladium is also an important model material for studying hydrogen sorption-desorption and diffusion. Cold rolled sheets of palladium and palladium-silver alloys are widely used in the energy and chemical industries (Armor 1992). The main method to produce a thin membrane is cold rolling with intermediate softening annealing. Cold rolling will produce defects and microstructure changes, which influence the properties of palladium and palladium-silver alloys. Unfortunately, there is little information about deformation texture in palladium and Pd₇₇Ag₂₃ alloys. Furthermore, there are only a few investigations about the relationship between hydrogen permeation and microstructure in palladium and Pd-Ag alloy. In this chapter, the microstructure of cold-rolled Pd and Pd-Ag alloy has been investigated. The

transformation from rolling texture to recrystallization texture is analyzed. Then the effect of microstructure and structure defects on hydrogen permeation in palladium and Pd₇₇-Ag₂₃ alloy is examined.

4.2 Microstructure and texture of Pd and Pd-Ag membranes

4.2.1 Microstructure in Pd and Pd-Ag membranes

The microstructure of palladium after 850⁰C annealing was analyzed using optical microscopy. The grain size of palladium is around 20 μm. The microstructure of

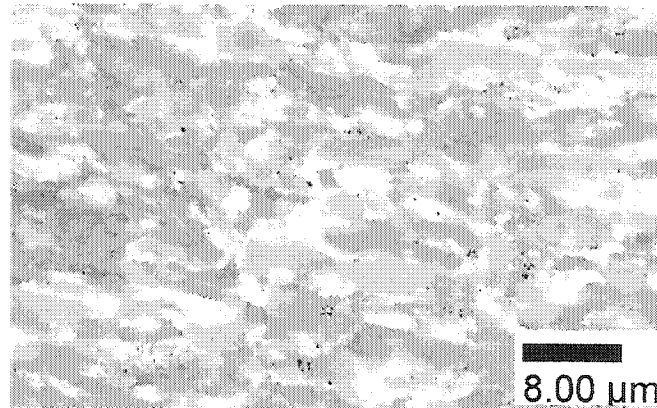


Fig 4.1 OIM microstructure of deformed palladium

deformed palladium is shown in Fig. 4.1. Figure 4.1 was obtained from an orientation imaging microscopy (OIM) image, which presents several colors for distinguishing different grains. Normally, it is quite difficult to etch palladium and its alloys since palladium is a noble metal. From Fig. 4.1, one can see that elongated grains are arranged along the rolling direction. The average grain size of palladium is 15 μm. It is very important to know the grain size of palladium because it will influence hydrogen permeation. A transmission electron microscope (TEM) image of 82% deformed palladium is shown in Fig. 4.2. Heavy cold rolling creates a more heterogeneous or

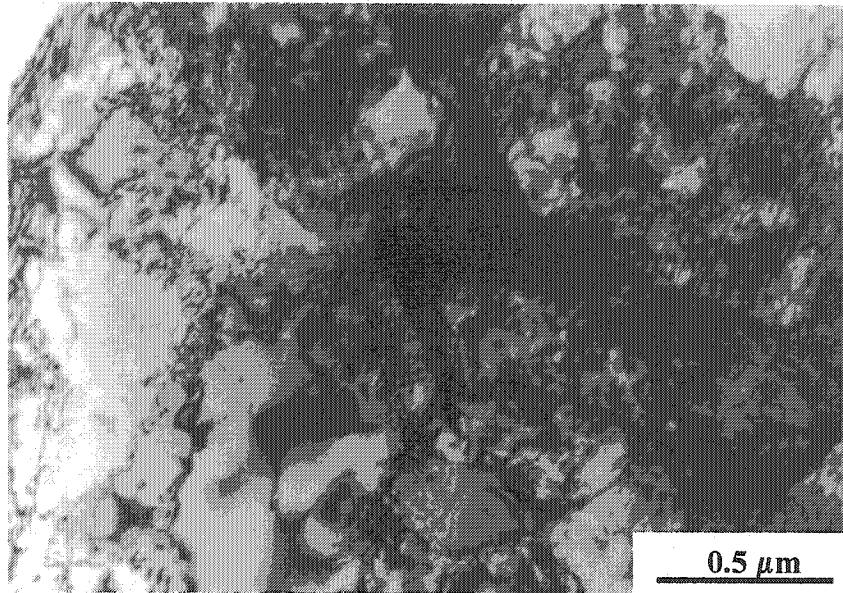


Fig. 4.2 TEM image of dislocation substructure of deformed Pd cellular arrangement of dislocations. High-density dislocations with cellular substructure have been observed. The cellular substructure includes walls with a high dislocation density surrounding regions with a low dislocation density. A cellular dislocation substructure is produced by deformation of metals with the high stacking fault energy at a large strain. Palladium has the high stacking fault energy and the amount deformation (82%) in this Pd sample was very high, so microstructure with dislocation substructure was formed.

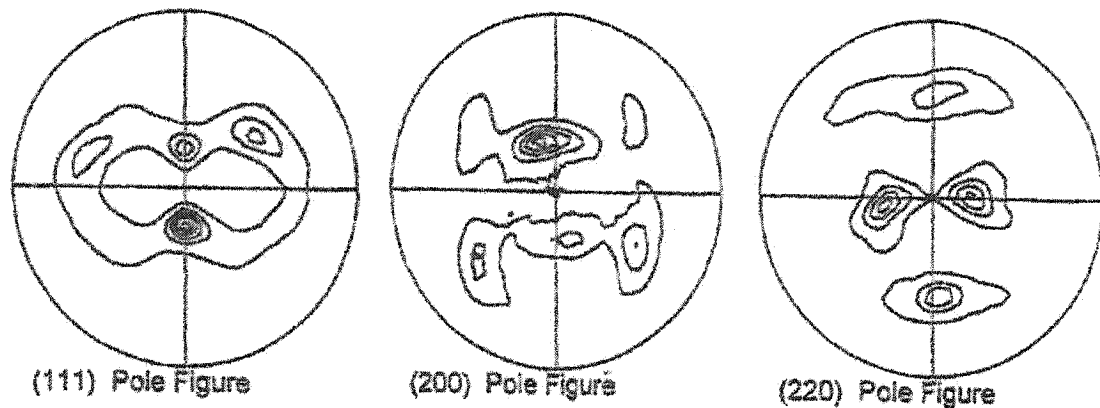
To measure dislocation density in deformed palladium, the diffraction broadening method was used. X-ray diffraction line profiles analysis was used to estimate dislocation densities of Pd and Pd₇₇Ag₂₃ alloy as shown in Table 4.1. From Table 4.1, it can be found that the deformed samples have much higher dislocation density than the annealed ones. Samples with a large amount of deformation have very high dislocation densities. Those dislocations make hydrogen transport and hydrogen discharge from the specimen more difficult.

Table 4.1 Dislocation densities in Pd and Pd₇₇Ag₂₃ alloys

Materials	Dislocation Density, *10 ¹² /cm ²
Pd	
850°C, 1.5h	0.07
20% Deformation	0.38
50% Deformation	1.7
82% Deformation	2.9
Pd ₇₇ Ag ₂₃	
Deformation	3.4
250°C, 3h	2.1
850°C, 1h	0.9

4.2.2 Deformation Texture of Palladium and Palladium-Silver Alloys

The (111), (200), (220) pole figures from the sheet surface with 82% rolling reduction are shown in Figure 4.3. After large deformation, strong texture appears. The (111), (200), (220) pole figures after 40%, and 60% deformation are nearly the same as Figure 4.3. The rolling textures of palladium at 40%, 60%, 82% deformations are



Contour levels: 1, 3, 5, 7, 9, 11

Fig. 4.3 Pole figures of palladium after 82% cold rolling

represented mainly by $\{112\}\langle 111\rangle$ component with additional $\{124\}\langle 112\rangle$ component. The cold-rolling texture $\{112\}\langle 111\rangle$ component of palladium is developed and sharpened gradually as deformation strain is increased.

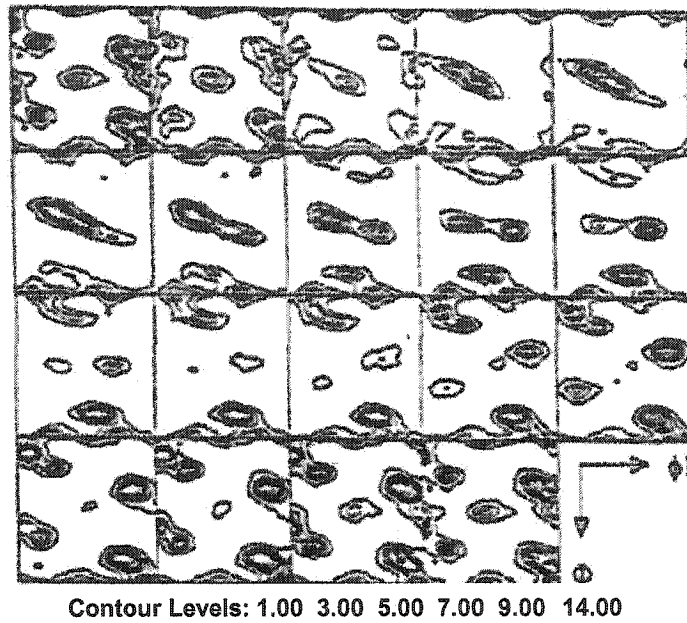


Fig. 4.4(a) Orientation distribution functions (ODF) of palladium after 40% cold rolling (Φ_2 cross sections)

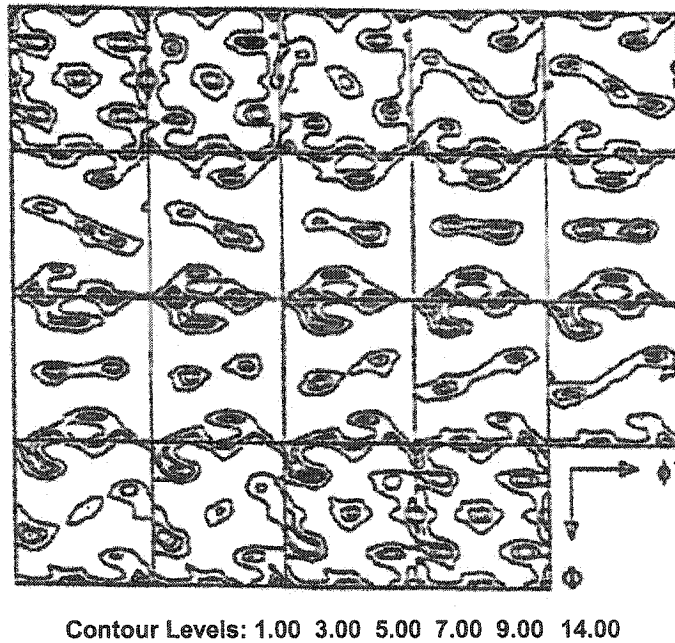
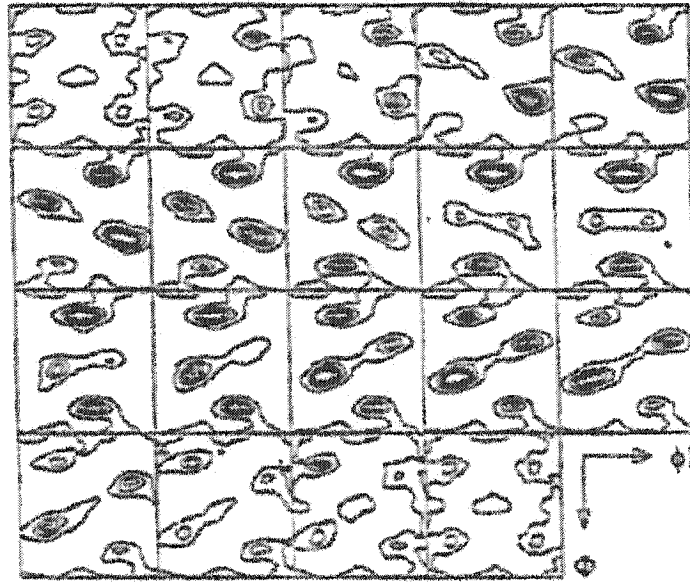


Fig. 4.4(b) Orientation distribution functions (ODF) of palladium after 60% cold rolling (Φ_2 cross sections)



Contour Levels: 1.00 3.00 5.00 7.00 9.00 14.00

Fig. 4.4(c) Orientation distribution functions (ODF) of palladium after 82% cold rolling (Φ_2 cross sections)

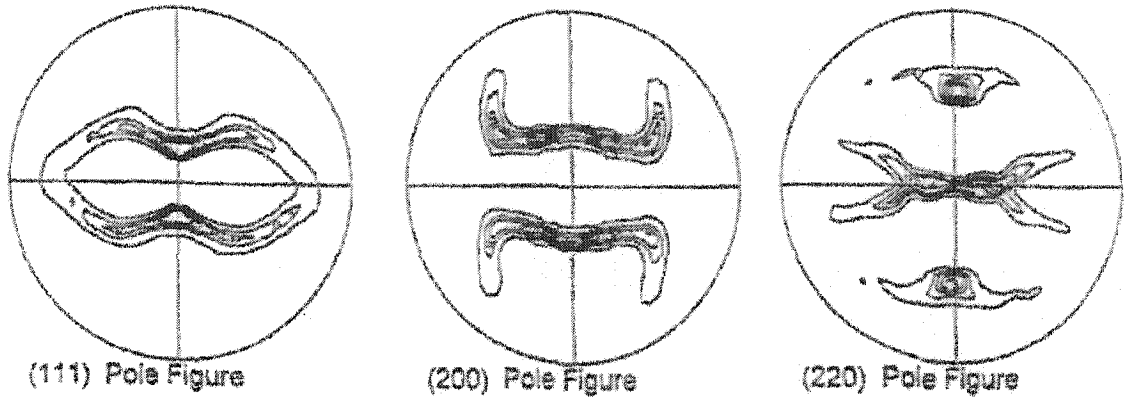
The orientation distribution functions (ODF) for palladium specimens are shown in Fig. 4.4. The summary of cold rolled textures obtained after large deformation in palladium and Pd-Ag alloys has been shown in Table 4.2

Table 4.2 Cold-Rolling Texture of Palladium and Pd-Ag alloys after large deformation

Materials	Texture	Stacking fault energy ^{c,d} mJ/m ²
Palladium	{112}<111> {124}<112>	180
Pd ₇₇ Ag ₂₃	{123}<111> {011}<112>	125
Pd ₂₀ Ag ₈₀ ^a	{112}<111> {011}<112>	30
Silver ^b	{011}<112>	24

a. Mirzaev 1996, b. Hu 1961, c. Rao 1968, d. Harris 1968

The (111), (200), (220) pole figures of Pd₇₇Ag₂₃ with 80% rolling reduction are shown in Figure 4.5. The rolling texture of palladium is mainly {011}<112>/{123}<111>. From Table 4.2, we can find that there are some differences between palladium and Pd-Ag alloy as well as pure silver. The pure palladium has a



Contour levels: 1, 3, 5, 7, 9, 11
Fig. 4.5 Pole figures of Pd₇₇Ag₂₃ after 80% cold rolling

{112}<111> texture and pure silver has a {011}<112> texture. The Pd₇₇Ag₂₃ alloy has a {011}<112> and a {123}<111> mixture texture. Pd₂₀Ag₈₀ has {011}<112> and {112}<111> texture. This means that the texture of this alloy has changed from {112}<111> for pure palladium to {011}<112> for pure silver.

Stacking fault energy plays an important role in determining deformation texture in fcc metals at room temperature. There are different stacking fault energy (SFE) values for palladium, silver and Pd-Ag alloy with fcc structure. Since the mean width of separation for extended dislocation varies inversely with the stacking-fault energy, cross-slip for close-packed crystals becomes increasingly difficult as the stacking-fault energy decreases (Murr 1975). Stacking fault energy influences the deformation mode, which will control texture development. Metal deformation is related to the active slip systems,

whose slip planes and directions will be determined by the metal's structure, temperature and deformation conditions. Sheet rolling is an approximation of a biaxial stress system. In fcc metals, the selection of independent shear systems will be made among twelve $\{111\} \langle 110 \rangle$ slip systems and twelve $\{111\} \langle 112 \rangle$ twin systems. The $\{111\} \langle 112 \rangle$ texture develops as a result of rotations of the tension and compressive axes caused by slip on the two systems with the highest resolved shear stresses under the bi-axial stress condition of rolling. Palladium and silver are fcc metals. Palladium has high stacking fault energy, which forms $\{111\} \langle 112 \rangle$ Cu-type texture. Silver has a low stacking fault energy, which essentially leads to the $\{110\} \langle 112 \rangle$ brass texture. For Pd-Ag alloys, the stacking fault energy will decrease when Ag concentration increase (Rao 1968, Harris 1968). This means that the deformation mode will change from pure slip to slip with twinning. So the Pd-Ag alloys should include a set of both $\{111\} \langle 112 \rangle$ and $\{110\} \langle 112 \rangle$ texture. As the Ag concentration increases in Pd-Ag alloys, $\{110\} \langle 112 \rangle$ texture component become stronger.

4.2.3 Annealing Texture of Palladium and Palladium-Silver Alloys

After annealing at 850°C , the texture of palladium and $\text{Pd}_{77}\text{Ag}_{23}$ will change. Orientation distribution functions (ODF) of Palladium after 82% cold rolling and annealing at 850°C for 1.5h has been shown in Fig. 4.6. The textures of palladium have changed from $\{121\} \langle 111 \rangle$ to $\{011\} \langle 100 \rangle$. Orientation distribution functions (ODF) of $\text{Pd}_{77}\text{Ag}_{23}$ after 80% cold rolling and annealing at 850°C for 1.5h has been shown in Fig. 4.7. The textures in annealed (850°C) materials are $\{113\} \langle 110 \rangle$ and $\{011\} \langle 122 \rangle$. A summary of textures of annealed palladium and Pd-Ag alloy is listed in Table 4.3. For Pd-Ag alloys, the deformed texture will not change $\{011\} \langle 211 \rangle / \{123\} \langle 111 \rangle$ after low

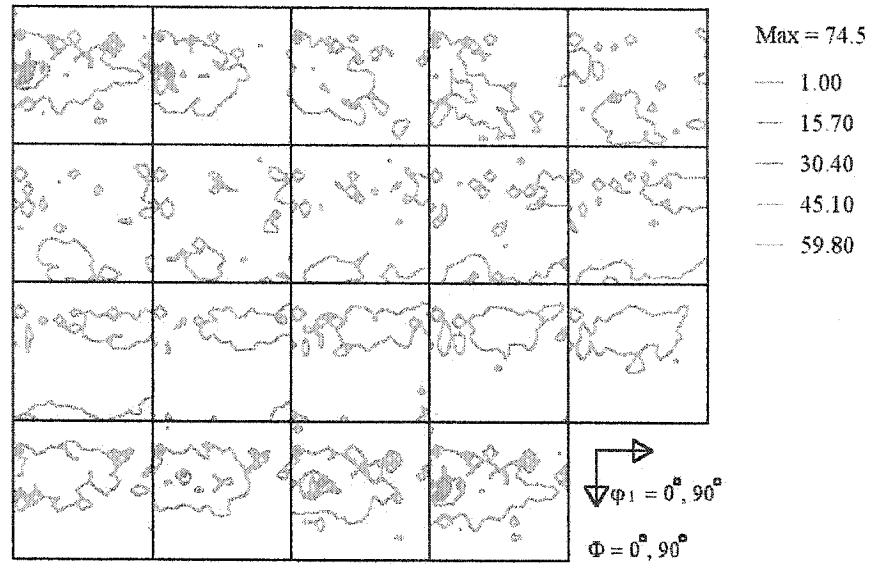


Fig. 4.6 Orientation distribution functions (ODF) of palladium after 82% cold rolling and annealing at 850°C for 1.5h

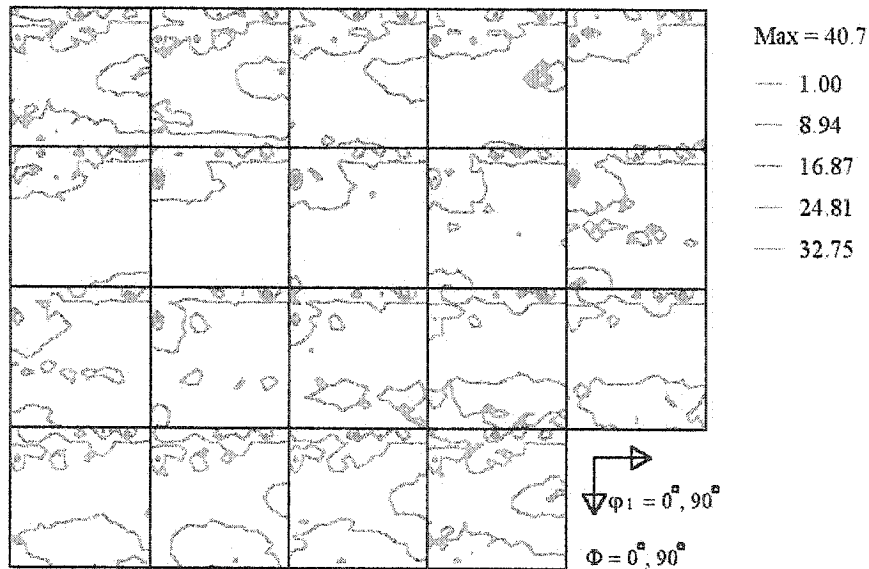


Fig. 4.7 Orientation distribution functions (ODF) of Pd₇₇Ag₂₃ after 80% cold rolling and annealing at 850°C for 1.5h

temperature annealing. In our research, the annealing temperature (850°C) is higher than the temperature of recrystallization. During annealing, the metals will have been

subjected to recrystallization. In recrystallization the dislocation density controls the stability of grains and determines which orientations grow at the expense of others. Deformation texture will influence recrystallization texture. Usually, an fcc metal with a low stacking fault energy after primary recrystallization produces $\{326\}\langle 835\rangle$ texture (Schmidt and Lucke 1979). After annealing at high temperature (600°C), $\{113\}\langle 332\rangle$ texture will be produced in 70:30 brass with high reduction (Duggan and Lee 1988). In this case $\{113\}\langle 110\rangle$ and $\{011\}\langle 122\rangle$ textures for $\text{Pd}_{77}\text{Ag}_{23}$ has been observed after annealing at 850°C , this texture is close to the brass texture. This means that adding silver to palladium will make the Pd-Ag alloy texture more similar to the silver texture.

Table 4.3 Recrystallization Texture of Palladium and Pd-Ag alloys

Materials	Texture
Palladium	$\{011\}\langle 100\rangle$
$\text{Pd}_{77}\text{Ag}_{23}$	$\{113\}\langle 110\rangle$ $\{011\}\langle 122\rangle$
$\text{Pd}_{20}\text{Ag}_{80}$ ^a	$\{011\}\langle 112\rangle/\{112\}\langle 111\rangle/\{001\}\langle 100\rangle$
Silver ^b	$\{113\}\langle 112\rangle$

a. Mirzaev 1996, b. Schmid 1950

4.2.4 Summary

1. The average grain size of palladium is 15-20 μm . High-density of dislocations with cellular substructure have been formed. The dislocation density is $2.9 \times 10^{12}/\text{cm}^2$ for palladium after 82% cold rolling and $3.4 \times 10^{12}/\text{cm}^2$ for $\text{Pd}_{77}\text{Ag}_{23}$ after 80% cold rolling.
2. The stacking fault energy has significant influence on deformation texture of Pd-Ag alloys. Pure palladium, with a higher stacking fault energy than silver, exhibits

{111}/<112> texture. When the silver concentration is increased, {110}<112> texture gradually appears and {111}/<112> texture gradually disappears in Pd-Ag alloys.

3. The recrystallization texture after annealing at 850⁰C is {011}<100> for palladium and {113}<110>/{011}<122> for Pd₇₇Ag₂₃. When the silver concentration is increased, recrystallization texture is changed.

4.3 Optimization of hydrogen permeation in palladium membranes

4.3.1 Hydrogen permeation measurements

Typical permeation data of build up transient for annealed palladium are shown in Fig. 4.8. The reproducibility of the successive transients after hydrogen discharge suggests that traps are not being changed during charging. The figure shows that the permeation current density initially rises rapidly and then changes slowly. When a certain value of the permeation current density is reached, the transient will be very stable and nearly constant. The relationship between steady anode current density and cathode

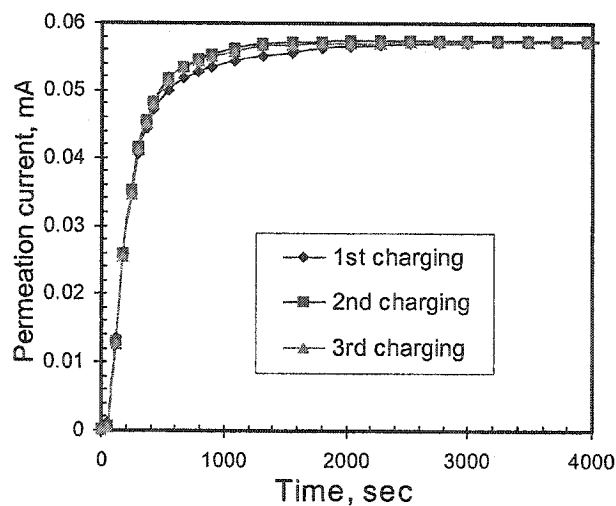


Fig. 4.8 Hydrogen permeation in palladium

current density has been shown in Fig. 4.9. When the charging current was increased, the permeation current increased in a linear fashion at first and then increased more and more slowly.

4.3.2 Optimization of Hydrogen permeation

The permeation efficiency (E_{PE}) can be defined as a percentage of the permeation current with respect to the charging current. From this definition, the permeation efficiency is expressed in equation 4.1.

$$E_{PE} = (I_{ss}/I_c) * 100 \quad (4.1)$$

Where I_c is the charging current density and I_{ss} is the steady state permeation anode current density. The permeation efficiency is also shown in Fig 4.9. It can be seen that permeation efficiency decreased with increased charging current. At around 0.01-0.15 mA/cm² of charging current, there is a plateau region. After this region, permeation efficiency decreased dramatically and became lower than 60%. In the plateau region, measurements of hydrogen diffusion coefficients are around 3.2×10^{-7} cm²s⁻¹, which is in

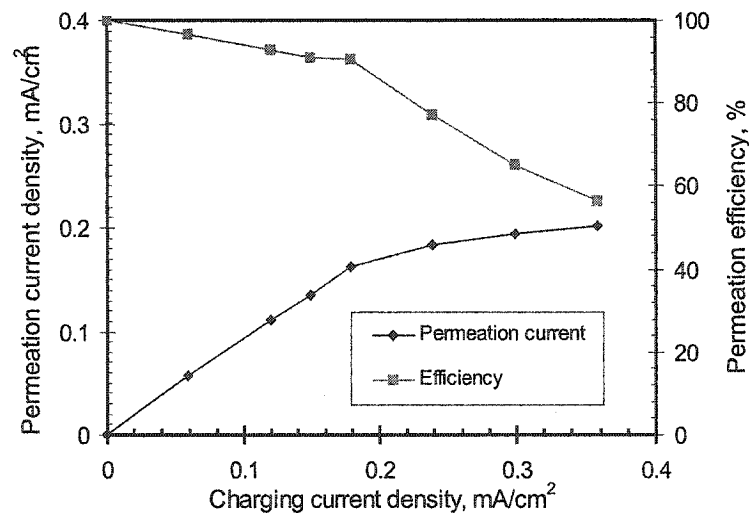


Fig. 4.9 Hydrogen permeation efficiency in palladium

good agreement with the literature (Early 1978). So the charging current density, 0.1 mA/cm^2 , has been chosen for further research.

The diffusion coefficients are $3.2 \times 10^{-7} \text{ cm}^2\text{s}^{-1}$ for annealed Pd and $2.9 \times 10^{-7} \text{ cm}^2\text{s}^{-1}$ for the annealed Pd₇₇Ag₂₃ alloy (Table 4.4). After the annealing process, the diffusion coefficients of Pd and Pd₇₇Ag₂₃ alloy increased. Those results are in agreement with previous reports (Sakamoto 1982, Bucur 1991).

To describe diffusion behaviors in more detail, the permeability and concentration of absorbed hydrogen have been introduced. The permeability (P) of hydrogen through a sample can be defined in equation 4.2.

$$P = (I \cdot L) \quad (4.2)$$

where I is the permeation current density and L is the thickness of a membrane. The equation 4.2 has been used to calculate the permeability to compare permeation data for specimens having different thickness. The concentration of absorbed hydrogen (C_0) at the input surface can be calculated from equation (3.5).

4.4 Effect of deformation of Pd and Pd₇₇Ag₂₃ alloy on hydrogen permeation

4.4.1 Effects of cold rolling on hydrogen permeation

The permeation transients of cold rolled and annealed Pd₇₇Ag₂₃ alloy are plotted in Figure 4.10. The anodic current density increases smoothly with increasing charging time and finally tends towards a constant. The permeation current of deformed samples increased more slowly than that in the annealed sample with the same thickness because of higher probabilities of hydrogen trapping. It can be concluded that deformation produced an imperfect structure with dislocations and point defects, which serve as

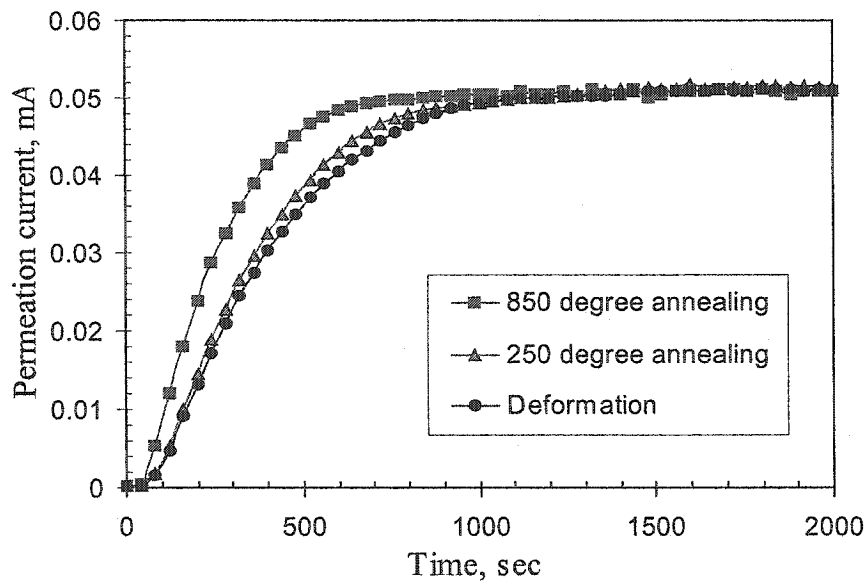


Fig. 4.10 Hydrogen permeation transients for Pd₇₇Ag₂₃ membranes

hydrogen trap sites. In the Pd₇₇Ag₂₃ alloy annealed at 250⁰C, the permeation current increases faster. The reason for this increase is that low temperature annealing leads to recovery and reduces residual stress in the sample, which permit hydrogen to diffuse

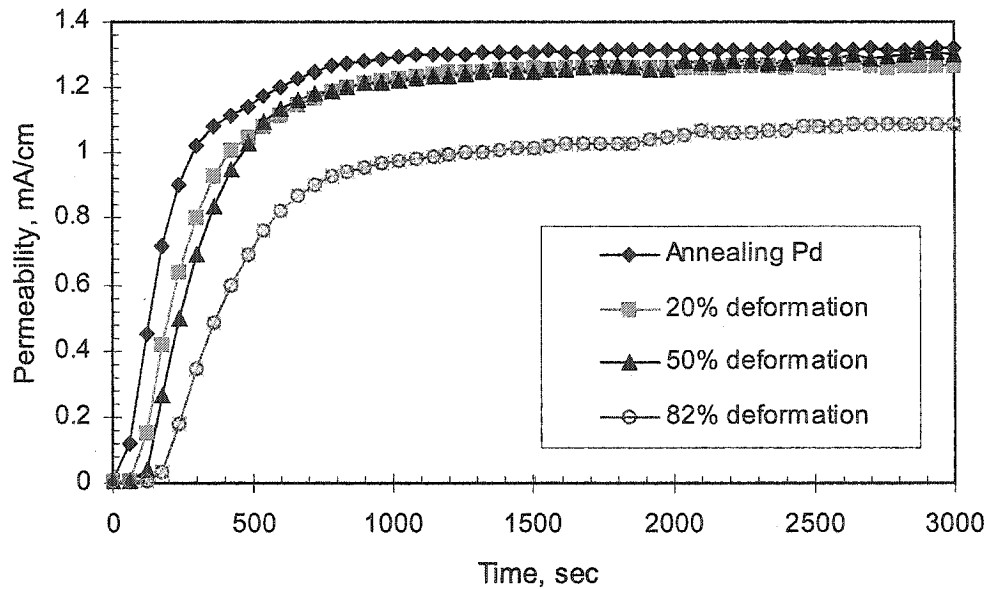


Fig. 4.11 Hydrogen permeation transients for palladium membranes

more easily than in the deformed state. The increase of the permeation current of the Pd₇₇Ag₂₃ alloy annealed at 850°C is the fastest among the three conditions. The annealing temperature (850°C) was above the recrystallization temperature of the Pd₇₇Ag₂₃ alloy and thus makes this alloy recrystallize and diminishes the number of imperfections. The Pd₇₇Ag₂₃ alloy that has fewer defects in the structure has faster hydrogen diffusion. The permeation transients of cold worked and annealed palladium are plotted in Figure 4.11. The trend here is similar to that observed in the palladium alloys in Fig. 4.10. At low deformation (20%), there are some small differences. When deformation increased to 50%, the permeation is evidently delayed. At 82% deformation, the permeation is still delayed but the changes are not so dramatic. This behavior shows that hydrogen occupies sites of low energy (deep traps) first and after saturation of these sites, hydrogen occupies the remaining sites as in well-annealed palladium.

The hydrogen decay curves for Pd₇₇Ag₂₃ alloy and palladium membranes are shown in the Fig. 4.12 and Fig. 4.13 respectively. For the annealed palladium, the hydrogen permeation current decreases faster than for the deformed one. The hydrogen

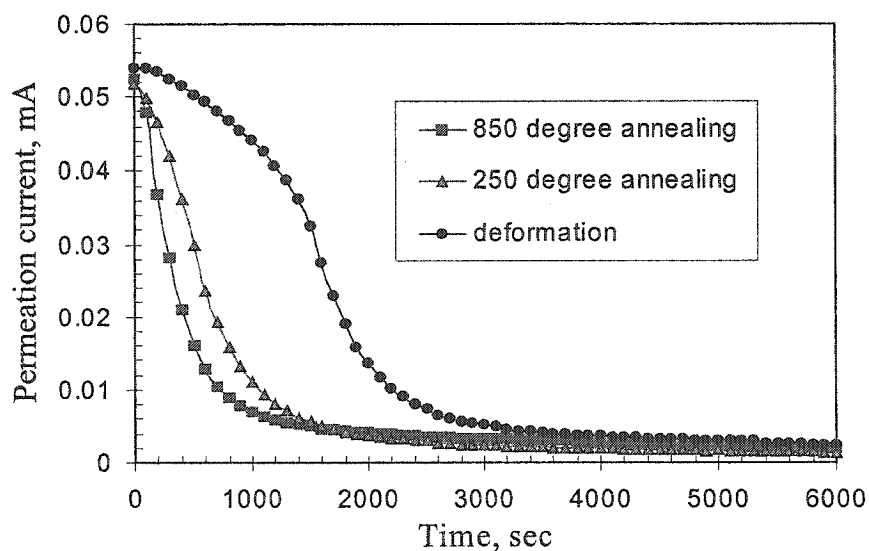


Fig. 4.12 Hydrogen decay for Pd₇₇Ag₂₃ membranes

diffusivity depends on the trap density, trap strength, degree of saturation of traps, and reversibility of trapping. After saturation of traps in palladium and its alloys, the hydrogen in palladium is more easily de-trapped because the binding energy of hydrogen to trap sites in fcc metals is a smaller fraction of the activation energy for diffusion. For the defect trap sites, hydrogen has to overcome additional energy to jump out. It takes time to finish this thermodynamic process. The permeation in deformed Pd₇₇Ag₂₃ decays more slowly. It is known that the lattice parameter of the Pd₇₇Ag₂₃ alloy has a higher value than that of pure palladium. So the palladium lattice expansion in the Pd₇₇Ag₂₃ alloy structure produces a lattice micro-strain (Sakamoto 1982). Thus both the deformation and the presence of the silver element may influence on hydrogen permeation in Pd₇₇Ag₂₃ alloy. Figure 4.13 illustrates the influence of both these factors.

The concentration of absorbed hydrogen at the input side is presented in Table 4.4. The hydrogen concentration decreased after annealing of deformed palladium and Pd₇₇Ag₂₃ alloy. This means that cold working increases the solubility of hydrogen in

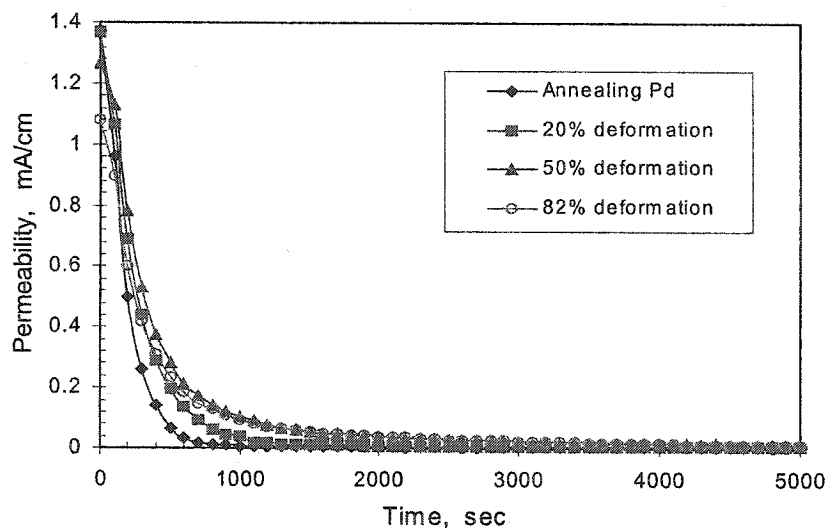


Fig. 4.13 Hydrogen decay permeation for palladium membranes

palladium due to the interaction of dissolved hydrogen atoms with the stress field of dislocations (Flanagan 1976).

4.4.2 Hydrogen trapping analysis for metals with defects

Octahedral sites in fcc palladium form an fcc lattice with the same lattice constant as the host lattice. The interstitial lattice is displaced with respect to the host lattice. There is one octahedral site per host atom. Neutron scattering and channeling experiments have shown that hydrogen in palladium occupies the octahedral sites (Dederichs 1980). The density of interstitial octahedral sites per unit volume, N_L , is calculated based on the number of interstitial octahedral sites per unit cell and metals' lattice parameters. N_L is 1.0193×10^{23} sites/cm³ for pure palladium and 9.9×10^{22} sites/cm³ for Pd₇₇Ag₂₃. In the near saturation limit and no full occupancy for the reversible traps, the influence of reversible trap densities on diffusion coefficients D_T is written in equation 4.5 (Oriani 1970).

$$D_T = D_L / (1 + KN_T / N_L) \quad (4.5)$$

where D_L is the lattice diffusion coefficient. It can be found that if the trap densities increase, the diffusion coefficient is lowered. K is trap strength, which is shown in equation 4.6.

$$K = \exp(-E_b / RT) \quad (4.6)$$

E_b is the binding energy for trapping. For Pd this energy is -26 KJ/Mol (Paul 1996). R is the gas constant. Combining equation 4.5 and 4.6 yields equation 4.7.

$$N_T = N_L (D_L / D_T - 1) \times \exp(E_b / RT) \quad (4.7)$$

Assuming $D_L = 3.2 \times 10^{-7}$ cm²/s for palladium (Early 1978) and $D_L = 3 \times 10^{-7}$ cm²/s for Pd₇₇Ag₂₃ (Bucur 1991) at room temperature, the trap density can be calculated

and is listed in Table 4.4. The results show that the trap density decreases after annealing palladium and Pd₇₇Ag₂₃. When annealed at 250⁰C, the trap density is reduced by about 50%. For a Pd₇₇Ag₂₃ alloy well annealed at 850⁰C, the trap density is reduced by two orders of magnitude. The trap density of palladium annealed at 850⁰C also decreases to nearly half of the density in 20% deformed palladium. This confirms that annealing can decrease trapping of hydrogen for palladium and Pd₇₇Ag₂₃ alloys.

Table 4.4 Hydrogen diffusion and trapping parameters of palladium and Pd₇₇Ag₂₃ alloys

Materials	Apparent Diffusion Coefficient, D × 10 ⁻⁷ [cm ² / s]	C ₀ × 10 ⁻⁵ [Mol/cm ³]	Trap Density, N _T × 10 ¹⁷ [cm ⁻³]
Pd			
850 ⁰ C, 1.5h	2.6	4.5	4.0
Deformation			
20%	2.4	5.5	7.1
50%	1.7	6.8	23.7
82%	1.6	7.5	24.1
Pd ₇₇ Ag ₂₃			
Deformation			
250 ⁰ C, 3h	2.2	6.1	9.5
850 ⁰ C, 1.5h	2.9	4.5	0.12

4.4.3 Summary

1. The study of hydrogen permeation in deformed palladium and Pd₇₇Ag₂₃ has shown that hydrogen permeation has been delayed because hydrogen trap sites have been introduced by deformation. When increasing the amount of deformation in palladium,

hydrogen permeation in palladium is delayed even more. The annealing of deformed palladium and Pd₇₇Ag₂₃ at 250⁰C reduces the number of trap sites, so permeation is faster than in the deformed metals. The annealing of deformed palladium and Pd₇₇Ag₂₃ at 850⁰C makes hydrogen diffusion faster. Recrystallization annealing reduces the number of trap sites and allows recovery of the hydrogen permeation characteristics in palladium and palladium alloys.

2. After deformation and annealing, palladium and Pd₇₇Ag₂₃ have different hydrogen decay characteristics. The annealed metals release hydrogen more rapidly than the deformed metals. The Pd₇₇Ag₂₃ alloy needs more time to release hydrogen because of combining effects of deformation and the lattice distortion. The solubility in deformed palladium and Pd₇₇Ag₂₃ is increased by deformation.
3. Time lag measurements of deformed palladium and its alloys established that the traps induced by deformation could be saturated. The trap densities in palladium rapidly increase from 20% to 50% deformed specimens, and then increase rather slowly to $2.41 \times 10^{18} \text{ cm}^{-3}$. The trap density is $1.44 \times 10^{18} \text{ cm}^{-3}$ for deformed Pd₇₇Ag₂₃ alloy. The dislocations and local residual stress introduced by deformation are thought to be trapping sites for hydrogen.

4.5 Simulation of hydrogen trapping in metal membranes

4.5.1 Trap mechanism analysis and trapping maps

When a metal membrane has been charged with hydrogen, hydrogen will be absorbed into the membrane and diffuse through it. If there are defects in this membrane, hydrogen will be trapped in defects. From the results presented in last two section (§4.2

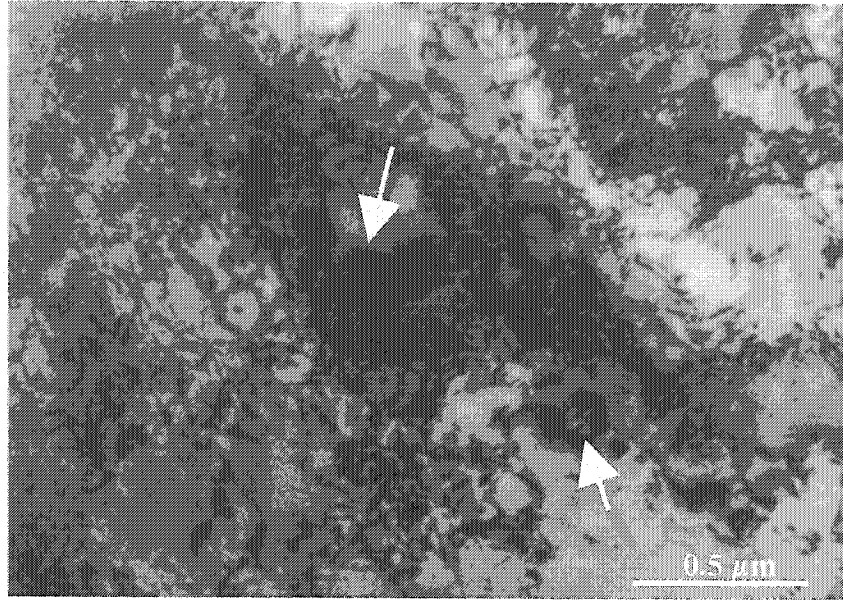


Fig. 4.14 TEM microstructure of Pd after hydrogen charging

and §4.3), it was concluded that deformation produces a high-density of dislocations, which normally serve as hydrogen traps in metals. A transmission electron microscope (TEM) image of 82% deformed palladium after hydrogen charging is shown in Fig. 4.14. High-density dislocations still exist in palladium. Some dislocation sites may serve as traps for hydrogen atoms. There are evidences that hydrogen can be trapped by the dislocations in fcc metals (Brass 1998, Heuser 1998). Because the volume of atoms at grain boundaries in Pd is very low (<1%), the trapping effects of grain boundaries are less important than that of dislocations. Therefore, it is reasonable to disregard the effect of grain boundaries or count the trapping effects in grain boundaries as a part of dislocations without underestimation. As a result, the total defects for trapping only include

dislocations. For simplicity, in latter discussions, only dislocations will be referred to as

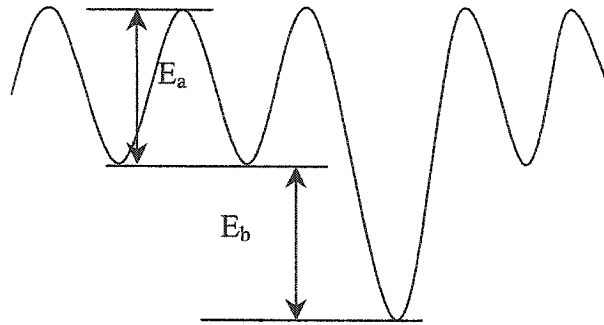


Fig. 4.15 Energetic schematic of hydrogen diffusion with trapping sites

defects. To simulate hydrogen trapping, we consider two kinds of lattice sites (normal and defect sites), which have different time of hydrogen residence (Fig. 4.15). The majority of sites available for occupancy by hydrogen atoms are normal lattice sites having activation energy of diffusion, E_a . The remaining sites are the defects acting as trapping sites, which have additional trap binding energy, E_b . The total energy for a hydrogen atom to jump out off a trap site is $E_a + E_b$, which represents a high-energy barrier for hydrogen escape. Hydrogen trapping phenomenon is due to attractive interaction between the dissolved hydrogen atoms and defects. The main deformation defects are dislocations because palladium is a single phase and the dislocation density after deformation is very high, which have been proved by TEM results in palladium (Fig. 4.2). In previous research, almost all attempts (chapter 2) used to explain hydrogen trapping were based on the continuum diffusion approximations by solving the diffusion equations with some special boundary conditions. Such approach may not be adequate approximations for the trapping on the atomic scale (Flynn 1964). Thus, the random walk method has been used in this work to deal with the effects of trapping on hydrogen

diffusion. Diffusivity is calculated based on the time and average distance that a group of hydrogen atoms have migrated from their initial sites. As it was already mentioned, lattice sites in the sample are divided into normal and trap sites. Following this concept, a computer sample with dislocation defects distributed randomly is generated according to the estimation volume of trap sites. This means that trap sites are randomly distributing in the computer sample. The cross-section of the computer simulation sample represents the distribution of dislocations, and will be called a trapping map (Fig. 4.16). In the trapping map, number 1 represents defect sites, which means “True” and trapping sites exist according to a binary digit system. Number 0 represents normal sites, which means “False” and represents non-trapping sites.

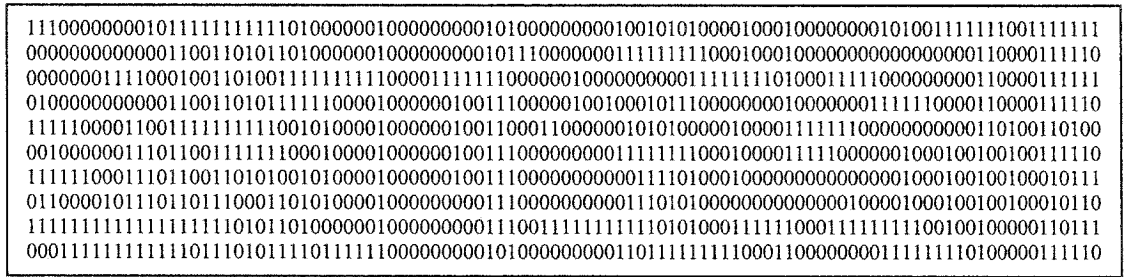


Fig. 4.16 Schematics of hydrogen trapping map in the metal membrane

4.5.2 The model description of hydrogen trapping

For most of the permeation experiments, hydrogen has been charged in the direction perpendicular to the membrane plane. According to recommendations by Hutchings (1993), the metal membranes specimens must have a ratio larger than 1:10 of the specimen thickness to the diameter of charging area, to have reliable hydrogen permeation measurements. Actually, our experiments used 1:40 to 1:200 ratios. This means that hydrogen diffusion is mainly through the direction perpendicular to the

membrane. The random walk method has been used to evaluate hydrogen diffusion. By checking the passing and residence time in the sample for individual hydrogen atoms, statistical total hydrogen flux has been obtained and has been compared to real experimental data. To introduce dislocation defects, the computer simulation sample has two dimensions, which are same as the cross-sections of metal membrane samples. In the computer sample, the length and the width correspond to the permeation area size and the thickness of a metal membrane respectively. The size of the computer simulation sample was set to a length of 100 units and a width of 10 units with 10:1 ratio, which is same as the ratio of the diameter of permeation area to the thickness of the metal membrane sample. Actually, the length of the computer simulation sample can be 1000 units or more, as long as the ratio of the length to the width of the computer sample is larger than 10:1. In order to simplify the situation, dislocations are presented in vertical or horizontal lines connecting defect sites with random lengths between 1 and 10 units. The dislocation or grain boundary traps will become saturated when certain amounts of hydrogen are captured by the traps (Wert 1983). After traps are saturated with hydrogen atoms, other hydrogen atoms can diffuse through the trapping sites in the same way as they do through the normal sites. We assume that the trapping site will become saturated after only one-hydrogen atom occupies the site, which means only one-hydrogen atom resides in one trapping site at one time. In reality, a trapping site may hold more than one hydrogen atom to become saturated. However, this makes no difference because the simulation is qualitative. The shape of the permeation curve is the same no matter how many hydrogen atoms saturated the trapping site. Therefore, this model represents all situations.

4.5.3 Simulation details and process of hydrogen permeation

In §4.5.1 and §4.5.2, the main idea of the present trapping model have been discussed and trap maps have been produced. Now, it is necessary to introduce more details to be able to run this simulation. Five conditions should be clarified to build the simulation model of hydrogen permeation.

1. Before charging with hydrogen, there is almost no hydrogen in the metal membranes. This is a normal case because residual hydrogen in the membrane has been extracted by holding a constant anodic potential at the exit side for a long time. The extraction of hydrogen is a standard procedure for electrochemical permeation. The boundary condition for hydrogen permeation assumes a constant hydrogen pressure on the entry side. When the thickness of the Pd membrane is over $50\mu\text{m}$, there is less than 100% of the charged hydrogen appearing on the exit side (Schuldiner and Hoare 1956). Even through a palladium membrane has been charged galvanostatically, it still can hold enough hydrogen on the entry side for hydrogen permeation to take place. The hydrogen concentration at the exit side is always zero for permeation since the exit side is held potentiostatically at a sufficient potential to ensure that all hydrogen from the membrane interior is instantly oxidized (Atrens 1980, Boes 1976, Tsubakino 2000).
2. As it was mentioned before, the volume fraction of grain boundaries in polycrystalline Pd is very low (<1%) and the trapping effects of grain boundaries are not as pronounced as trapping at dislocations. In this case only lattice diffusion is dealt with. The main attention focuses on hydrogen trapping at dislocations in a metal membrane.

3. There exists an equilibrium between hydrogen atoms at trapping sites and normal lattice sites (Oriani 1970). Sometimes, the thermal energy is large enough for the hydrogen atoms to jump out of the trap sites. The probability of hydrogen escaping a trapping site is calculated from $\exp(-E_b/kT)$. E_b is the binding energy, which represents the barrier level and depends on the type of defects. After jumping out from trapping potential well, the hydrogen atom will diffuse normally. The trap site is saturated after one hydrogen atom fills this site. When one hydrogen atom occupies a site, this site is now considered as a non-trapping site for hydrogen. This means that trapping effects will diminish in the sample.
4. The simulation run 20 loops at the plateau region for hydrogen permeation flux, to make sure that the permeation curves really reached steady state. Then the simulation starts the desorption process, which is the hydrogen releasing process. When a permeation flux is reduced to 1% of the steady state value, the whole simulation process stops. Although the criteria is set up as 1%, it can be changed to 2% or 3%, which will generate similar results.
5. The random walk process has been used to simulate hydrogen diffusion through membranes. The flux is calculated by counting the number of hydrogen atoms exiting the membrane in a given interval of simulation time at the exit side with a certain amount of hydrogen charged at the entry side. By plotting flux vs. simulation time, permeation curves have been obtained.

The diagram illustrating the simulation process is shown in Fig. 4.17. Accordingly, there are seven steps to simulate the trapping process.

Chapter 4: Effects of Deformation on Hydrogen Permeation in Pd and Pd-Ag Membranes

- (1) Input parameters: this includes filename, percent volume of trapping sites, binding energy, E_b , and the temperature in K.
- (2) Produce trap map: this produces dislocations with vertical or horizontal lines with random lengths between 1 and 10 units.
- (3) Hydrogen diffusion with trapping: this traces hydrogen atoms diffusion in metals with trapping sites.
- (4) Flux calculation: this counts the amount of hydrogen atoms passing through the membrane at a given time interval and compares the flux with the previous time.
- (5) Charging hydrogen stops and desorption process starts: this stops hydrogen supply and starts the decay process when a constant flux plateau has been reached and the flux does not change much for 20 times.
- (6) Stop desorption process: this stops desorption and starts saving files when the flux reaches 1% of steady state flux value.
- (7) Save a file and end the processing: this will save calculation results in a file named by the user and end the whole program.

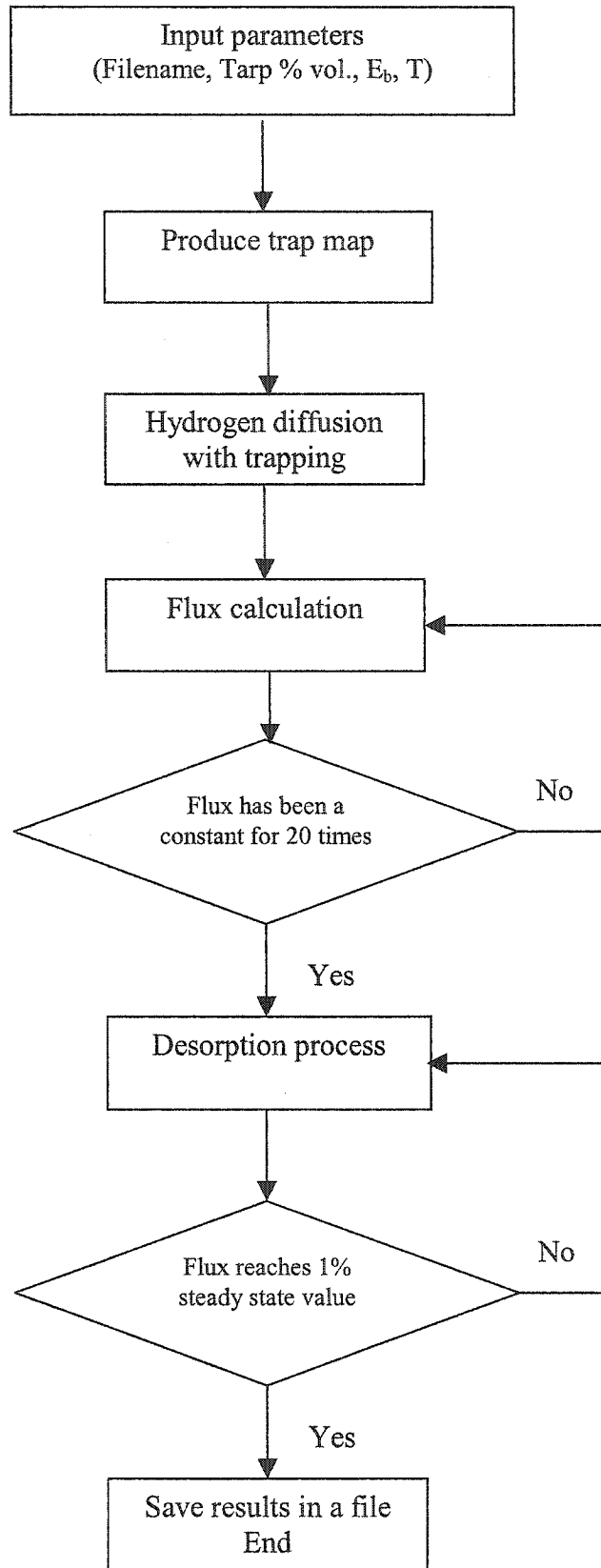


Fig 4.17 Procedure of hydrogen diffusion simulation

4.5.4 Comparison hydrogen trapping behavior with the model

In order to calculate the transient hydrogen permeation curve, the binding energy (E_b) should be determined. The binding energy is related to the character of materials and the kind of defects in the membranes. Here 0.1 eV has been chosen as E_b for palladium with dislocations as defects, which is a normal case for fcc metals (Young 1998). By changing the trapping volume, different hydrogen permeation curves have been obtained. With the same kind of defects (same binding energy), hydrogen permeation processes have been delayed when trapping volume increased. Also, hydrogen decay curves have similar trends. Increasing trapping volume has retarded hydrogen release from the exit side. When comparing the present results of simulation (Fig. 4.18) with the experiments (Fig. 4.10-4.13), it can be seen that they correspond with each other. When the percent of deformation increases to produce more dislocations, the trapping volume increases as well. So this causes a hydrogen permeation delay, which

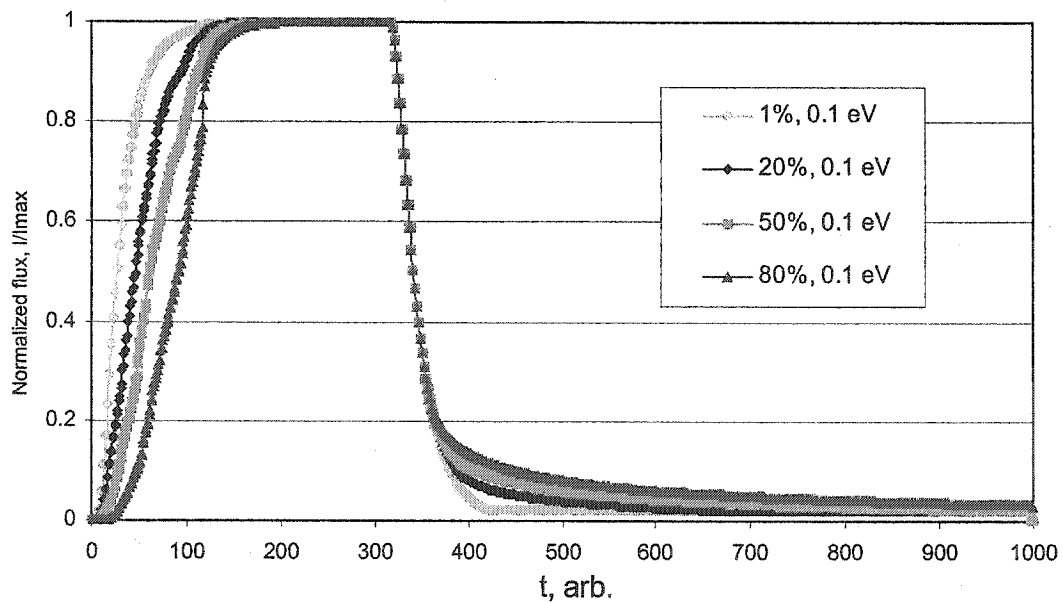


Fig. 4.18 Simulation results of metal membranes with trapping

means trapping sites hold hydrogen for a longer time than in normal sites. Both experimental hydrogen permeation and hydrogen decay curves show the same trends when trapping sites increase as the simulation presented. This validates the model for hydrogen permeation with trapping. Furthermore, using this model can evaluate the effect of binding energy on hydrogen permeation (Fig. 4.19). From Fig. 4.19, it can be seen that higher binding energy delays hydrogen permeation and decay. The time-lags obtained from the model and the experiments are in a linear relationship (Fig. 4.20). One can change three parameters in the model: binding energy, temperature, and trapping volume at the same time. This is one of the many advantages in using this model for the estimation of hydrogen permeation and transport. When bulk data are available, different parameters of the model can be obtained. This model can generate results immediately. The calculation time of a permeation curve is less than 20 seconds in a 200 MHz PC computer. If a sample has an initial hydrogen concentration before charging, the model

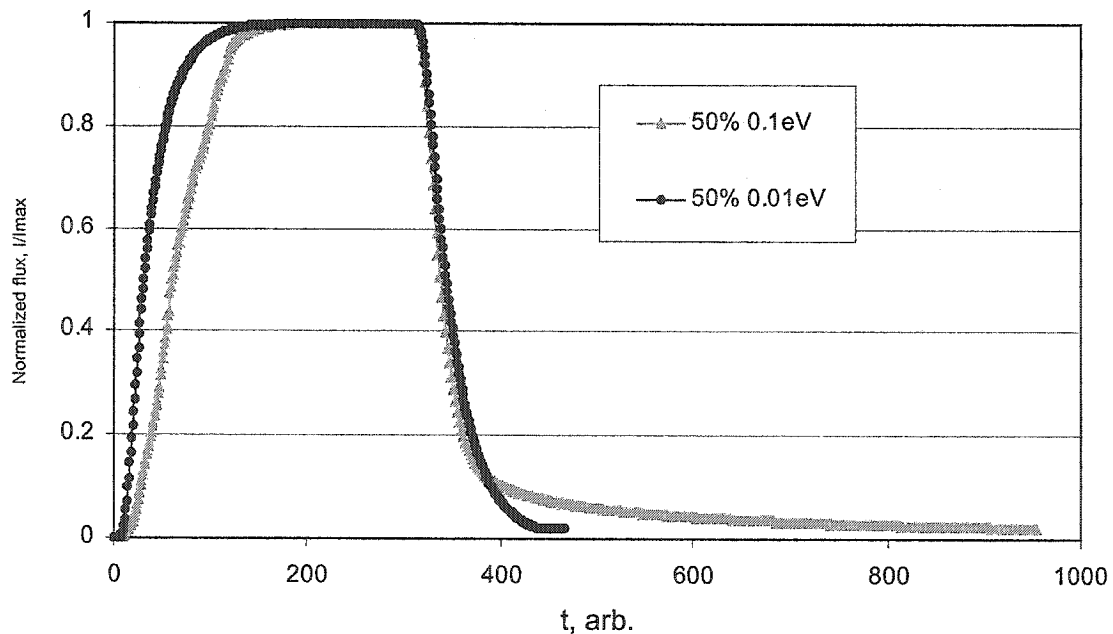


Fig. 4.19 Effect of binding energy on hydrogen permeation

can still be used for the simulation of hydrogen permeation by adjusting the trapping volume. Of course, one should know the former charging condition and the amount of hydrogen in the sample in order to get a volume of trapping sites.

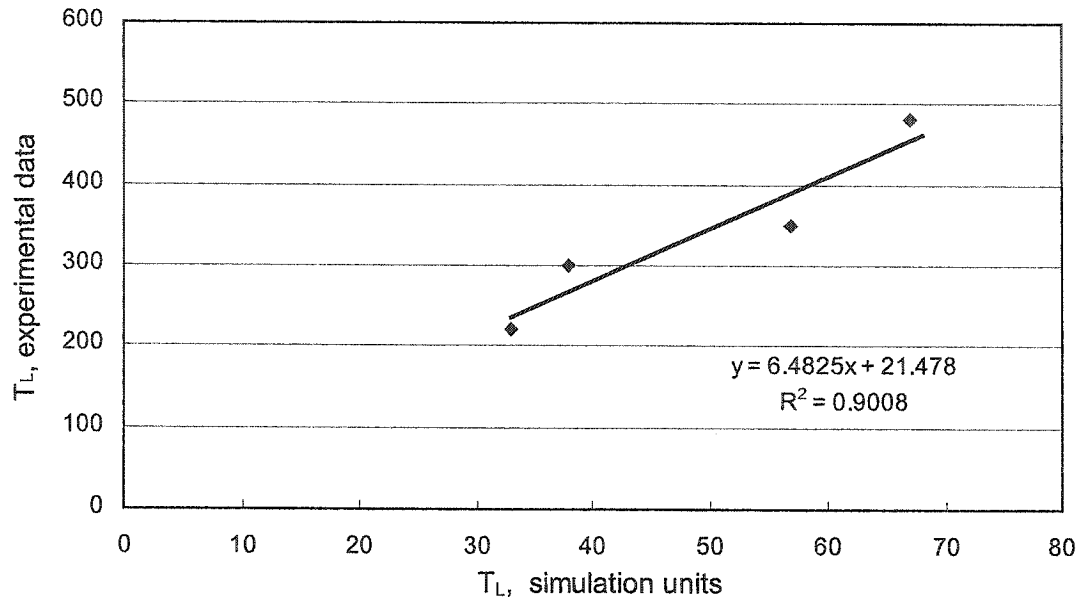


Fig. 4.20 Comparison of simulation with experiment data for Pd hydrogen permeation

4.5.5 Summary

1. The model is built to simulate trapping mechanisms and diffusion. The experimental data are in good qualitative agreement with the model. The model can explain the effects of trapping on hydrogen permeation through thin membranes.
2. The model can generate random trapping site distributions and diffusion profiles. The simulation clearly generates results very quickly compared to experiments. Three parameters are used as an input data to the simulation: the binding energy, temperature, and trapping volume. Those three parameters can be changed at same time for different simulation conditions.

3. If a sample has an initial hydrogen concentration before charging, the trapping volume has to be adjusted accordingly. One should know the former charging conditions and the amount of hydrogen in the sample in order to get the correct trapping volume.

CHAPTER 5

EFFECTS OF GRAIN SIZE ON HYDROGEN PERMEATION IN NICKEL MEMBRANES

5.1 Introduction

Grain boundaries are very important structural components of polycrystalline materials, especially in nanocrystalline materials. From nanometer size grain to micrometer size grain, the volume fraction of grain boundaries in materials will dramatically change. There is some evidence that grain boundaries increase interstitial atoms diffusion (Gleiter and Chalmer 1972). Therefore grain boundaries should play an important role in hydrogen diffusion through metal membranes. As a result, a change in the volume fraction of grain boundaries would influence hydrogen permeation. In our study, different grain size nickel samples have been obtained by annealing nanocrystalline nickel membranes. Through texture analysis and grain size measurements, information about grain boundary character distribution has been

obtained. The relationship between the grain size, grain boundary misorientation distribution and hydrogen permeation through nickel membranes has been established.

5.2 Microstructure and texture in nickel membranes

5.2.1 Effect of annealing temperatures on grain size in nickel membranes

When the annealing temperature is above a certain value, nanocrystalline nickel grain will grow. Accordingly our membrane samples were annealed at different temperatures between 200-900 °C and held at these temperatures for 1h. The annealing temperature was increased in 100°C intervals. The relationship between the grain size of nickel membranes and the annealing temperature is shown in Fig. 5.1. The grain size of the sample annealed at 500 °C was too small to measure using optical microscopy. This is the lowest annealing temperature that will lead to a very quick recrystallization in nickel membranes. Grain growth has occurred at temperatures higher than 500°C (Figure 5.1). From an X-ray diffraction peaks analysis of the annealed nickel membranes, one can see

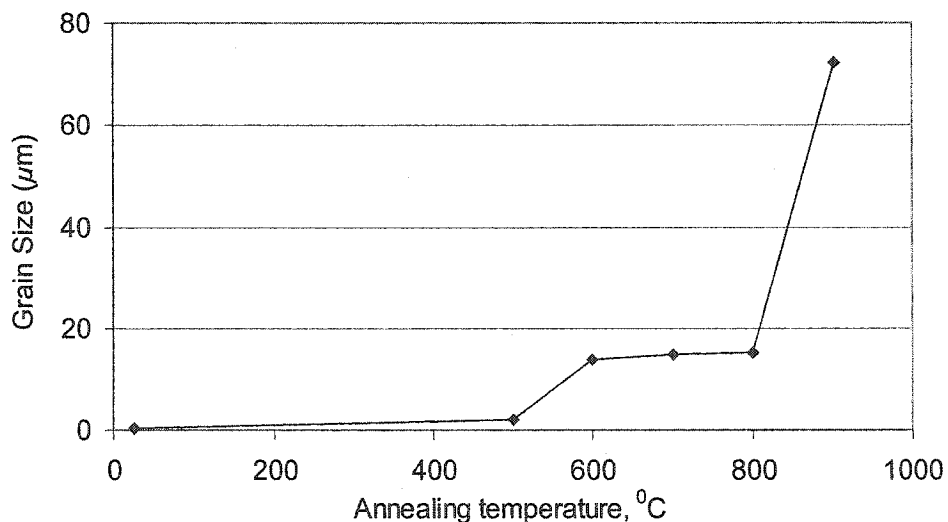


Fig. 5.1 Grain sizes change with annealing temperature

that the broadening of peaks is smaller than in the sample with nanocrystalline grains. After annealing between 500⁰C and 900⁰C, diffraction peaks do not show grain size broadening. The sample annealed at 900⁰C was fully recrystallized and had much larger grains than the sample annealed at 800⁰C. The temperature of 900⁰C is the upper temperature limit for annealing nickel membranes with 70 μ m thickness because at this temperature the grain size becomes bigger than the nickel membrane thickness.

5.2.2 Effect of annealing temperatures on grain orientation in nickel membranes

The orientation distribution functions (ODF) of nickel membranes have been calculated from measured pole figures. The original nanocrystalline nickel membrane has a very strong (100) fiber texture (Fig. 5.2), which is a typical texture of nickel membranes produced by electrodeposition. When nanocrystalline nickel membranes have been annealed at 200⁰C or 300⁰C, the (100) fiber texture is still present, but the intensity of this

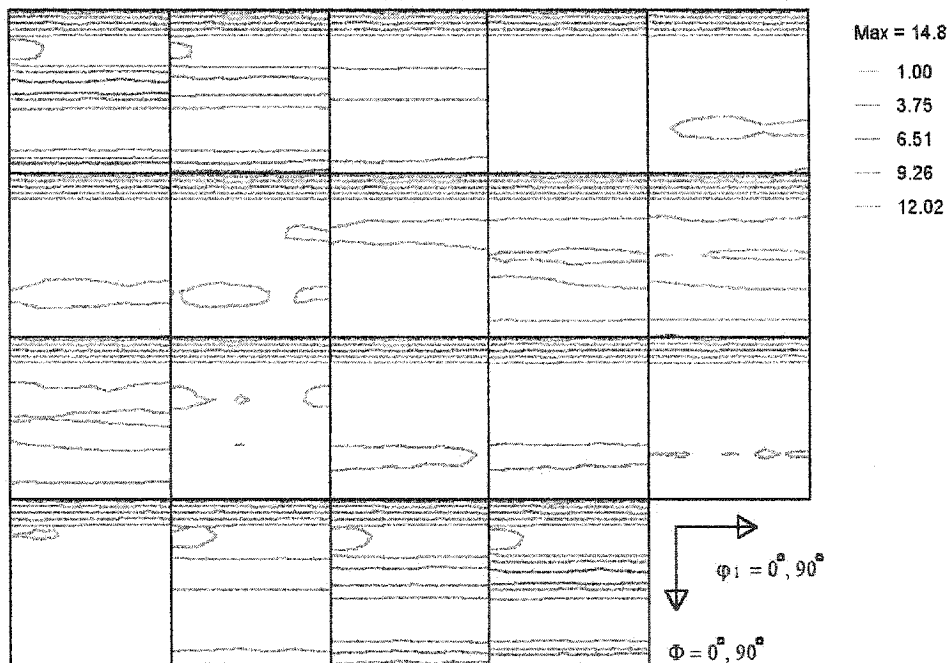


Fig. 5.2 Texture (ODF) of nano-nickel membranes

texture decreases. When annealed at 400⁰C, the texture of the nickel membrane is changed to the (111) texture, however the (100) fiber texture component is still present

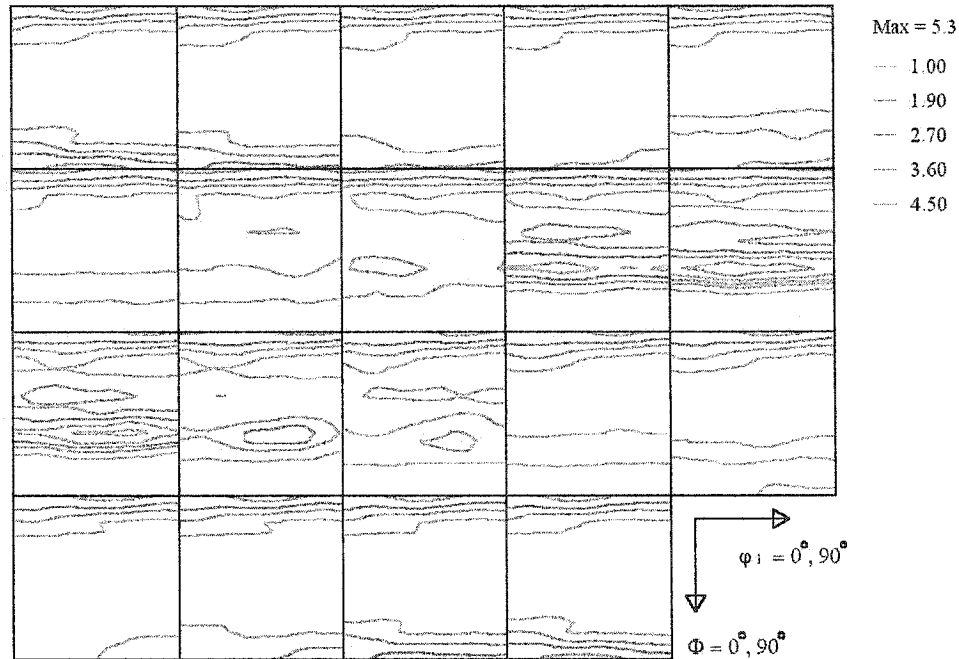


Fig. 5.3 Texture (ODF) of nickel membranes annealed at 400⁰C

(Fig. 5.3). The strength of the (100) fiber texture in the annealed nickel membrane is weaker than pre-annealed sample. Annealing between 400⁰C and 700⁰C leads to transformation of texture from the deposition fiber texture to the recrystallization texture. After annealing nanocrystalline nickels between 700⁰C and 900⁰C, a strong recrystallization texture is observed in the ODFs presented in Fig. 5.4 and Fig. 5.5. The fiber texture developed during the deposition becomes weaker as the annealing temperatures increases. The original texture cannot be seen after annealing at temperatures higher than 700⁰C.

The different textures will influence changes in the grain boundary character distribution (GBCD) of nickel membranes after annealing. The GBCD is calculated from the ODF (Morawiec 1993). When comparing the misorientation of the grains at various

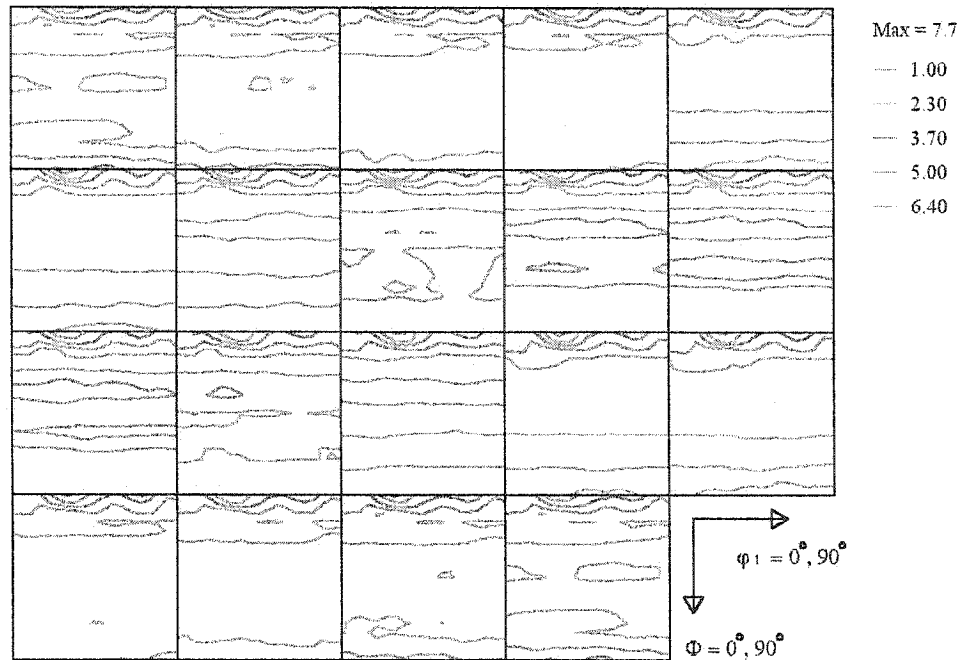


Fig. 5.4 Texture (ODF) of nickel membranes annealed at 700°C

annealing temperatures, the differences of grain boundary character distribution of nickel membranes are not significant in general (Figure 5.6). Following the accepted classification of grain boundary types, low angle (0° - 15°), middle angle (30° - 45°) and high angle (45° - 65°) grain boundaries have been identified by the misorientation of grains. A slight increase in the percentage of high angle (45° - 65°) grain boundary occurs, as the annealing temperature is increased (Figure 5.7). There is also a small decrease in the percentage of low (0° - 15°) and middle angle (30° - 45°) grain boundaries. Diffusivity is related to grain misorientation (Gleiter and Chalmer 1972). Normally, high angle grain boundaries have high diffusivity and low angle grain boundaries have low diffusion coefficient. Because the changes in fractions of low and middle angle boundaries are very minimal, these changes should not lead to a significant change in the diffusivity. The slight change in misorientation between grains is followed by a decrease of volume percent of grain boundaries during annealing of nanocrystalline nickel membranes.

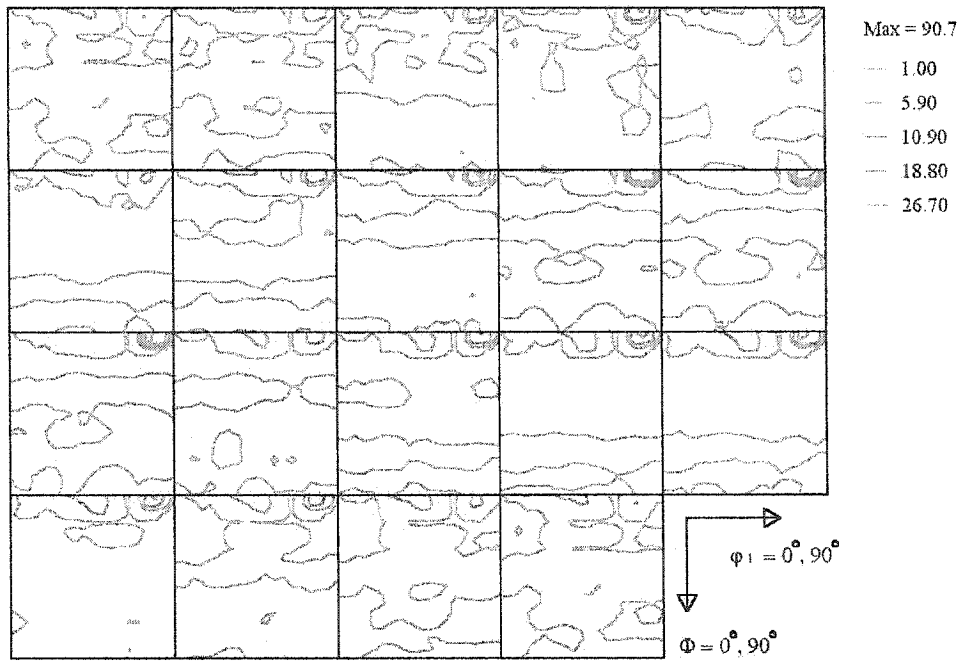


Fig. 5.5 Texture (ODF) of nickel membranes annealed at 900°C

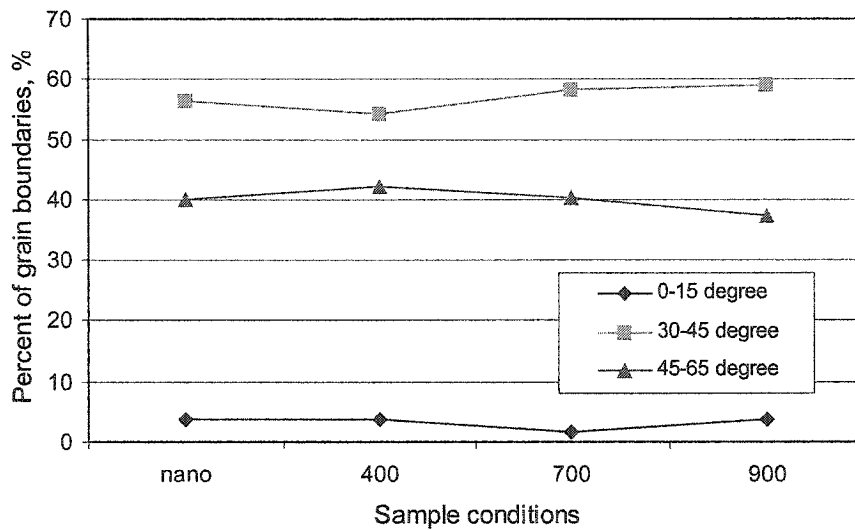


Fig. 5.7 Percentage of different classes of grain boundaries in nano-nickel and annealed nickel membranes after different annealing temperatures for 1h

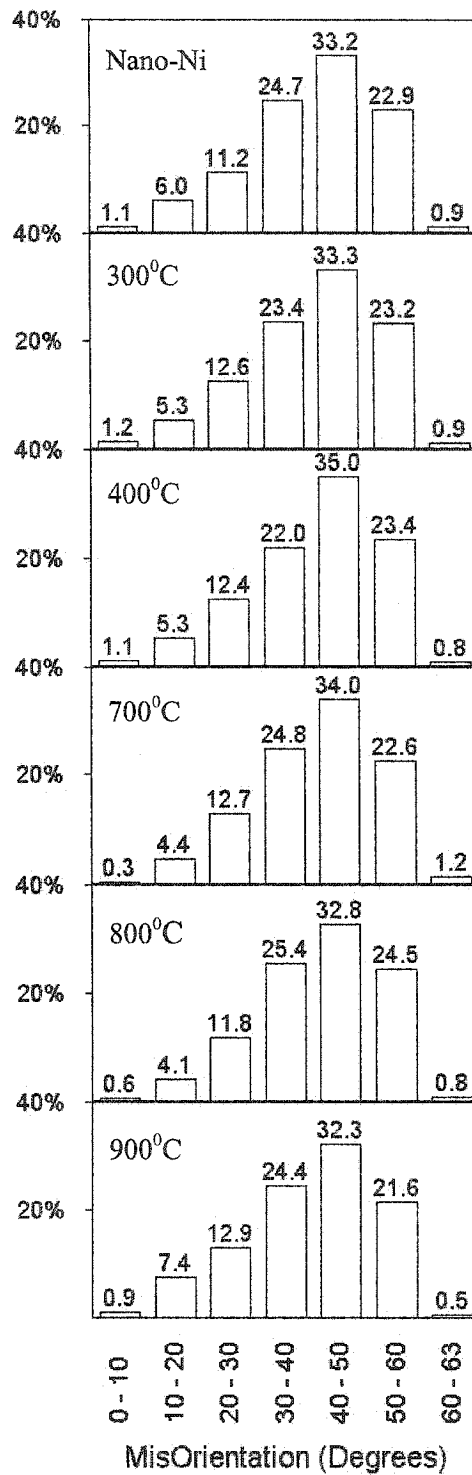


Fig. 5.6 Grain boundary character distributions (GBCD) of nano-nickel membrane and nickel membranes after different annealing temperatures

5.3 Effects of grain size on hydrogen permeation in membranes

5.3.1 Effects of charging current on hydrogen permeation in membranes

The relationship between steady anode current density and cathode current density (I_c) is shown in Fig 5.8. When the charging current increases, the permeation current increases more rapidly, and then reaches a plateau area. The higher the charging current, the faster hydrogen penetrates the membrane. The steady state permeation current increases with increasing charging current. According to equation (4.1), the efficiency definition, charging efficiency, permeation current and diffusivity have been plotted in Fig. 5.9. It can be seen that permeation efficiency for nano-nickel membranes decreased, but diffusion coefficients and permeation currents increased when the charging current increased. Unlike palladium with micron size grains, the difference between the lowest and highest value of the diffusivity differs by a factor of 2. So increasing hydrogen supply in the entry surface of nano-nickel membranes does raise the

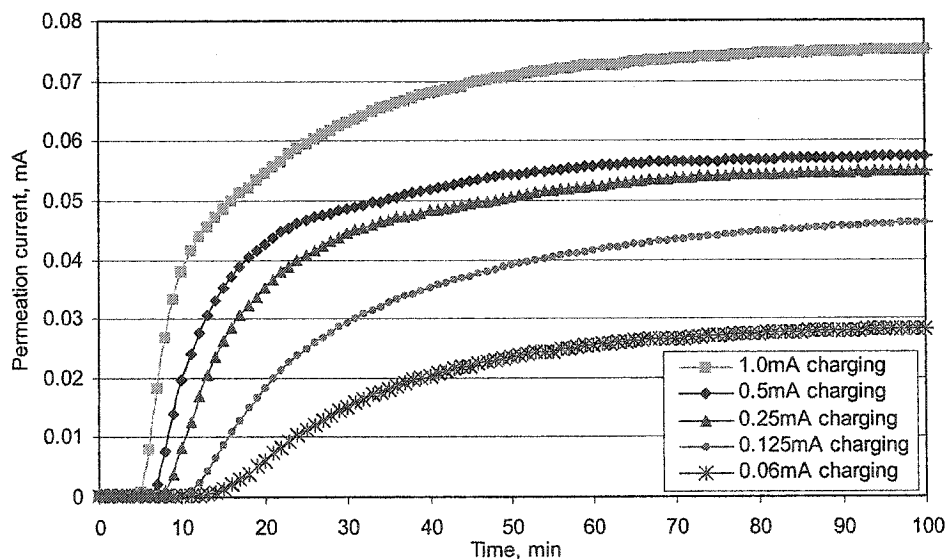


Fig. 5.8 Permeation transients for nano-nickel membranes with different charging current

hydrogen diffusivity (Fig. 5.9). Those observations are similar to a diffusivity dependence on hydrogen concentration in nano-palladium reported by Mutschele (1987). The reason for this change is that most of the hydrogen in nanocrystalline nickel membranes is dissolved in the grain boundaries whose site energies have a Gaussian distribution (Mutschele 1987). Increasing hydrogen concentration will saturate low energy sites of the Gaussian statistical distribution of energy sites quickly and then eventually fill high-energy sites. Hydrogen diffusion will increase because the occupation of high-energy sites of the Gaussian distribution decreases the average activation energy (Arantes 1993). Hydrogen diffusion through grain boundaries plays a key role in hydrogen permeation through the nano-nickel membrane.

The decay transients for different charging currents have been shown in Fig. 5.10. One can see that hydrogen decays quickly for high charging currents at the beginning and approaches a similar constant value at the end of the experiments. This can be explained

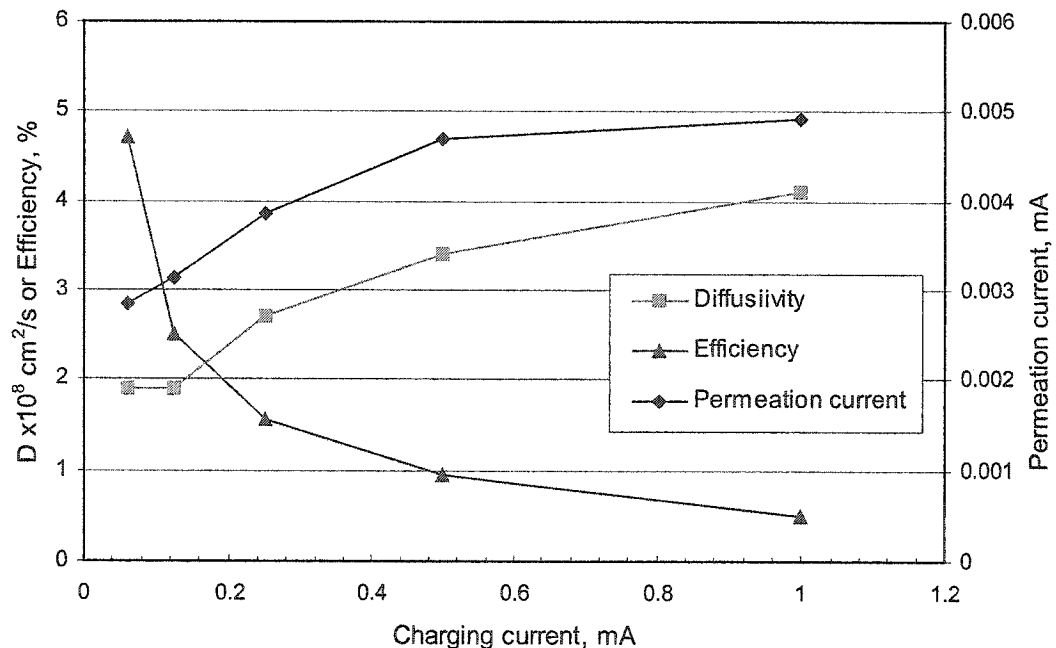


Fig. 5.9 Relationship between diffusivity, efficiency and permeation current for nano-nickel membranes with different charging currents

that if there are trapping sites in the sample, the trapping and diffusion of atoms are in dynamic equilibrium at a steady state. When charging is stopped, hydrogen continues to be extracted from the anodic side. As charging current increases, the number of hydrogen atoms in the nanocrystalline nickel membrane increase. The number of trapped atoms is proportional to the local concentration of atoms. A high charging current should trap more hydrogen atoms in the sample and should delay decay transients more than a low charging current because trapping sites release hydrogen slower than normal sites. But the results here show no delay, which means no trapping effect. It can be concluded that increasing charging currents only increases the total amount of hydrogen within the membrane.

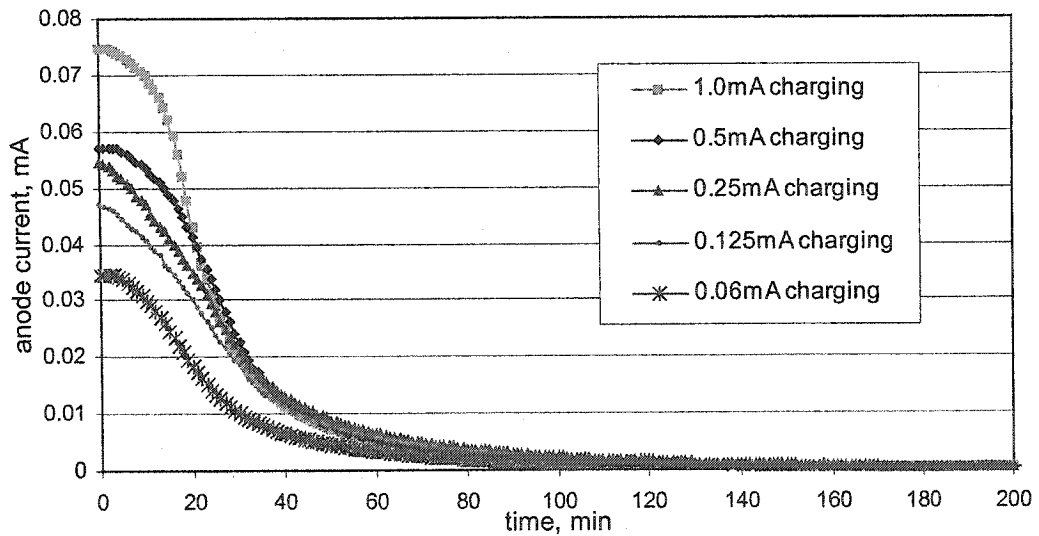


Fig. 5.10 Decay transients for nano-nickel membranes with different charging

5.3.2 Effects of grain size on hydrogen permeation in membranes

The diffusivity of hydrogen through the nickel membrane decreases significantly when comparing the non-annealed nanocrystalline membrane to the membrane annealed at 500 °C. The diffusivity does not change much for the membranes annealed at temperatures of 500 to 900 °C (Figure 5.11). The increase in the grain size affects the

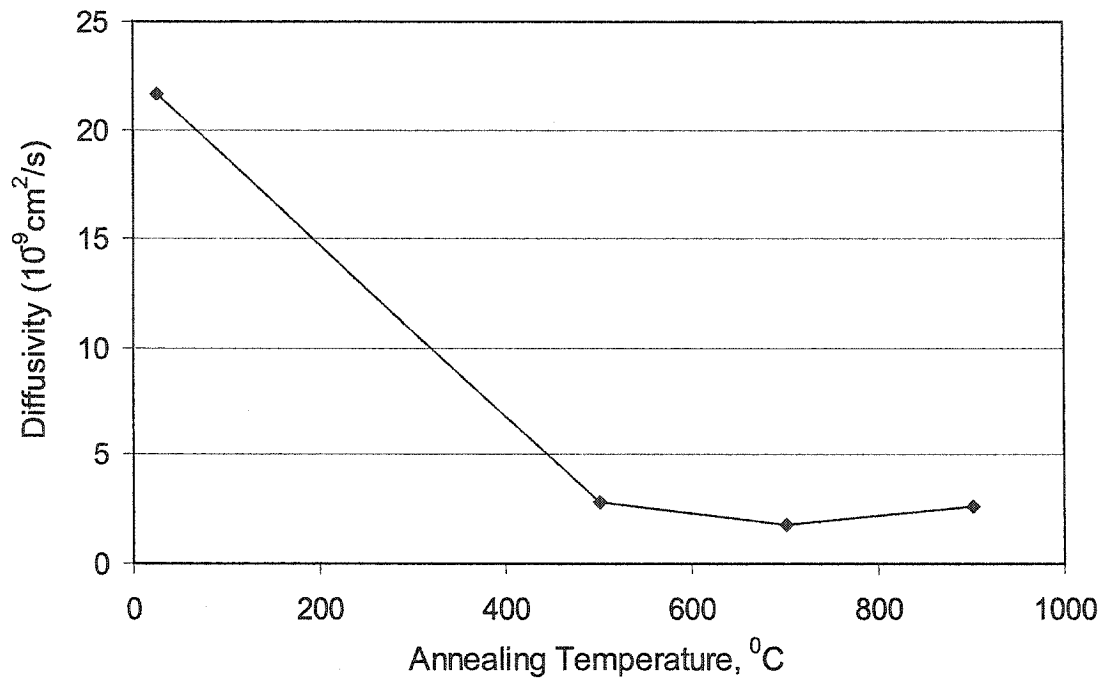


Fig. 5.11 Hydrogen diffusivity changes with annealing temperature

rate of permeation significantly, because the volume and type of grain boundaries are key factors in controlling hydrogen permeation. However, because the annealing process does not change the GBCD of nickel membranes (Fig. 5.6 and 5.7), this factor contributes minimally to changes in hydrogen diffusion through membranes. As the grain boundaries become a smaller portion of the sample after annealing at high temperature, the changes in volume of grain boundary does not contribute to changes of diffusivity even though there are large changes in the grain size after from annealing 800 °C to 900 °C. This is

why the difference between the diffusion coefficients of hydrogen is negligible for the specimens annealed between 800 °C and 900 °C.

5.3.3 Effects of grain boundary on hydrogen permeation in membranes

To examine the effects of grain boundaries on hydrogen diffusion, three microstructural types in metals have been chosen: single crystal, polycrystalline and nanocrystalline. The diffusivities of single crystal, polycrystalline and nanocrystalline nickel membranes have been shown in Fig. 5.12. From this figure, one can see that the single crystal nickel membrane has very small hydrogen diffusivity. The diffusivity of hydrogen in the nanocrystalline nickel membrane is nearly 40 times higher than that of a single crystal nickel membrane. The diffusivity of hydrogen increases six times from the single crystal membrane to the polycrystalline membrane, and increases 6 times again from the polycrystalline membrane to the nanocrystalline membrane. It should be mentioned here that these three membranes have been carefully chosen with the same

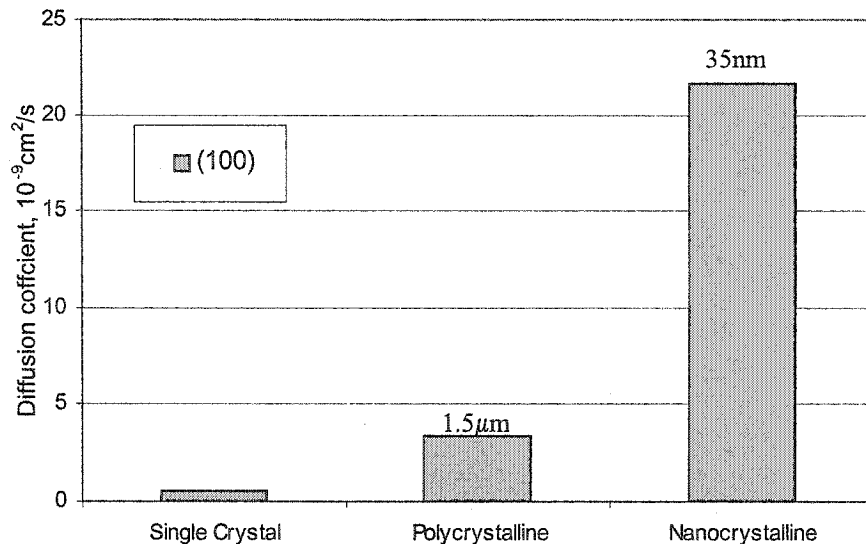


Fig. 5.12 Comparison of hydrogen diffusivities between single, poly and nano-nickel with the same orientation

(100) orientation in order to clarify the effect of grain boundaries only and to exclude the effect of different orientations.

The overall diffusion (lattice and grain boundary diffusion) in the polycrystalline membrane can be described by an effective diffusion coefficient, D_{eff} . The effective diffusion coefficient is given in equation 5.1 (Hart 1957).

$$D_{\text{eff}} = fD_{\text{GB}} + (1-f) D_{\text{G}} \quad (5.1)$$

Where f is the volume fraction of grain boundaries and D_{GB} is the diffusion coefficient along grain boundaries. D_{G} is the diffusion coefficient within the grains. For an equiaxed boundary network, we have

$$f = 3\delta / d \quad (5.2)$$

where d is the grain size and δ is the thickness of grain boundaries. Using measured diffusivity in the nanocrystalline nickel membrane marked as D_{eff} and the reference data D_{G} for single crystal nickel, D_{GB} can be calculated from formula (5.1). Combining equation (5.1) and (5.2) yields a series of D_{eff} which can be obtained by changing grain

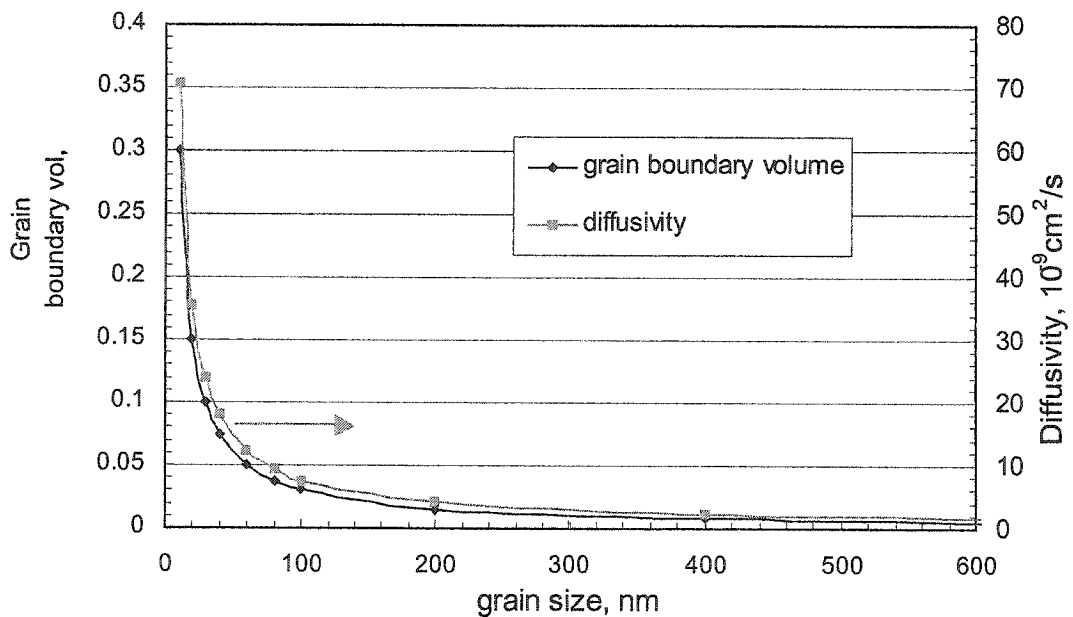


Fig. 5.13 Calculation of grain boundary volumes and diffusivities for different grain sizes in nickel membranes

size (Fig. 5.13). From Fig. 5.13, one can observe that diffusivities change dramatically when the grain size is increased, especially in the range of 10-100 nm. A comparison of the results of calculation (Fig. 5.13) with experimental data (Fig. 5.11), shows the same trends and also matches Marte's data (1997). This agreement proves that grain boundaries play a very important role in hydrogen diffusion through nickel membranes.

5.4 Summary

1. When nanocrystalline nickel membranes have been annealed between 200⁰C and 900⁰C, the microstructures of membranes change. After annealing in the range of 200⁰C to 400⁰C, diffraction peak broadening is reduced. After annealing between 500⁰C and 900⁰C, there is no grain size broadening observed and the grain size increases. After annealing at 900⁰C, some of the grains in the nickel membranes are larger than 70 μ m, which is the thickness of nickel membrane.
2. Annealing between 200⁰C and 900⁰C yields a gradual texture change in the nickel membrane from (100) fiber texture to (111) recrystallization texture. The differences in grain boundary character distribution (GBCD) of nickel membranes after annealing from 200⁰C to 900⁰C are not significant. A slight increase in the number of high angle (45⁰-65⁰) grain boundaries occurs, as the annealing temperature is increased. There is a small decrease in frequency of low (0⁰-15⁰) and middle angle (30⁰-45⁰) grain boundaries.
3. When the charging currents was increased, the permeation current for the nano-Ni membranes increased more rapidly, and then reached a high steady state permeation current. The permeation efficiency for the nano-nickel membranes decreased, but diffusion coefficients and permeation currents increased when the charging current

was increased. The diffusivity and permeation current increased slowly and approach a steady value for charging currents higher than 0.5 mA. The hydrogen diffusion coefficients of the nano-nickel membranes are dependent on hydrogen concentrations (charging currents).

4. The diffusion of hydrogen through the grain boundaries occurs more rapidly than in the grains of the metal membranes. The diffusivity of hydrogen is six times higher in polycrystalline membranes than in single crystal membranes, and increases again 6 times in nanocrystalline membranes. As the grain boundaries become a small portion of the sample after annealing at 800 °C and 900 °C, large changes in the grain size cannot even be noticed by measuring the rate of diffusion of hydrogen.

CHAPTER 6

EFFECTS OF TEXTURE ON HYDROGEN PERMEATION IN NICKEL MEMBRANES

6.1 Introduction

Transition metal-hydrogen systems have many applications. However, hydrogen ingress even at low concentrations can induce mechanical degradation of nickel and nickel alloys, and compromise the intended application of the alloy (Latanision 1983, Wipf 1997). An understanding of hydrogen adsorption-desorption characteristics on the hydrogen mobility in metals is needed to predict the impact of hydrogen on specific metal systems. Hydrogen dissociates on metal surfaces and dissolves atomically into the metal. As the hydrogen concentration increases in the bulk of metal, it interacts with metals and may form hydrides or can be trapped at grain boundaries or structural defects.

Electrodeposition is often used to manufacture nickel membranes in industry. Usually, nickel membranes produced by electrodeposition have different textures

depending on processing parameters. In general, the texture of electrodeposits is governed by three major factors which are related to the substrate used, electrochemical solution and processing parameters (Weil 1987, Delpancke 1993, Bergenstorf 1997). For thin electrodeposits, the substrate orientation affects the textures of deposits. However, this influence decreases with increasing deposit thickness. For thick deposits texture is only a function of electrolyte composition and current density.

The understanding of interactions between hydrogen and texture of metals is important to minimize the extent of damage because hydrogen embrittlement in metals is related to orientations of metals (Bath 1971). The diffusion of interstitial atoms in single crystals is not random. The experiment by Johnson (1964) indicated that diffusion along some directions is several orders faster than that along other directions. Because hydrogen permeation in single crystal metals is anisotropic (Ebisuzaki 1967, Brass 1990, Wu 1994, Brass 1996), textured polycrystalline metals may show different behaviors of hydrogen permeation for various textures. In this chapter, different textures in nickel membranes were obtained from electrodeposition or annealing. The crystal orientation has been examined.

6.2 Microstructure and texture of nickel membranes

6.2.1 Microstructure and texture of nickel deposits

The cross-section of optical microstructure of the nickel deposit is showed in Fig. 6.1. The grains have columnar shape and are oriented perpendicular to the substrate. Grain size of the deposit increases with coating thickness. A usual assessment of the microstructure allows us to reveal three zones. A very thin layer adjacent to the substrate

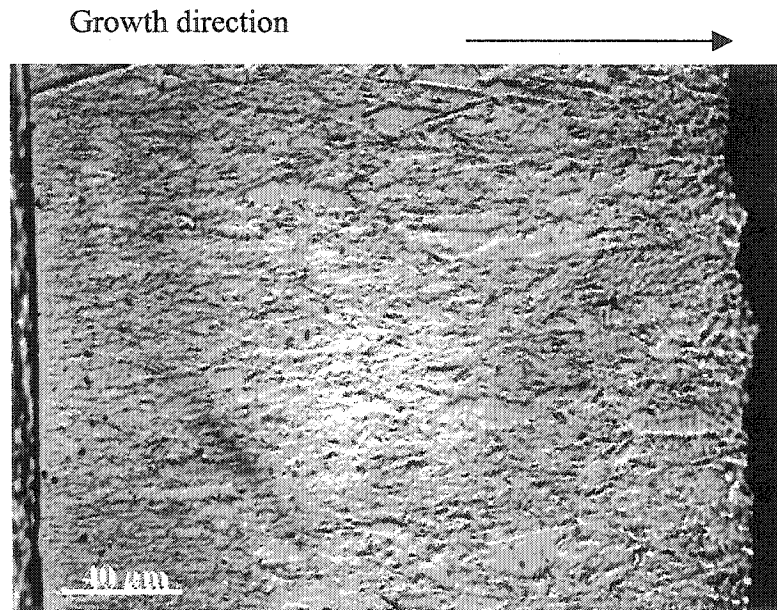
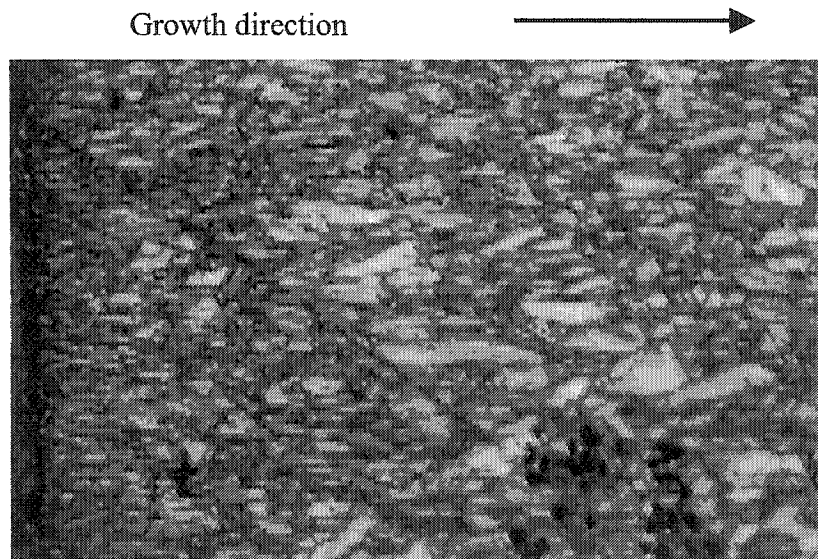


Fig. 6.1 Cross-section of microstructure of a nickel deposit

consists of equiaxed and fine grains. Then there is a transition zone, where the equiaxed grains change gradually into columnar shape grains. Although the increase in current



8.00 μm = 40 steps IQ 46.2...482.2

Fig. 6.2 Orientation imaging microscopy (OIM) microstructure of the cross-section in a nickel membrane

density reduced significantly the average grain size, the character of the microstructure

with three zones is observed for all deposition conditions. Orientation imaging microscopy (OIM) microstructure observation (Fig. 6.2) shows grains more clearly. There is a mixture of small grains and large grains in the nickel membrane. Although it is difficult to examine the microstructure through the whole cross-section by OIM, the average grain size of the nickel membrane is estimated at around $1.5 \mu\text{m}$ from the OIM image (Fig. 6.2). It is worthy to point out that nickel membranes have micron size grains.

As it was already mentioned in chapter 3, titanium plates were used as the substrates for nickel electrodeposition. The texture of the titanium substrate is presented as the orientation distribution function (ODF) in Fig. 6.3. The crystallographic texture of the substrate is composed of a $\{1210\}\langle 1010 \rangle$ component, which is typical of a cold

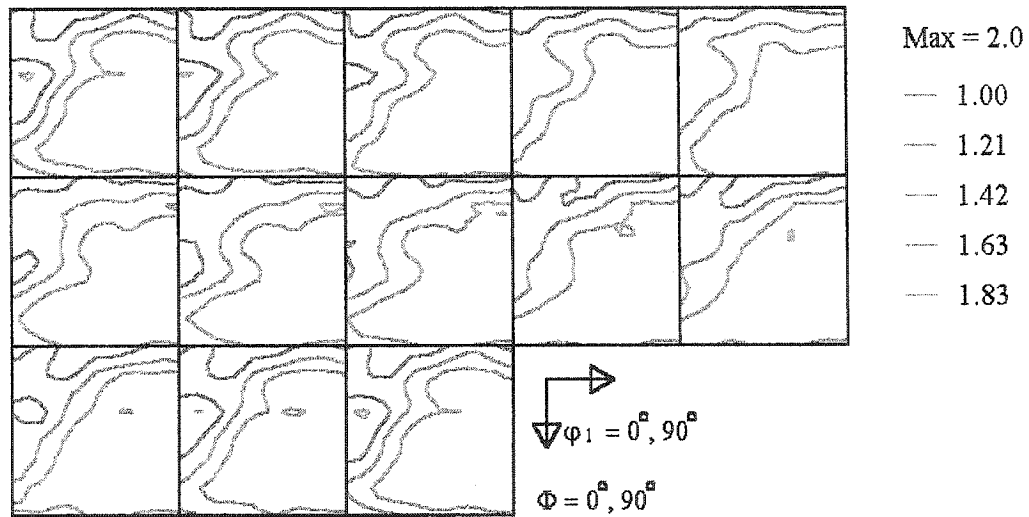


Fig. 6.3 Orientation distribution function (ODF) of a titanium substrate

rolled Ti plate (Inoue 1988). This knowledge is of importance to verify the influence of the substrate orientation on the deposit texture. A simple comparison of the typical texture of the nickel deposit (Fig. 6.4) and the Ti substrate shows that the substrate texture is totally different from the texture of the deposit. The deposit texture has a (100)

or (110) fiber texture depending on electrodeposition parameters, which shows that the substrate does not influence the deposit texture. This means that in this investigation the texture of the nickel deposit is influenced by the deposition parameters, but not by the substrate texture. A strong (100) fiber texture was clearly observed at low current densities. An analysis of the (100) fiber texture indicates that its strength increases when

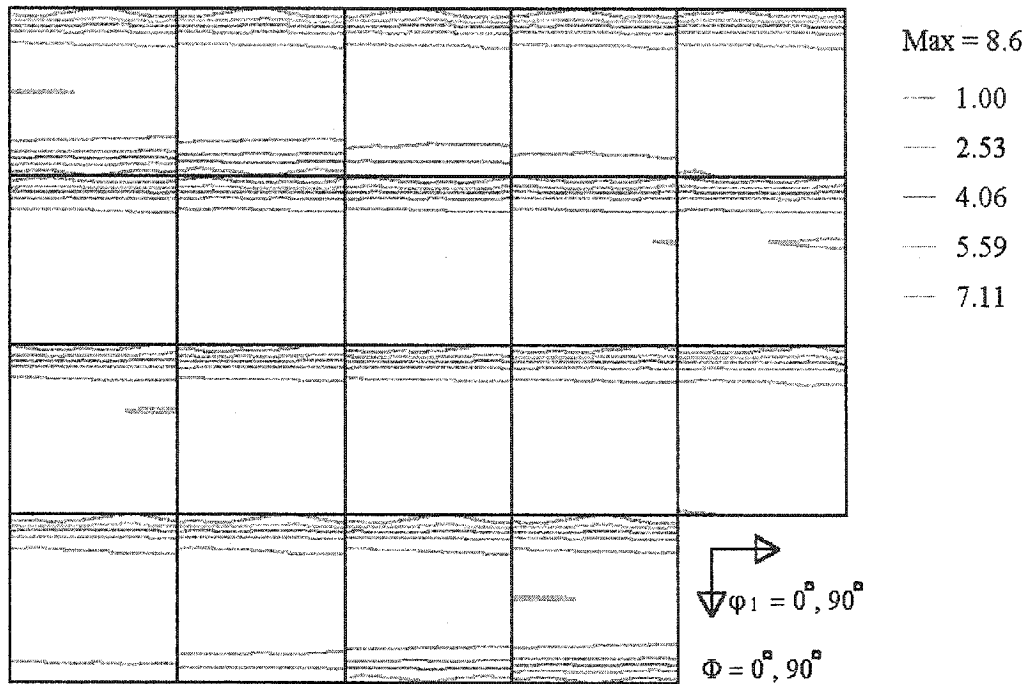


Fig. 6.4 Orientation distribution function (ODF) of a nickel deposit

the thickness of the deposits increases. This is especially true for low current density where an increase of the coating thickness from 25 to 190 μm caused texture strengthening by one order of magnitude (Fig 6.5). The influence of current density on the deposit texture is also shown in Fig. 6.6. There are two texture components, (100) and (110) fiber texture and their strength changes with the current density. At low current densities, the (100) texture is a main component. At high current densities, the (110) fiber

texture dominates. The rapid changes in intensities of (100) and (110) texture takes place between 30 and 50 A/dm².

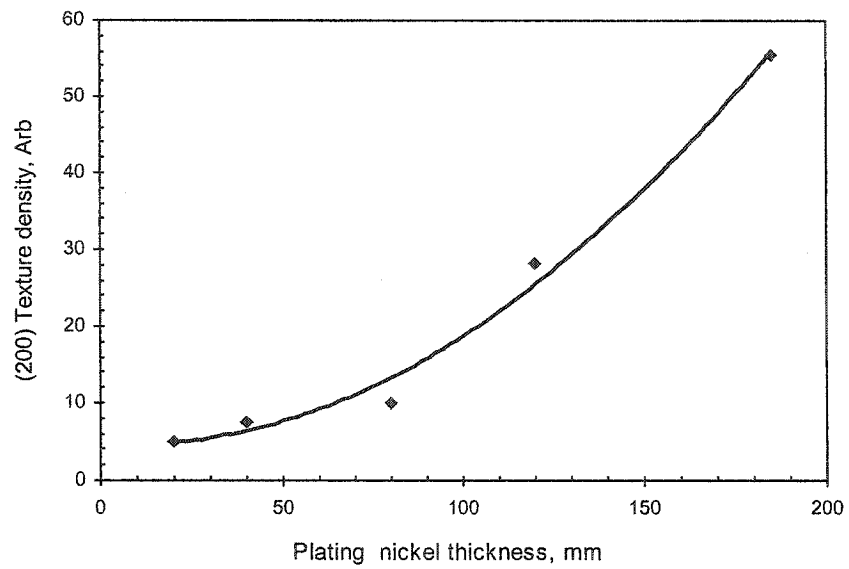


Fig. 6.5 The strength of (200) texture of electroplated nickel as a function of with the thickness

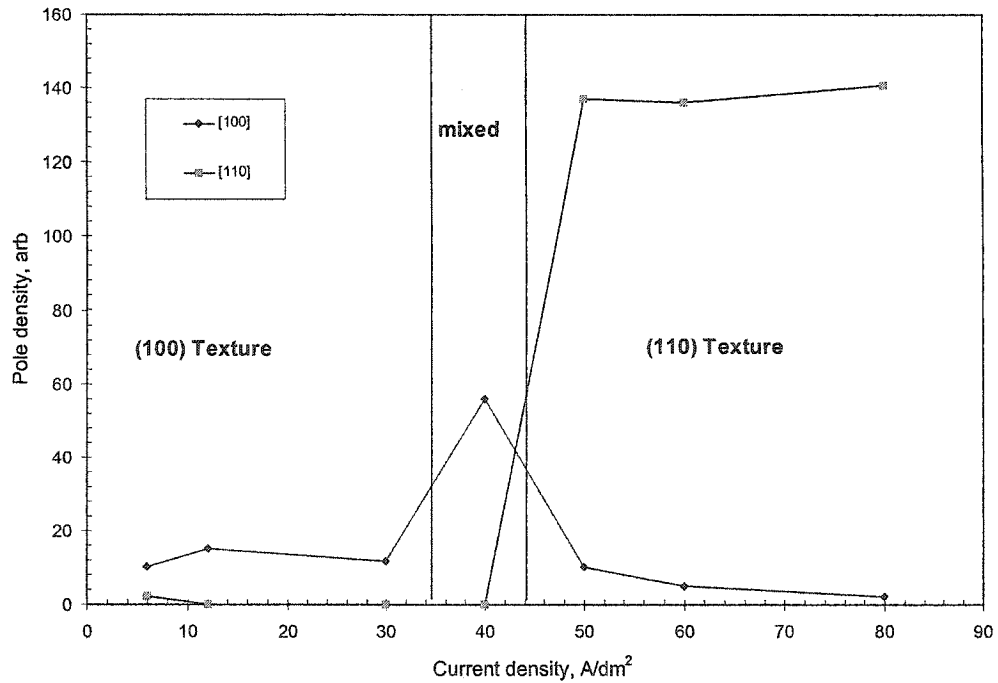


Fig. 6.6 Changes of strength of textures in electroplated nickel membranes with the current density

6.2.2 Analysis of texture formation in nickel deposits

During the electrodeposition, deposit crystals were formed by electrocrystallization. Direct electrocrystallization includes adsorption of atoms on the film surface, nucleation and growth processes. Nucleation and growth are mainly processes of electrocrystallization. The formation of textures is closely related to mechanisms of crystal nucleation and growth. Because the electrocrystallization of nickel is a strong inhibited process (Amblard et al 1979, 1984, Kollia et al 1991), the formation of texture in nickel deposit is also related to the inhibition. Therefore, it is important to consider the formation of the deposits with inhibition.

6.2.2.1 Nucleation of nickel electrodeposits

The nucleation stage of electrodeposits includes the solvated ion being transported to the cathode (substrate) by the electric field and then discharged into ad-atoms at the surface of the cathode. Finally small embryos formed on the substrate after adsorption atoms diffuse into low-energy sites. The formation of a new phase (small embryos) requires the system to be in a metastable state. This is achieved by perturbing the equilibrium state via the application of a potential field in a direct electrocrystallization. The nucleation rate (I) is expressed by equation 6.1 (Vermiyea 1963).

$$I = J \cdot B \cdot \exp[-\Delta G^* / RT] \quad (6.1)$$

Where ΔG^* is the critical free energy for nucleation, which is related to the surface free energies of the electrode-solution, electrode-film, and film-solution interfaces. B is a constant containing geometrical factors and J is the current density of the electrode.

6.2.2.2 Preferred Growth of Nickel Deposit

The deposit growth is often dependent on the process conditions, which follow nucleation. Selective crystal growth is controlled by the system energy. Different growth rates produce grains with different orientations, which is the way to develop textures.

According to the thermodynamics, any chemical reaction and structural transformation can occur when the system's energy is minimized. The system energy includes: surface energy, grain boundary energy and energy of the defect formation. For electrodeposition, the system energy is dominated by the surface energy when the depositing speed is low. So, the surface energy should be taken into account to understand the crystal growth. When the whole surface energy is at a minimum, the system has minimum energy. This means that the grain surfaces with minimal energy will grow preferentially.

The surface energy ratios for some low-index crystal planes, calculated by using a Lennard-Jones potential approach, are shown in table 6.1 (Tyson 1976, Li 1997). Clearly the (100) and (110) faces have lower surface energy values than the other faces, so nickel will easily form grains with (100) and (110) orientations. This explains why (100) and (110) textures are the most frequently observed. The strong (100) texture produced at low current densities results from a smaller inhibitor and adsorption (Li 1997), so the surface energy plays a more important role in electrocrystallization. The (100) texture is the result of the lowest surface energy face, which grows preferentially. But (100) texture will be transformed to (110) texture at high current densities because the inhibitor has a stronger effect. Between (100) texture and (110) texture regions, there is a mixed field of (100) and (110) texture.

Table 6.1 Surface energies of nickel metals

$\gamma^{(100)} / \gamma^{(100)}$	$\gamma^{(110)} / \gamma^{(100)}$	$\gamma^{(111)} / \gamma^{(100)}$	$\gamma^{(311)} / \gamma^{(100)}$	Reference
1.00	1.14	1.25	----	(Tyson 1976)
1.00	1.06	1.12	1.21	(Li 1997)

The linear rate of electrocrystallization, v , is directly related to the current density, j , according to equation 6.2 (Walsh and Herron 1991).

$$v = j V_m / nF \quad (6.2)$$

Where V_m is the molar volume and F is Faraday's constant. This relationship shows that high current density will lead to a higher rate of growth. When comparing equation (6.1) and (6.2), it can be found that nucleation and growth are in competition with each other. When the current density is high, the growth rate is very fast and occurs shortly after nucleation. The growth rate of the deposit is also different on different crystal phases. This means that the competition in crystal growth rate can produce texture.

6.3 Effects of texture on hydrogen permeation through membranes

6.3.1 Textures of deposited and annealed nickel membranes

The microstructure of nickel deposits was investigated at the cross-section of the samples. The microstructural cross-sections exhibit three zones. A very thin layer adjacent to the substrate consists of fine equiaxed grains. Then, a thin transitional layer is observed where a transition from equiaxed to columnar structure occurs. A large proportion of grains in the remaining part of the membrane have columnar shape grains that are orientated perpendicularly to the substrate for most electroplating conditions. The texture of the Ti substrate is presented as the orientation distribution functions (ODF) in Fig. 6.3. It exhibits $\{1210\}\langle 1010\rangle$ orientation, which is typical of cold rolled Ti plate (Inoue 1988). The texture of a typical Ni electrodeposit is presented in Fig. 6.4. Either (100) or (110) fiber textures can be obtained by changing the deposition conditions. At low current densities, the (100) fiber texture is a main component. While at high current

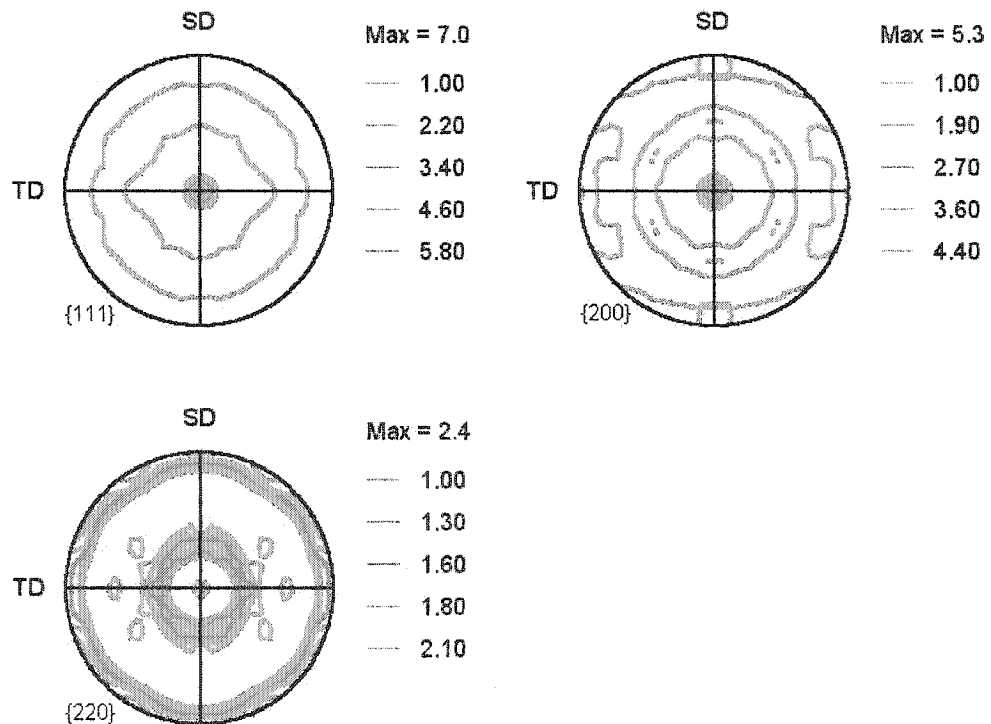


Fig. 6.7 The annealing texture of a nickel deposit

densities, the (110) fiber texture dominates. Furthermore, (111) texture can be induced by annealing deposits with (100) texture at 800°C for 1h (Fig. 6.7). Similar behavior has been reported recently (Czerwinski 1999).

6.3.2 Hydrogen permeation through differently textured membranes

Hydrogen permeation curves through nickel with different textures, including a sample without a dominant texture are shown in Figure 6.8. In all cases, the permeation current increases smoothly with increasing charging time to a maximum constant value. However, there are significant differences between the membranes having (001), (011) and (111) texture. Hydrogen transport through (111) textured nickel increases faster than

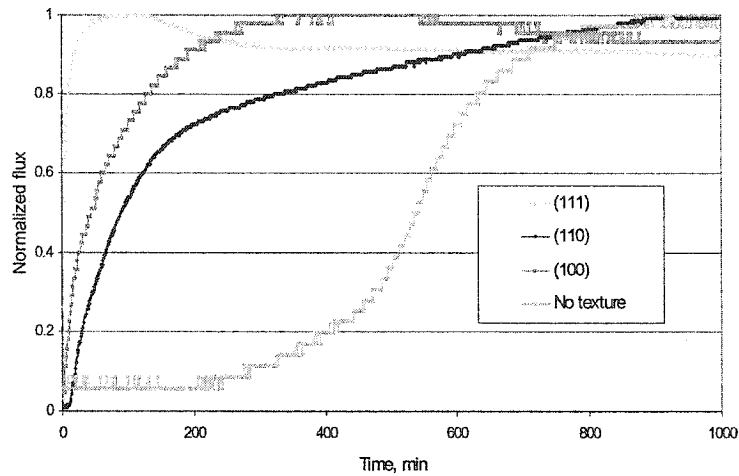


Fig. 6.8 Hydrogen permeation curves for nickel deposits with different textures

for any of the other textures. The time to attain steady state permeation is longest in (100) texture nickel. When compared to all other samples, the sample without a dominant texture has the slowest hydrogen permeation. Hydrogen permeation parameters for the nickel membranes with different textures have been listed in Table 6.2. Diffusion coefficients for (001) and (110) single crystal samples are provided for comparison.

Chapter 6: Effects of Texture on Hydrogen Permeation in Nickel Membranes

Diffusion coefficients increase as one moves from (001) to (011) and then (111) textured samples. The diffusion coefficient of a sample without a dominant texture is lower than the values measured for the samples with (001) texture, (110) and (111) textures. Diffusion coefficients of (001) and (011) texture membranes are higher than those of (001) and (011) single crystal membranes, but exhibit the same trend of changes as for (001) and (011) single crystal membranes. The sub-surface concentration (C_0) of hydrogen in the sample without a dominant texture is the highest (see the Table 6.2). The concentration of hydrogen in membranes having (111) and (011) texture is quite low. This means that there is only a small amount of hydrogen atoms in the membrane because hydrogen diffuses quickly through those samples.

Table 6.2 Hydrogen permeation data in nickel membrane with different textures

Membrane		D, *10 ⁻⁹ cm ² /s	C ₀ , *10 ⁻⁴ Mol/cm ³
Polycrystalline-Ni	Without texture	2.6	3.8
	(100) texture	3.4	1.8
	(110) texture	6.5	1.2
	(111) texture	8.5	1.3
Single Crystal-Ni	(100)	0.56 ^a	---
		0.51 ^b	---
	(110)	0.62 ^c	---

a. Ebisuzaki 1967 b. Brass 1990 c. Brass 1996

The whole process of hydrogen permeation through metal membranes normally consists of three steps: hydrogen absorption, diffusion and desorption. First, hydrogen absorbs on the membrane surface and dissolves into the metal. Then, atomic hydrogen

diffuses through the membrane, driven by the concentration gradient. Finally, hydrogen desorbs from the membrane. For the adsorption and desorption processes, kinetics are governed by absorption energies. The diffusion process is affected by microstructural factors, such as structure of interfaces and grain orientation. There are two reasons for observing different behaviors for hydrogen permeation in textured nickel samples.

The first reason is that hydrogen absorption energies are different for various crystal planes (Christmann 1979, Kresse 2000a, Kresse 2000b). From Kresse 2000a, we can get absorption energy data of the three low index planes for nickel: (001), (110) and (111). To show absorption energies for different orientations, the inverse pole figure has been used. Here, adsorption energies of certain orientations are calculated by the weighted average method from (001), (110) and (111) absorption energies. Absorption

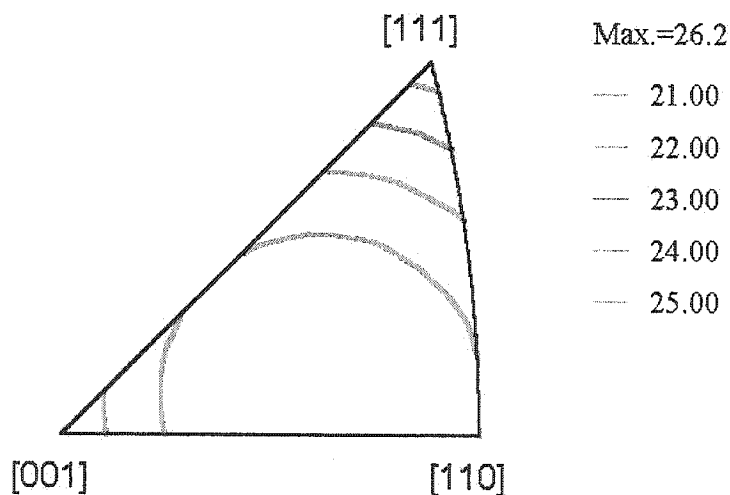


Fig. 6.9 Hydrogen absorption energies represented in the form of inverse pole figure for Ni crystal

energy distributions for certain orientations have been shown in Fig. 6.9. Figure 6.9 clearly shows how absorption energies change for different crystallographic planes. The absorption energy is the highest for the (001) plane and lowest for the (111) plane.

Hydrogen is expected to absorb more easily into (111) planes than on either (001) or (011) planes.

Secondly, the diffusivity also depends on orientation (Ebisuzaki 1967, Brass 1990, Brass 1996). A difference is noted for the two (001) and (110) single crystal orientations in nickel membranes. Polycrystalline membranes are composed of many single crystals (grains) with different orientations. If a polycrystalline membrane has texture, the grains have some preferred orientation of crystallographic planes with respect to the specimen surface. Hydrogen diffusion should be dependent on texture.

Hydrogen permeation relies on both absorption and diffusion. Hydrogen permeation in single crystal metals is anisotropic. For textured samples, certain orientations contribute more than others in terms of hydrogen permeation. That is why nickel membranes exhibit different behaviors of hydrogen permeation for (001), (011) and (111) texture. From absorption data for three crystal orientations and diffusivity differences of single crystal nickel, one can expect different diffusion coefficients for various textures in nickel membranes.

6.4 Summary

1. The average grain size in the electrodeposited nickel membranes is around 1.5 μm .

The nickel electrodeposits with thickness' of 200 μm have a columnar structure of grains and a fiber texture containing two major components: (100) and (110). Plating texture of nickel deposits is not dependent on the substrate texture. In the low current density range, the (100) fiber texture dominates. High current densities favor the growth of the strong (110) fiber texture. There is a texture transition region between 30 and 50A/dm². The formation of (100) and (110) texture in nickel can be explained

by the minimum surface energy concept and inhibited growth. Plating current density has a strong influence on the type and strength of texture. By controlling plating conditions, the texture of the deposits can be manipulated. After annealing at 800°C for 1h, the (100) texture of the deposit is transformed to the (111) texture.

2. Hydrogen permeation through nickel depends on the texture of the nickel membranes. Diffusion coefficients increase as one moves from (001) to (011) and (111) textured samples. The Diffusion coefficient of a sample without a dominant texture is lower than the values measured for the samples with (001), (110) and (111) textures. Diffusion coefficients of (001) and (011) polycrystalline membranes are higher than (001) and (011) single crystal membranes. However, in both cases the (011) diffusion coefficient is greater than that for the (001).
3. By using absorption energies of (001), (011) and (111) the three basic planes in nickel, adsorption energies for other orientations have been calculated using the weighted average method. Absorption energies for different orientations have been shown in the form of an inverse pole figure.
4. Different orientations of single crystal metals have different hydrogen absorption energies. For (001), (011) and (111) the three basic planes in fcc nickel, absorption energies decrease respectively. From the acknowledged absorption data for these three orientations and bulk diffusivity differences for single crystal nickel, one can expect that different diffusion coefficients exist for nickel membranes having different textures.

CHAPTER 7

ANALYSIS OF MICROSTRUCTURAL FACTORS ON HYDROGEN PERMEATION IN NICKEL, PALLADIUM AND $\text{Pd}_{77}\text{Ag}_{23}$ MEMBRANES

7.1 Introduction

Membranes made of nickel, palladium and Pd-Ag alloys have various applications (Nelson 1984, Tosti 2000). These metals and alloys can be easily formed into tubes that are used in hydrogen extraction units because they have a very good workability (Savitskii 1969, Lewis 1996, Tosti 2000). Palladium and Pd-Ag alloys also have good corrosion resistance in many aggressive media. Thermal treatment and mechanical deformation can be used to control texture and microstructure, which influence properties of nickel, palladium and palladium-silver alloys. Although the effect of mechanical deformation on solubility and diffusivity of palladium membranes has been already reported (Flanagan 1976, Bucur 1991), there are very few investigations on

the relationship between hydrogen permeation, and microstructure, grain boundary character distribution in metals and alloys.

Microstructural defects, grain boundary and texture affect hydrogen permeation in metals. Normally, the diffusion of hydrogen in metals proceeds more rapidly along grain boundaries than through the lattice. Grain boundary properties are dependent on the boundary structure. Prior studies have shown that cracking in grain boundaries charged with hydrogen is selective and dependent on grain misorientation. The low angle boundaries (LAB) are resistant to intergranular cracking (Bath 1971, Bernardini and Gas 1997). The role of grain boundary character distribution in hydrogen diffusion is also necessary to evaluate. A role of structural defects and texture on hydrogen permeation was discussed in previous chapters.

7.2 Grain misorientation in Pd and Pd-Ag membranes

Types of textures observed in palladium and Pd₇₇Ag₂₃ alloys are listed in Table

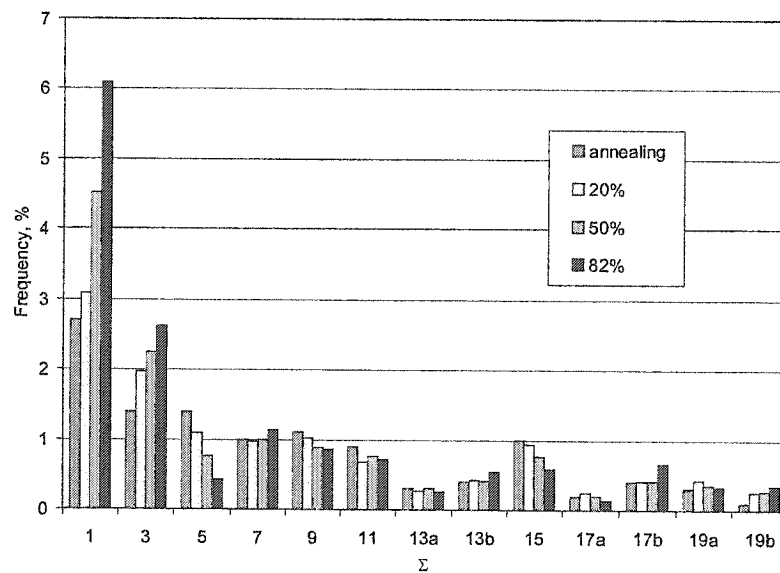


Fig. 7.1 Grain boundary character distribution in Pd

4.1. After large deformation, a strong rolling texture is developed. After annealing between 250⁰C and 850⁰C, the texture of palladium and Pd₇₇Ag₂₃ will change. The different textures will influence the grain boundary character distribution (GBCD). Those GBCDs in palladium and Pd₇₇Ag₂₃ were calculated using the method proposed by Morawiec et al (1993). The frequencies of CSL grain boundaries in palladium and Pd₇₇Ag₂₃ was calculated using 10⁴ pairs of orientations. Fig. 7.1 illustrates the frequency of CSL boundary distribution in palladium. From Fig. 7.1, we can notice that the annealed sample has a very low frequency of low angle (Σ 1) boundaries. When the amount of deformation increased, the frequency of low angle (Σ 1) boundaries significantly increased. Fig 7.2 illustrates the grain boundary distribution character in Pd₇₇Ag₂₃. The annealed samples have low frequency of low angle (Σ 1) grain boundaries compared to the deformed samples. When the annealing temperature increased from 250⁰C to 850⁰C, the frequency of low angle (Σ 1) boundaries decreased. After annealing for long time (20 hours) at 850⁰C, the frequency of low angle (Σ 1) boundaries strongly decreased.

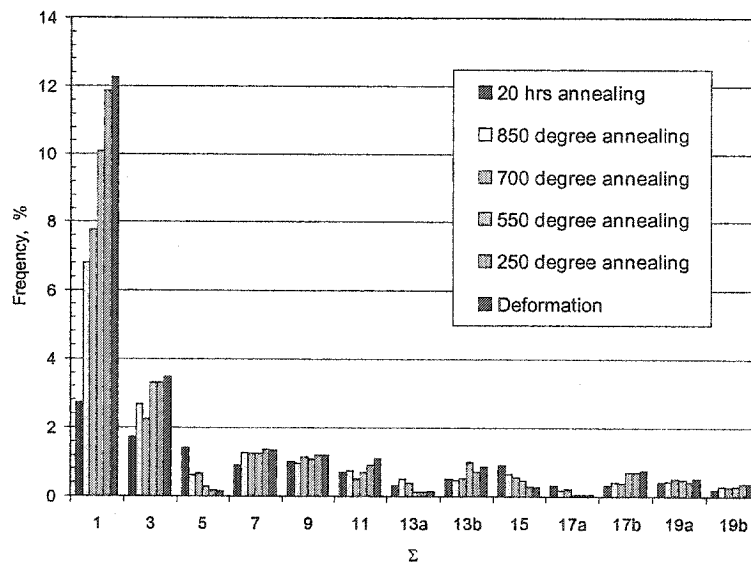
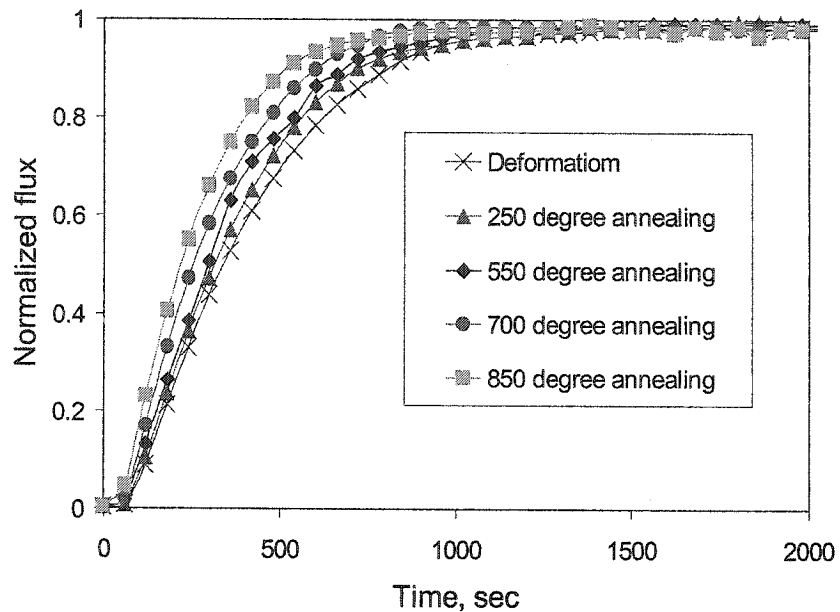


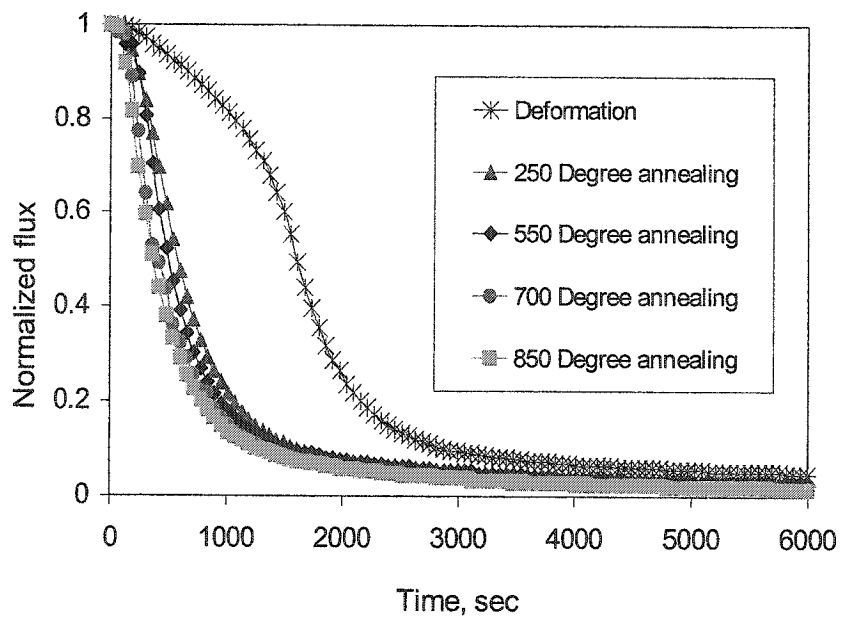
Fig. 7.2 Grain boundary distribution character in Pd₇₇Ag₂₃

7.3 Effects of misorientation on hydrogen permeation in membranes

The permeation curves obtained for the specimen after cold deformation and the annealed specimen of Pd₇₇Ag₂₃ alloys are shown in Fig. 7.3. The figure shows that the



(a)



(b)

Fig. 7.3 Hydrogen build-up (a) permeation and (b) decay for Pd₇₇Ag₂₃ membranes

permeation current density initially rises rapidly and then changes slowly. The permeation current of the deformed samples has increased more slowly than that of annealing samples with the same thickness. Pd₇₇Ag₂₃ after deformation and annealing exhibit different hydrogen absorption and desorption characteristics. The samples of annealed Palladium and Pd₇₇Ag₂₃ absorb and release hydrogen more rapidly than the deformed samples.

The permeation transients of cold rolled and annealed palladium (Fig. 4.8) are similar to that of palladium alloys. At low deformation (20%) however, some differences in hydrogen permeation characteristics are registered. When deformation increased to 50%, the permeation has been evidently delayed. This process continues up to 82% deformation, when the permeation is still delayed but changes are not so dramatic. The diffusion coefficients of palladium and Pd₇₇Ag₂₃ alloy decreased after deformation. On the other hand, the total amount of hydrogen accumulated in palladium and Pd₇₇Ag₂₃ alloy increased after deformation. This means that cold working increases the solubility

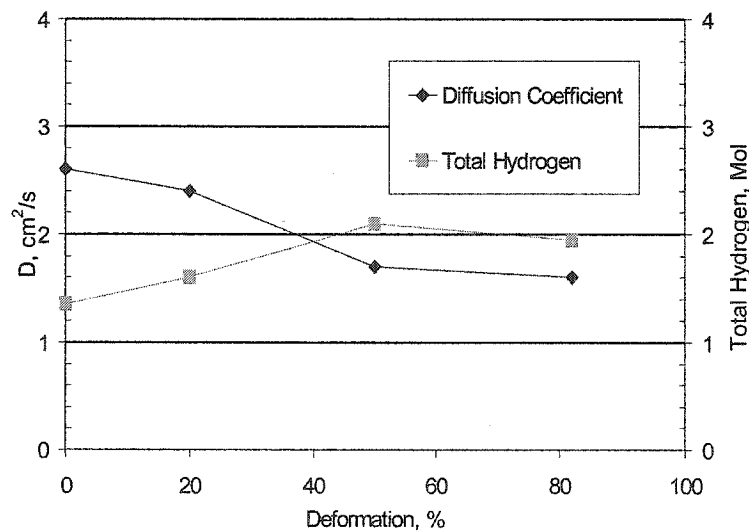


Fig. 7.4 Hydrogen diffusivity and total hydrogen accumulated in specimens as a function of deformed reductions in Pd

of hydrogen in palladium. The decay curves illustrating permeation for palladium and Pd₇₇Ag₂₃ membranes are shown in Fig. 4.12 and Fig. 4.13. For the annealed palladium, the hydrogen permeation current decreases faster than in the deformed palladium

The diffusion coefficients are $3.2 \times 10^{-7} \text{ cm}^2\text{s}^{-1}$ for the annealed Pd, and $2.9 \times 10^{-7} \text{ cm}^2\text{s}^{-1}$ for annealed Pd₇₇Ag₂₃ alloy. The annealing process increases the diffusion coefficients of Pd and Pd₇₇Ag₂₃ alloy. Those results are agreement with the previous reports (Early 1978, Bucur 1991). The hydrogen diffusion coefficients and the total hydrogen accumulated in specimens (equation 3.6) are presented in Fig. 7.4 and Fig. 7.5. The diffusion coefficients of palladium and Pd₇₇Ag₂₃ alloys decreased after deformation. On the other hand, the total amount of hydrogen in palladium and Pd₇₇Ag₂₃ alloys increased after deformation. This means that cold working increases the solubility of hydrogen in palladium due to the interaction of dissolved hydrogen atoms with the stress field created by the high density of dislocations (Flanagan 1976).

Hydrogen diffusion in polycrystalline materials is related to microstructure and

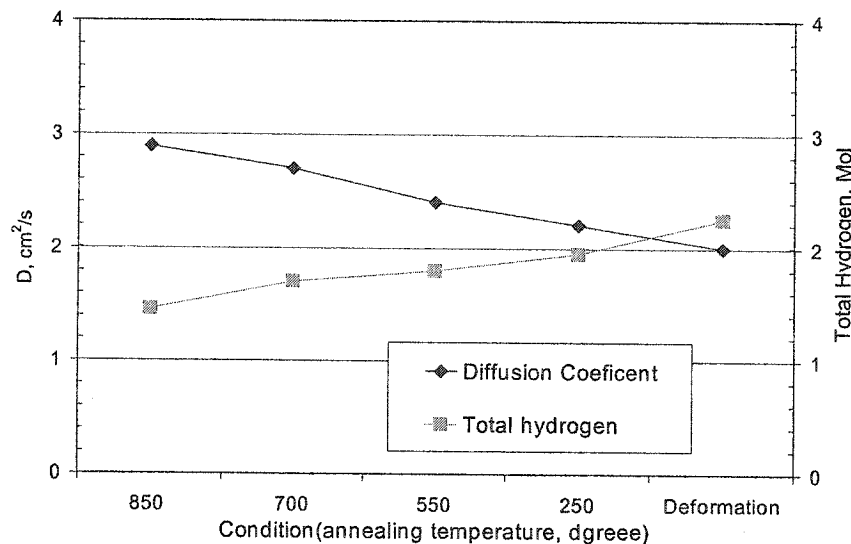


Fig. 7.5 Hydrogen diffusivity and total hydrogen accumulated in specimens as a function of annealing temperature for Pd₇₇Ag₂₃

orientation of grains. The structure of grain boundaries and type of texture affect the diffusion of hydrogen. When deformation increases, the textures in palladium samples strengthen and more defects are introduced. The defects will serve as trap sites for hydrogen. The hydrogen diffusivity depends on the trap density, trap strength, degree of saturation of traps, reversibility of trapping. Hydrogen more easily diffuse in the specimen annealed at 850 °C. In the deformed Pd₇₇Ag₂₃ the current decays more slowly.

Although rolling textures of palladium at 20%, 50%, 82% reduction have the same {112}<111> texture component with an additional {124}<112> component, the intensity of {112}<111> texture increased as reduction increased. For palladium, hydrogen absorption energies are different for the three low index planes: (001), (110) and (111) (Dong 1998). The absorption energy is the highest for the (001) plane and lowest for the (111) plane. Hydrogen is expected to absorb more easily into (111) planes than on either (001) or (011) planes. There is a 19.5° deviation angle between (112) and (111) plane. The stronger is the (112) texture, the more (112) planes are parallel to the surface of the sample and less (111) planes are parallel to the surface of the sample. Thus, absorption ability reduces. Maybe, this is one reason that highly deformed samples have low hydrogen diffusivities. Because the type of textures in deformed samples is unchanged, deformation defects make a significant contribution to low hydrogen diffusivities.

From previous studies of metals, the diffusivity is related to the orientation relationship (Gleiter and Chalmer 1972). The misorientation should have an influence on the diffusion. Comparing the different deformed samples, the frequency of low angle boundaries in deformed palladium is increased with increased reduction. Normally, the

high proportion of low angle grain boundaries will make diffusion more difficult. That is another possible reason for the delay of hydrogen diffusion.

After annealing, the texture became weak and the number of defects was reduced. The percentage of low angle grain boundaries was reduced as well, which may contribute to the acceleration of diffusion. It is worth pointing out that when the annealing temperature increased from 250 °C to 850 °C, the frequency of low angle boundaries decreased. That may be a reason that a high annealing temperature can improve hydrogen diffusion greatly. However, the low proportion of low angle boundaries is associated with the annealed structure, where there is no hydrogen trapping (chapter 4). So trapping and grain boundaries effects cannot be separated. The volume of grain boundaries is only a small portion of the volume of grains in a polycrystalline palladium membrane. The trapping should play a more important role in control of hydrogen permeation of deformed palladium membranes.

Another reason for the improvement of hydrogen permeation after annealing is the rearrangement and annihilation of dislocations, which are hydrogen trap sites. Annealing at low temperatures allows deformed samples to recover, and residual stresses are relaxed. All these microstructural changes facilitate the transport of hydrogen. The permeation current in Pd₇₇Ag₂₃ alloy annealed at 850°C increase faster than for the specimens that had experienced other thermal treatments. The high annealing temperature diminishes imperfections in the structure and facilitates the diffusion of hydrogen.

The defect traps, texture and character of grain misorientation distributions are three factors, which influence hydrogen diffusion in deformed palladium and Pd₇₇Ag₂₃ alloy. For deformed palladium and Pd₇₇Ag₂₃ alloy, defect trapping is a major factor for

hydrogen diffusion. The texture and misorientation distributions in deformed palladium and Pd₇₇Ag₂₃ alloy are also possible contributors to changes in hydrogen diffusion characteristics. The differences in hydrogen permeation for palladium and Pd₇₇Ag₂₃ result from different combination of factors mentioned above.

7.4 Microstructure in control of hydrogen diffusion through Nickel, Palladium and Pd₇₇Ag₂₃ Membranes

As it was mentioned before, there are several microstructural factors, which affect hydrogen permeation. According to our analysis, defects from plastic deformation, grain size, texture and misorientation are four main factors. Different processes may produce different microstructures, which may change some of these factors. A summary illustrating the influence of microstructure on hydrogen permeation is shown in table 7.1.

From the experimental data obtained for polycrystalline palladium (chapter 4), the density of dislocations in cold rolled palladium membranes is larger than 10^{12} cm⁻², but is less than 10^{10} cm⁻² in annealed palladium membranes. From the hydrogen trapping analysis of dislocations, it can be learned that deformation defects have a large influence on hydrogen permeation. When comparing to the annealed specimens, hydrogen diffusivity of cold rolling palladium is reduced roughly by a factor of two. This agrees with a previous work of polycrystalline nickel (Latanision 1983). It can be concluded from our analysis that the plastic deformation delays hydrogen permeation in polycrystalline metals. The diffusivity of hydrogen increases six times in polycrystalline membranes as compared to single crystal membranes, and increases six times again from polycrystalline membranes with 1.5 μm grain size to nanocrystalline membranes with 35 nm grain size (chapter 5). The density of dislocations in electrodeposited membranes is

around 10^{10}cm^{-2} (Merchant 1995). Obviously, the grain size in nanometer level has a stronger influence on hydrogen permeation than deformation defects in polycrystalline membranes. When comparing grain size and texture factors (Fig. 5.12 and Table 5.2), one can notice that the grain size plays more important role in hydrogen permeation than texture. This is also true for misorientation because texture and misorientation are related. This indicates that the grain size is a dominating factor for hydrogen permeation if the grains in the fcc sample are of nanometer size.

There is 2-3 times difference in diffusivity between various textures in nickel membranes (Table 5.2). It is estimated that a role of deformation defects and texture related factors in hydrogen permeation are nearly the same. So the structural defects and texture are both important for hydrogen permeation if the grains are of micrometer size.

When comparing texture and misorientation (chapter 5 and chapter 6), it is clear that texture has a more pronounced influence on hydrogen permeation than the misorientation between grains, unless there is a large difference in grain misorientation.

Table 7.1 Summary of microstructure influence on hydrogen permeation

	Nano-crystal	Poly-crystal	Single crystal
Grain size	very strong	strong	—
Defects	—	very strong	very strong
Texture (Orientation)	—	fair	strong
Misorientation	—	weak	—

In Table 7.1, there are four columns. The vertical direction presents effects of grain size, structural defects, texture and misorientation on hydrogen permeation in descending order. The horizontal direction shows effects of grain boundaries on hydrogen permeation in nano-crystal, poly-crystal and single-crystal membranes. Using Table 7.1, one can have a clear picture of how microstructural factors affect hydrogen permeation.

7.5 Summary

1. The rolling textures of palladium at 20%, 50%, 82% deformations exhibit mainly the $\{112\}\langle 111\rangle$ texture component with additional $\{124\}\langle 112\rangle$ component. The intensity of the cold-rolled texture $\{112\}\langle 111\rangle$ component of palladium increased gradually as deformation strain was increased. The proportion of low angle boundaries (LAB) has increased as reduction increases. Pd₇₇Ag₂₃ alloy has $\{011\}\langle 112\rangle$ and $\{123\}\langle 111\rangle$ textures. The annealing process reduces the amount of low angle boundaries in Palladium and Pd₇₇Ag₂₃ alloy.
2. Palladium and Pd₇₇Ag₂₃ after deformation and annealing exhibit different hydrogen permeation characteristics. When deformation increases, the textures in the palladium samples strengthen and more defects are introduced. The hydrogen permeation in deformed palladium and Pd₇₇Ag₂₃ is very slow. The high intensity of texture and high proportion of low angle grain boundaries also contributes to a delay in hydrogen diffusion. After annealing, textures of Palladium and Pd₇₇Ag₂₃ became weak, and the number of defects and low angle grain boundaries is reduced, which facilitate hydrogen diffusion.
3. Defect traps, texture and grain boundary misorientation distributions are the factors, which influence hydrogen diffusion in deformed palladium and Pd₇₇Ag₂₃ alloy.

Overall, the presence of defect traps is the major factor affecting the hydrogen diffusion in deformed palladium and the Pd₇₇Ag₂₃ alloy. Other factors play a less important role. The hydrogen permeation in palladium and Pd₇₇Ag₂₃ depends on combined influence of the factors mentioned above.

4. There are four major microstructural factors: deformation structural defects, grain size, texture and grain boundary character distribution, which influence hydrogen permeation in fcc metals. In polycrystalline metals with grain sizes in a micron level, the importance of these factors for hydrogen permeation is in that order: defects, texture and grain boundary character distribution. The grain size is the most important factor that controls hydrogen permeation in nanomaterials.

CHAPTER 8

HYDROGEN PERMEATION IN MULTI-LAYER MEMBRANES

8.1 Introduction

Layer-structure materials and multilayer membranes consist of several laminated layers. Actually, multilayer membranes are kinds of composite materials. Because each layer of a multilayer membrane has different characteristics of hydrogen permeation and is separated from another by an interface, these structural factors may have special influences on hydrogen permeation through the membrane. Analysis methods and mathematical descriptions of hydrogen permeation assume that samples are structurally homogeneous throughout their thickness. In chapter 4 to chapter 7, the effect of crystal defects, grain boundaries and texture of the membrane on hydrogen permeation was discussed. For composite metal membranes that are built from different kinds of single metal layers, previous models cannot be used directly. However, former methods can be extended assuming new boundary conditions. After analysis of hydrogen permeation

through each layer and interfaces of multilayer membranes, it is possible to find a way to explain hydrogen permeation process in multilayer membranes.

8.2 Hydrogen permeation through nano-nickel and poly-nickel membranes

8.2.1 Hydrogen charging for nano-nickel and poly-nickel membranes

The multilayer membrane system, which consists of a nano-Ni layer and a poly-Ni layer with a thin layer palladium in the both sides, is shown in Fig. 8.1. The thickness

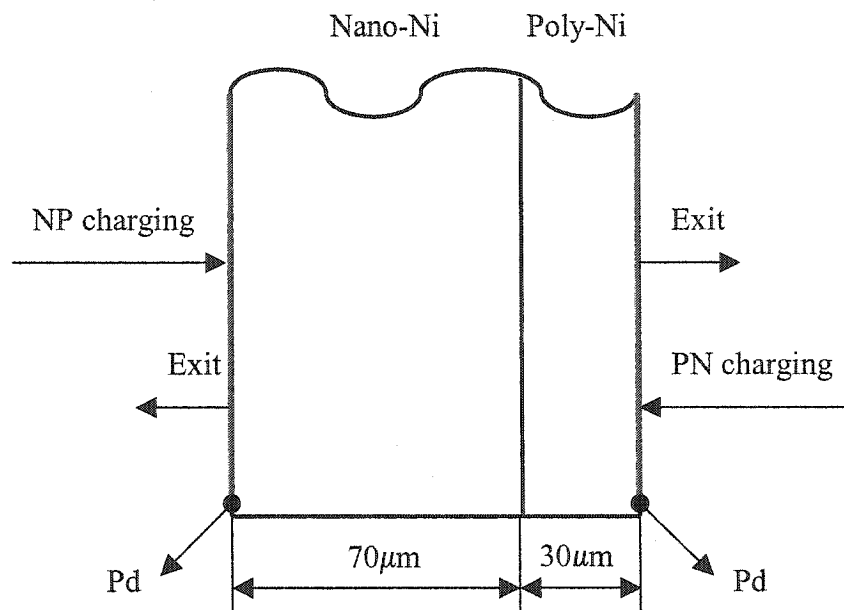


Fig. 8.1 Schematics of layer structures and hydrogen charging modes for a nano-poly-Ni multilayer membrane

for the nano-Ni layer is about $70\mu\text{m}$ and for the poly-Ni layer is around $30\mu\text{m}$. This membrane can be charged from two different directions. When hydrogen is charged from the nano-Ni layer side of a multilayer membrane, this charging will be called as NP charging and will represent the Nano-Poly-Ni direction of charging. In this case, hydrogen can permeate through the nano-Ni layer first and cross the interface between the nano-Ni layer and the poly-Ni layer, then through the poly-Ni layer in the membrane.

When hydrogen is charged from the poly-Ni layer side of a multilayer membrane, this charging will be called as PN charging and will represent the Poly-Nano-Ni direction of charging. In this case, hydrogen would permeate through the poly-Ni layer first and cross the interface between the poly-Ni layer and the nano-Ni layer.

8.2.2 Hydrogen permeation in the nano-nickel and poly-nickel bilayer membranes

The permeation curves obtained for the specimen of the poly-nano-Ni and nano-

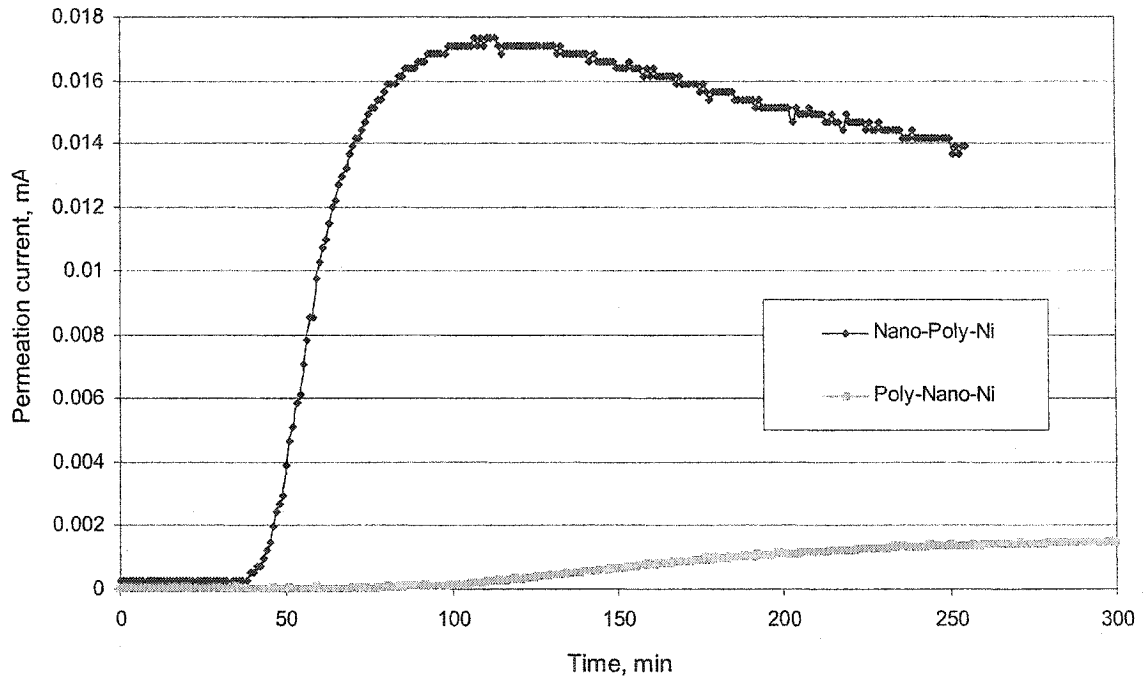


Fig. 8.2 Hydrogen permeation for poly-nano-Ni membranes in two directions

poly-Ni membranes are shown in Fig. 8.2, which combines permeation curves in two opposite charging directions. When hydrogen is charged from the nano-Ni side of a nano-Ni and poly-Ni composite membrane, the permeation current density initially rises rapidly and then changes slowly to the steady state. When hydrogen charged from the

poly-Ni side, the permeation current density gradually rises and takes a longer time to reach a steady state. Also the permeability of the NP charging is eight times higher than that of PN charging of the same membrane. The difference of hydrogen permeation in two directions is big even though the composite membrane is composed of the same thickness of the poly-Ni layer and of the nano-Ni layer. After charging from two opposite directions, using the same experimental conditions, there are more hydrogen atoms in NP charging than in PN charging (Fig. 8.2). Hydrogen decay curves (Fig. 8.3) show that the membrane by NP charging releases hydrogen faster than by PN charging. Because there is no charging during decaying, the driving force for hydrogen diffusion is the concentration gradient. This means that the hydrogen concentration is high in the interface between the nano-Ni layer and the poly-Ni layer.

Using the time-lag method for hydrogen permeation, hydrogen diffusion coefficient and permeability of a single layer and multilayer membranes have been measured and are listed in the Table 8.1. The diffusivity for a nano-poly-Ni membrane is two times higher than that of a poly-nano-Ni membrane. Comparing hydrogen permeation data of a single layer and multilayer membranes, one can find that diffusivity and permeability changes for the nano-poly-Ni and poly-nano-Ni membranes are similar to those for the nano-Ni membranes to the poly-Ni membranes. The diffusivity and permeability of a nano-poly-Ni membrane are smaller than those for a single nano-Ni membrane, but larger than those for the poly-Ni membranes. Obviously, a nano-Ni layer on a poly-Ni layer increases hydrogen permeation when compared to a single poly-Ni membrane. On the other hand, the nano-poly-Ni with an extra poly-layer nickel on the nano-Ni decreases hydrogen permeation when compared to a single nano-Ni membrane.

Using the method for hydrogen permeation in layered materials (Crank 1975), equation (8.1) can be obtained:

$$L_{1st}/D_{1st} + L_{2nd}/D_{2nd} = L_{composite}/D_{composite} \quad (8.1)$$

Where L_{1st} , L_{2nd} and $L_{composite}$ are the thickness of the 1st layer, the 2nd layer and the composite layer respectively. D_{1st} , D_{2nd} and $D_{composite}$ correspond to the diffusivity of 1st, 2nd and composite layer. Substituting the data from Table 8.1 for the nano-Ni as the 1st layer with 70 μm thickness and the poly-Ni as the 2nd layer with 30 μm thickness, one can obtain that the diffusivity of the nano-poly-Ni membrane equals 8.3 cm^2/s . The result agrees with our data very well (Table 8.1), when hydrogen has been charged from the nano-Ni side for a nano-poly-Ni membrane.

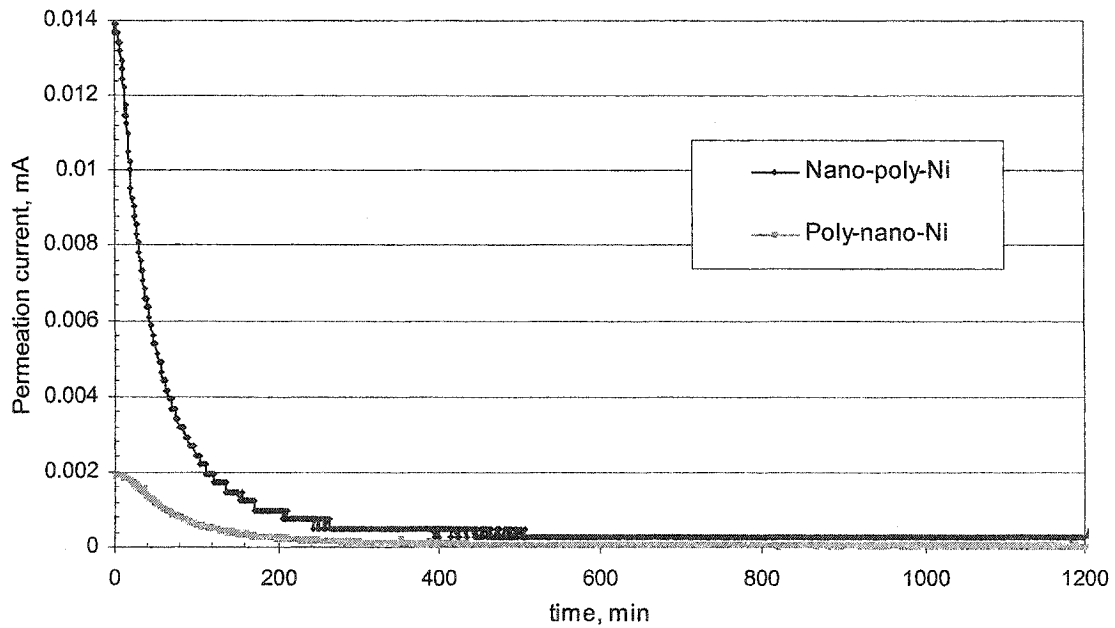


Fig. 8.3 Hydrogen decay for poly-nano-Ni membranes in two directions

Hydrogen transport from the poly-Ni layer to the nano-Ni layer is much lower than in the opposite direction (Table 8.1). There is a problem when using equation 8.1 to evaluate hydrogen permeation in a poly-nano-Ni membrane, because the equation does

not take into account the charging direction. The reason is that equation 8.1 is based on the assumption that the total difference of hydrogen concentration equals to the sum of the hydrogen concentration differences, and that fluxes are equal for all layers at a steady state. In our cases, this is not true because permeability of a nano-Ni membrane is higher than that of a poly-Ni membrane. For a nano-poly-Ni membrane, the nano-Ni layer absorbs hydrogen easily and has enough hydrogen supply to sustain transport when the nano-Ni layer is the first layer of the composite membrane. There is enough hydrogen in the interface between the nano-Ni layer and the poly-Ni layer so that it is an easy path for hydrogen compared to the interface between electrolyte and the poly-Ni layer. For a poly-nano-Ni membrane, the poly-Ni layer cannot absorb as many hydrogen atoms as the nano-Ni has, even though there is enough hydrogen supply to undergo transport when the poly-Ni layer is the first layer of the composite membrane. There is less hydrogen available in the interface between the poly-Ni layer and the nano-Ni layer, which limits hydrogen flux through the nano-Ni layer. Because diffusivity of nano-materials is dependent on hydrogen concentration (Mutschele 1987), hydrogen permeation through the nano-Ni layer slows down when hydrogen supply to the surface decreases. Our data has shown that diffusion coefficients of the nano-Ni membranes increase as charging currents increase. This is a key point for understanding as to why diffusion behavior in a nano-poly-Ni membrane is different from the normal single layer nickel membranes. Overall hydrogen permeation in a nano-poly-Ni membrane is much higher than that of a poly-nano-Ni membrane.

To prove an additional support for above analysis of hydrogen permeation in bilayer membranes, a nano-poly-Ni sample has been charged from two sides after

annealing at 800⁰C. The result shows that diffusion coefficients are nearly the same for both charging directions, and are equal to a single layer polycrystalline nickel membrane. This means that composites with two poly-Ni layers show no difference in hydrogen permeation behavior when compared to a single poly-Ni membrane. This experiment does provide evidence, that the nano-Ni layer in composite membranes plays a very important role in hydrogen permeation anisotropy.

Table 8.1 Hydrogen permeation data in single layer and multilayer membranes

Membrane	Grain size	Structure	D *10 ⁻⁹ cm ² /s	Permeability, J _∞ *L *10 ⁻⁹ mol H/cm s
Nano-Ni	40 nm	One layer	21.6	2.1
Poly-Ni	1.5μm	One layer	3.4	0.4
Nano-Poly-Ni	---	Two layers	8.1	35.2
Poly-Nano-Ni	---	Two layers	3.9	3.7

8.3 Simulation of hydrogen permeation in multilayer membranes

8.3.1 Multilayer diffusion mechanism and concentration profile

When a multilayer membrane has been charged with hydrogen, hydrogen will be absorbed on the first layer of the membrane and diffuses through it in the same way that hydrogen diffuses through a single layer membrane. When hydrogen reaches the interface between the first layer and the second layer, hydrogen will absorb on the second layer of the membrane and diffuse through the second layer, then will be desorbed on the exit side. If an interface between metals is well connected and does not have voids, such

interface between components of membranes will easily absorb and transport hydrogen. Hydrogen concentrations on both sides of the interface are only dependent on the solubility for each layer in the bilayer metal membranes.

The schematic diagrams of hydrogen concentration for NP charging and PN charging in a poly-Ni and nano-Ni composite membrane are shown in Fig. 8.4 and 8.5. In both cases, hydrogen concentration at the exit side is zero, which is the normal case for hydrogen permeation. The hydrogen concentrations in both the entry and exit sides of the

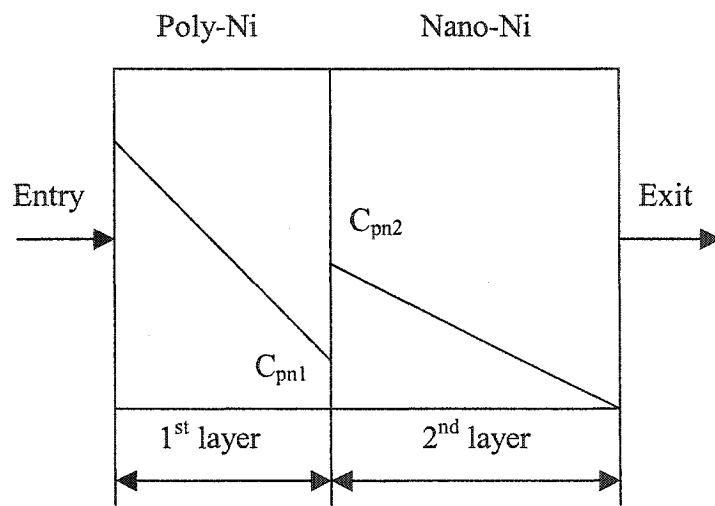


Fig. 8.4 Hydrogen concentration profile for PN charging in a poly-Ni and nano-Ni composite membrane

poly-nano-Ni membrane are the same as that of the nano-poly-Ni membrane. However, there is a difference in the hydrogen concentration at the interface between the poly-Ni layer and the nano-Ni layer when compared NP charging with PN charging in a poly-Ni and nano-Ni composite membrane. The hydrogen concentration (C_{pn1}) of the poly-Ni side at the interface between the poly-Ni and nano-Ni layers for PN charging is lower than hydrogen concentration (C_{pn2}) of the nano-Ni side at the interface. The hydrogen concentration (C_{np1}) of the nano-Ni side at the interface between the nano-Ni and poly-Ni

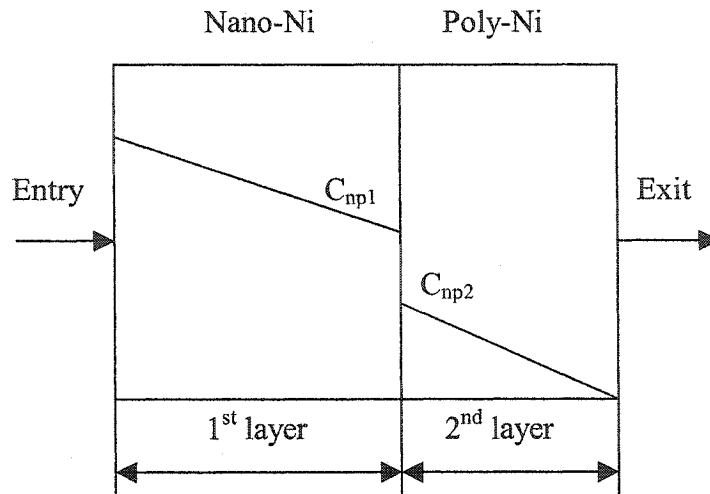


Fig. 8.5 Hydrogen concentration profile for NP charging in a poly-Ni and nano-Ni composite membrane

layers for NP charging (nano-poly-Ni) is higher than hydrogen concentration (C_{np2}) of the poly-Ni side at the interface. This is because in the case of the nano-poly membrane, the 1st layer is the nano-layer, which has relatively higher diffusivity and solubility due to the higher volume of grain boundaries. For PN charging in a poly-nano-Ni membrane, the 1st layer is a poly-Ni layer, which has relatively low diffusivity and solubility and as a result a lower hydrogen concentration is present at the interface. According to Henry's law, Henry's constant, K , can be defined from the ratio of hydrogen concentrations on both sides of the interface. K_{np} refers to the ratio of the hydrogen concentration of the nano-Ni side to that of the poly-Ni side just near the nano-Ni layer and poly-Ni layer interface. K_{pn} refers to the ratio of the hydrogen concentration of the poly-Ni side to that of the nano-Ni side just near the poly-Ni layer and nano-Ni layer interface. Those definitions can be written as equations (8.2) and (8.3)

$$K_{np} = C_{np1} / C_{np2} \quad (8.2)$$

$$K_{pn} = C_{pn1} / C_{pn2} \quad (8.3)$$

Of course, this definition assumes that the ratio of the concentrations across the interface is always equal to the ratio of the corresponding equilibrium solubilities. From Fig. 8.4 and 8.5, one can see that the K_{np} is larger than 1 and the K_{pn} is smaller than 1.

For the 2nd layer membrane, the driving force for diffusion is the hydrogen gradient across the membrane. For PN charging in the poly-nano-Ni membrane, hydrogen concentration of the poly-Ni side at the interface between the poly-Ni layer and the nano-Ni layer is lower than that of the nano-Ni side at the interface. It means that the poly-Ni side cannot provide enough hydrogen atoms for the nano-Ni side to diffuse. Thus, hydrogen in the nano-Ni as the 2nd layer will diffuse slowly because of low concentration of hydrogen at the interface in the nano-Ni layer. Another reason is that hydrogen atoms from the poly-Ni side can be sucked into the nano-Ni layer until the nano-Ni layer reaches its solubility limit because the nano-Ni has a higher solubility. It takes time to saturate the nano-Ni layer in the composite membrane. Therefore, diffusion process for the whole composite membrane has been slowed down.

For NP charging in the poly-nano-Ni membrane, the nano-Ni layer is in the charging side with plenty hydrogen supply. Hydrogen concentration in the charging side is high. Because the nano-Ni with high hydrogen concentration transports hydrogen fast, hydrogen in the nano-Ni layer diffuses faster for NP charging than for PN charging in the poly-nano-Ni membrane. Hydrogen concentration of the nano-Ni side at the interface between the nano-Ni layer and the poly-Ni layer is higher than that of the poly-Ni side at the interface. It implies that the nano-Ni side provides enough hydrogen atoms for the poly-Ni side to diffuse. Hydrogen in the poly-Ni layer of the poly-nano-Ni membrane with a NP charging condition can still diffuse like in a single layer Ni membrane with

hydrogen charging. The combination of fast diffusion in the nano-Ni layer and normal diffusion in the poly-Ni layer of the poly-nano-Ni membrane makes the NP charging condition better than the PN charging condition in terms of hydrogen diffusivity. It is the hydrogen concentration at the interface between the nano-Ni layer and the poly-Ni layer that plays an important role in anisotropic hydrogen diffusion for two-direction charging.

8.3.2 Description of the simulation model

From Fig. 8.4 and 8.5, it can be seen that hydrogen has been charged in the direction perpendicular to the membrane plane, which is the case in our experiments. The cross-section of the metal membrane sample is described by a two-dimensional network of sites. One site represents a small piece of material, which is defined as a group of atoms. In this model, a multilayer membrane has two components, which are the nano-Ni layer and the poly-Ni layer. In order to simplify the problem, both the nano-Ni layer and the poly-Ni layer are treated as a homogenous diffusion matrix in the model. The overall diffusivity in the nano-layer is considered higher than that in the poly-layer because of the differences in the grain boundary volume. In this sense, the grain boundary effect is implemented in a simple way. Due to this assumption, the details of the microstructures and grain boundary character distribution in the nano-layer and the poly-layer are not included directly in the simulation. The membrane specimens with larger than 1:10 ratio of specimen thickness to diameter of charging area have been recommended for a reliable hydrogen permeation measurement (Hutchings 1993). Samples used in experiments have 1:40 to 1:200 ratios. This means that hydrogen diffusion mainly occurs through the membrane along the direction perpendicular to the membrane because the thickness is relatively small comparing with the diameter of the charging area. To implement this

experimental condition in the computer model, the computer sample is defined as 100 sites in length and 10 sites in width. The computer sample has the periodic boundary condition along the sample length, therefore, the length of the computer sample can be considered as infinite. This ensures that the effect of the sample edge on the hydrogen permeation is eliminated. The random walk method has been used to simulate hydrogen diffusion (Shewmon 1989). Normalized thickness of the nano-Ni layer or the poly-Ni layer is used to represent the results in a more general form. The thickness ratio ($L_{\text{nano}}/L_{\text{comp}}$ or $L_{\text{poly}}/L_{\text{comp}}$) between the polycrystalline layer and the nanocrystalline layer was normalized to the whole thickness. The interface between the two layers in a bilayer membrane is considered free from defects.

When a bilayer membrane has been charged, there are two possible scenarios for hydrogen permeation, depending on the charging direction. The nano layer in a bilayer membrane is the first layer for the first case, NP mode. The polycrystalline layer in a bilayer membrane is the first layer for the second case, PN mode.

In the NP mode, hydrogen is charged from the nano-Ni side of the nano-poly-Ni membrane, the transport of hydrogen in nano-Ni layer is fast like in a single nano-Ni membrane until hydrogen reaches the interface between the nano-Ni layer and the poly-Ni layer. Hydrogen concentration at the nano-Ni side of the interface between the nano-Ni layer and the poly-Ni layer is higher than that at the poly-Ni side of the interface. Hydrogen concentration at the interface between the nano-Ni and the poly-Ni layers is high, which supplies enough hydrogen atoms into the poly-Ni layer for further permeation.

In the PN mode, hydrogen is charged from the poly-Ni side of the poly-nano-Ni membrane, hydrogen in the poly-Ni layer is transported like in a single poly-Ni membrane. Hydrogen concentration at the poly-Ni side of the interface between the poly-Ni layer and the nano-Ni layer is low, and therefore supply of hydrogen atoms into the nano-Ni layer is limited. Hydrogen atoms go at first slowly through the nano-Ni layer because hydrogen atoms from the poly-Ni side can be sunk into the nano-Ni until the nano-Ni reaches its solubility limit. Because the nano-Ni has a high solubility, it takes time to saturate the nano-Ni.

It was the hydrogen concentration difference in nano-Ni layer that resulted in the difference in hydrogen diffusivities in the two nano-layers. Finally, this leads to the significant difference in the overall hydrogen permeation in a bilayer membrane for two-direction charging. This phenomenon is simulated qualitatively, when a constant hydrogen concentration is kept at the entrance side of the membrane.

8.3.3 Simulation process of hydrogen permeation in bilayer membranes

In the section 8.3.1 and 8.3.2, the modeling scenario has been described and the hydrogen concentration profile has been produced. Now, it is necessary to introduce more details to run this simulation. Four conditions should be clarified to build up the simulation model for hydrogen permeation in bilayer membranes.

1. Before charging hydrogen, there is almost no hydrogen in metal membranes. This is a normal case because residual hydrogen in the membrane has been extracted by holding a constant anodic potential at the exit side for long time. The extraction of hydrogen is a standard procedure for electrochemical permeation. The boundary conditions for hydrogen permeation are constant pressure on the entry side, which

keep enough hydrogen on the entry surface of the membrane. Even through a nickel membrane has been charged galvanostatically, it still can hold enough hydrogen on the entry side because there is less than 100% of the charged hydrogen appearing on the exit side (Archer 1984, Harris 1991). Actually, a large part of hydrogen charged at the nickel membranes formed molecular hydrogen, which dissolved into the aqueous solution and bubbled away, and only a small fraction was transported across the membrane. Therefore, it is easy to establish a constant hydrogen concentration in the entrance side. The zero concentration at the exit side is always true for permeation since the exit side is held potentiostatically at a sufficient potential to ensure that all hydrogen is instantly oxidized (Atrens 1980, Boes 1976, Tsubakino 2000, Yen 1999).

2. As mentioned before (section 5.3), the difference in percentage of grain boundaries volumes between polycrystalline nickel and nanocrystalline nickel is big. In order to simplify the calculation, the overall diffusivity in the nano-layer is considered higher than that in the poly-layer. This means that the grain boundary effect is integrated into the overall diffusivities of the membranes. Due to this simplification, the details in the microstructures and grain boundary character distribution in the nano-layer and the poly-layer are eliminated. Both the nano-layer and the poly-layer are treated as a homogenous diffusion matrix in the model. Here only the lattice diffusion is being used for polycrystalline nickel. A unique and complex diffusivity for the nanocrystalline nickel represents a combination of lattice diffusion, triple junction diffusion and grain boundary diffusion, which is expressed as a diffusion coefficient of a nano-Ni membrane. The main attention focuses on anisotropic behaviors of bilayer membranes.

3. The random walk process has been used to simulate hydrogen diffusion through composite membranes. The atoms jump into different directions at even probability in two dimensions. The flux is calculated by averaging the number of passing hydrogen atoms in exit side at a given time of simulation time units when a certain amount of hydrogen has been charged in entry side. By plotting flux vs. simulation time, a permeation curve has been obtained.
4. The simulation runs 20 loops at its plateau region for a given hydrogen permeation flux to make sure that permeation curve really reaches steady state. Then the simulation stops hydrogen charging from entry side and starts the desorption process immediately, in which hydrogen is removed from the specimen. When a permeation flux reduces to 1% of the steady state value, the whole simulation process stops. 1% is arbitrarily selected in this qualitative simulation.

8.3.4 Simulation steps of hydrogen permeation in bilayer membranes

The diagram illustrating the whole process of simulation is shown in Fig.8.6. Accordingly, there are seven steps to simulate the process of diffusion.

- (1) Input parameters: this includes Filename, thickness of the nano-Ni layer as well as the poly-Ni layer, and diffusion coefficients of the nano-Ni layer as well as the poly-Ni layer.
- (2) Produce hydrogen concentration file across the computer sample with two dimensions.
- (3) Simulate hydrogen diffusion with the interface between two layers: this traces hydrogen atom diffusion in bilayer membranes.

(4) Flux calculation: this counts flux of hydrogen passing through the membrane and compares the flux with previous one.

(5) Stop charging hydrogen and start desorption process: this process stops hydrogen supply and starts decay process when a constant flux plateau has been reached for 20 times.

(6) Stop desorption process: this procedure stops desorption and starts saving files when the flux reaches 1% of steady state flux value.

(7) Save a file and end the processing: this procedure will save calculation results in a file named by the user and end the whole program.

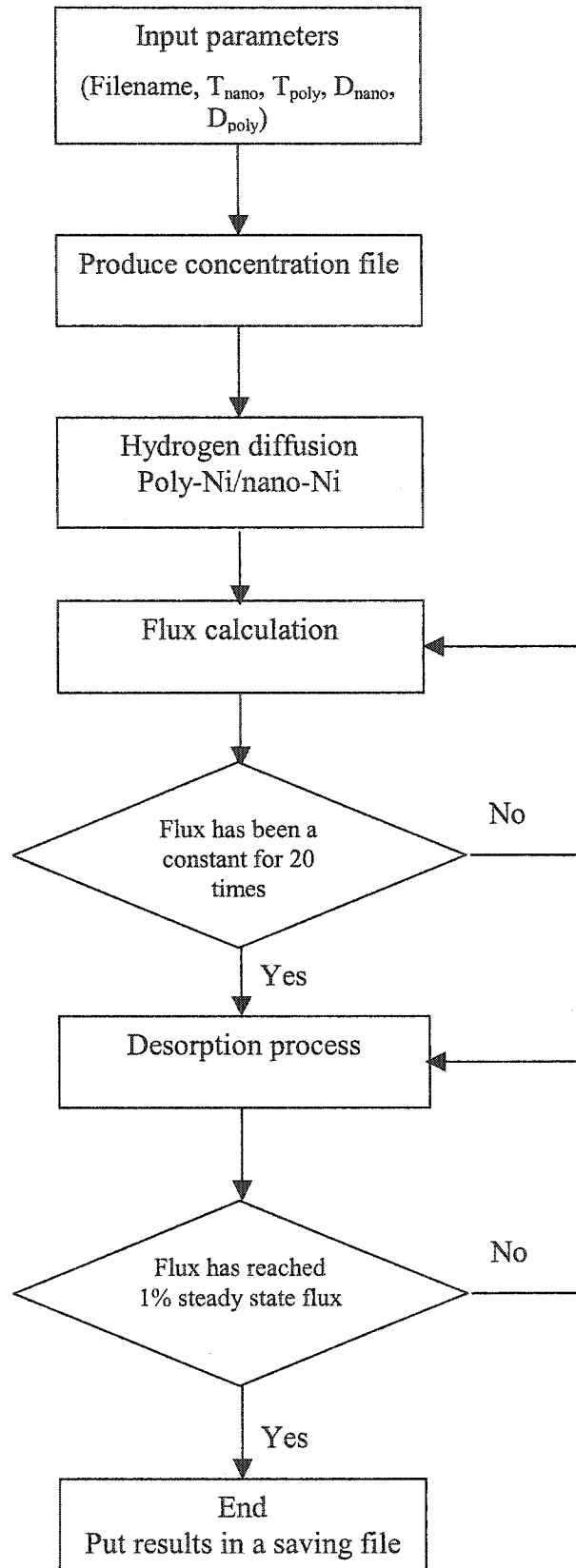


Fig. 8.6 Flow chart of hydrogen permeation simulation

8.4 Comparison of hydrogen permeation behaviors in two directions

In order to calculate the transient hydrogen permeation curve, diffusivity for a nano-Ni membrane and a poly-Ni membrane should be determined. The diffusivities for nickel membranes have been measured and shown in Table 8.1. Of course, diffusivity for the nano-Ni is dependent on grain size and the temperature measured. For qualitative simulation, only ratio of the nano-Ni layer and the poly-Ni layer diffusivity in a poly-

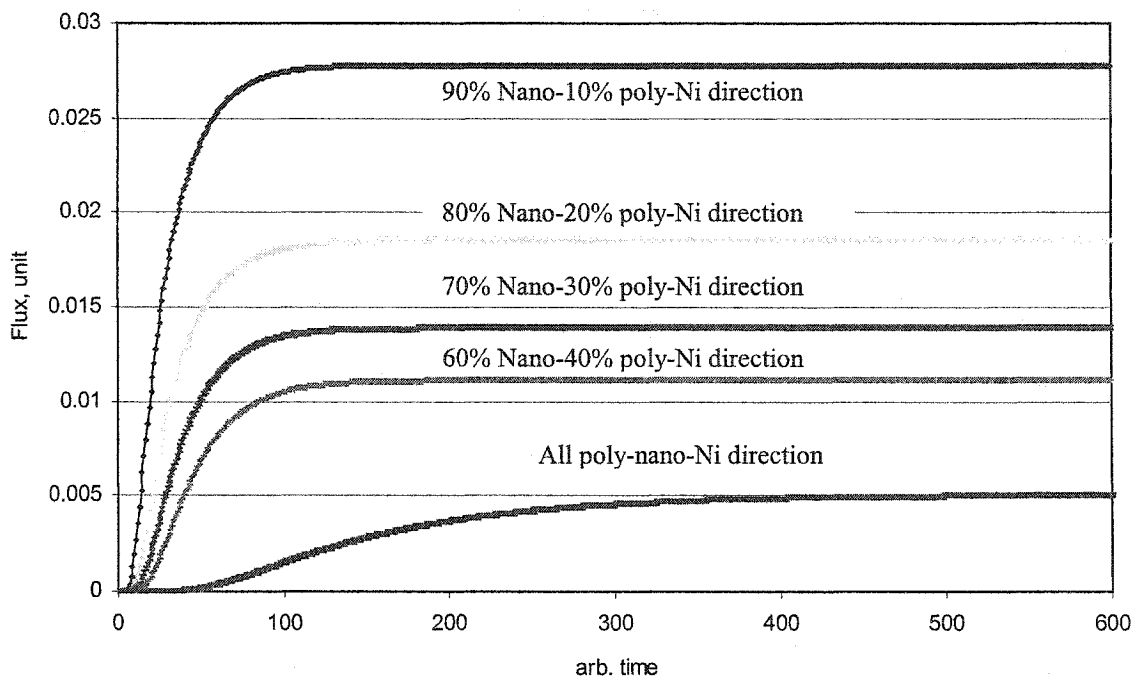


Fig. 8.7 Hydrogen buildup curves from the simulation approach for different ratios of nano-Ni layer and poly-Ni layer in a poly-nano-Ni membrane with NP charging and PN charging conditions

nano-Ni membrane is necessary. By changing the thickness ratio of the nano-Ni layer and the poly-Ni layer in poly-nano-Ni membranes, different hydrogen permeation curves have been obtained from simulation (Fig. 8.7). When charging from the nano-poly-Ni directions, not only the hydrogen flux of the composite membrane increases with increasing thickness of the nano-Ni layer, the diffusivity of the composite membrane also

increases. But hydrogen flux and diffusivity of the composite membrane are almost the same for different ratios of the nano-Ni layer and the poly-Ni layer when charging from another direction. In Fig. 8.7, permeation curves for all poly-nano-Ni membranes are overlapped together, which looks like one permeation curve. Comparing the present simulation results (Fig. 8.7) with the experimental curves (Fig. 8.2), it can be found that they are corresponding to each other. When charging from the nano-poly-Ni direction, steady state flux and diffusivity are correspondingly high. When charging from the poly-nano-Ni direction, steady state flux and diffusivity are low. After changing the thickness ratio of the nano-Ni layer and the poly-Ni layer in poly-nano-Ni membranes, different hydrogen decay curves have been obtained (Fig. 8.8). When charging from the nano-poly-Ni direction, hydrogen has been released quickly from the composite membrane even though the starting hydrogen flux is high for the nano-Ni as the 1st layer. For different ratios of the nano-Ni layer and the poly-Ni layer thickness, the membrane with the highest ratio of the nano-Ni layer decays fastest. When charging from the poly-nano-Ni direction, decay curves are almost the same for different ratios of the poly-Ni and the nano-Ni layer. Comparing the present model (Fig. 8.8) with the experimental results (Fig. 8.3), it can be found that they represent a similar trend of changes.

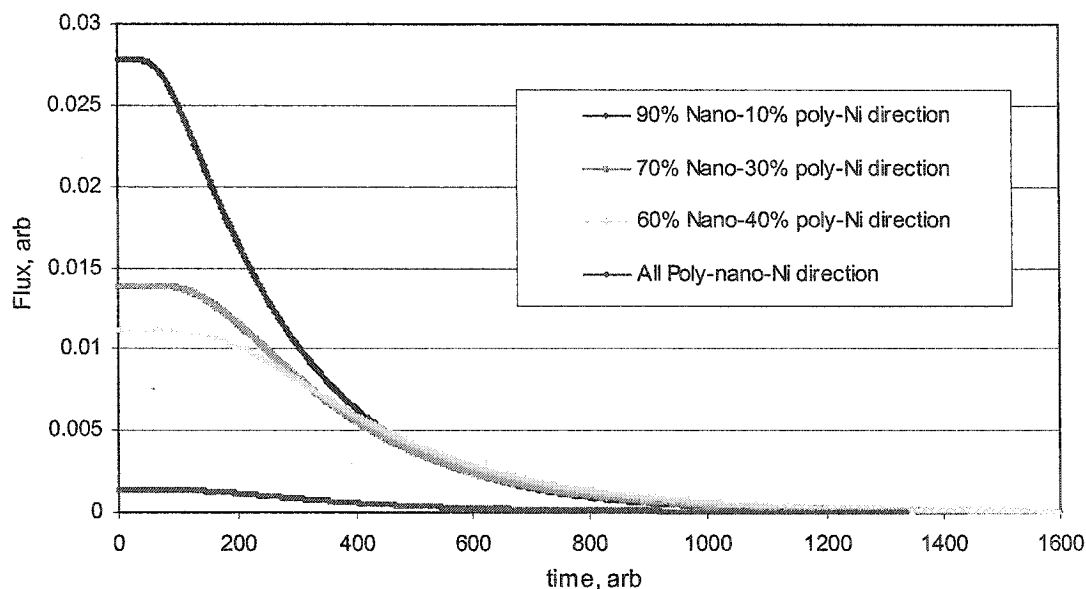


Fig. 8.8 Hydrogen decay curves from the simulation approach for different ratios of nano-Ni layer and poly-Ni layer in a poly-nano-Ni membrane with NP charging and PN charging conditions

8.5 Summary

1. When hydrogen is charged from the nano-Ni side (NP charging) of the nano-Ni and poly-Ni composite membrane, the permeation current rises rapidly. Then the membrane releases hydrogen quickly during decay. When hydrogen is charged from the poly-Ni side (PN charging) of the same composite membrane, the permeation current gradually rises and takes a longer time to reach a steady state. Then the membrane releases hydrogen slowly during decay. Also, the permeability of a nano-poly-Ni membrane for NP charging is eight times higher than that for PN charging. The hydrogen concentration of the poly-Ni side at the interface between poly-Ni and nano-Ni layers of the nano-Ni and poly-Ni composite membrane is lower than that of the nano-Ni side at the interface during PN charging. The hydrogen concentration of the nano-Ni side at the interface between nano-Ni and poly-Ni layers for the same

composite membrane is higher than that of the poly-Ni side at the interface during NP charging.

2. The diffusivity for charging from the nano-poly-Ni direction charging is two times higher than that from charging in the poly-nano-Ni direction charging for the same nano-poly-Ni membrane. The difference in diffusivity and permeability between the nano-poly-Ni direction and the poly-nano-Ni direction of the same composite membrane is similar to those between a single nano-Ni membrane and a single poly-Ni membrane. The diffusivity and permeability of nano-poly-Ni membranes are smaller than those for nano-Ni membranes, but larger than those for poly-Ni membranes. Using these findings, one can manipulate hydrogen permeation through composite membranes.
3. The hydrogen permeation model for a bilayer membrane is built to simulate hydrogen diffusion in the nano-Ni layer and the poly-Ni layer of a composite membrane for charging in two opposite directions. The model can generate hydrogen concentration profiles across the membrane. The experimental data is in good qualitative agreement with the model. The model can explain the anisotropic transport phenomena in bilayer membranes.

CHAPTER 9

CONCLUSIONS AND FURTHER RESEARCH

9.1 Summary and conclusions

1. The average grain size of palladium membranes is between 15-20 μm as determined from optical microstructure and OIM analysis. Heavy deformation produces high-density dislocations in Pd and Pd₇₇Ag₂₃ alloy. The stacking fault energy has significant influence on the deformation texture of Pd-Ag alloys. Pure palladium, which has a higher stacking fault energy value than silver, exhibits $\{111\}\langle 112\rangle$ texture. When the silver concentration is increased, $\{110\}\langle 112\rangle$ texture gradually appears and $\{111\}\langle 112\rangle$ texture gradually disappears in all Pd-Ag alloys. There is a large difference between annealed textures of Pd and Pd-Ag. The recrystallization texture after annealing at 850^oC is $\{113\}\langle 112\rangle$ for palladium and $\{113\}\langle 110\rangle/\langle 581\rangle$ for Pd₇₇Ag₂₃. When the silver concentration is increased, the recrystallization texture is changed.

2. Hydrogen permeation in the deformed palladium and Pd₇₇Ag₂₃ specimens has been delayed because hydrogen trap sites have been introduced by deformation. When the amount of deformation in palladium is increased, hydrogen permeation in palladium is delayed even more. The annealing of deformed palladium and Pd₇₇Ag₂₃ at 250⁰C reduces the number of trap sites, so permeation is faster than in the deformed metals. The annealing of deformed palladium and Pd₇₇Ag₂₃ at 850⁰C accelerates hydrogen diffusion. Recrystallization annealing reduces the number of trap sites and allows recovery of the hydrogen permeation characteristics in palladium and Pd-Ag alloy.
3. After deformation and annealing, palladium and Pd₇₇Ag₂₃ have different hydrogen decay characteristics. The annealed metals release hydrogen more rapidly than the deformed metals. The Pd₇₇Ag₂₃ alloy needs more time to release than palladium. The solubility in deformed palladium and Pd₇₇Ag₂₃ is increased by deformation. The trap densities in palladium rapidly increase from 20% to 50% deformation, and then increase slowly to $2.41 \times 10^{18} \text{ cm}^{-3}$. The trap density is $1.44 \times 10^{18} \text{ cm}^{-3}$ for deformed Pd₇₇Ag₂₃ alloy. The dislocations and local residual stress introduced by deformation are thought to be trapping sites for hydrogen.
4. A hydrogen-trapping model has been developed, which can explain the effect of trapping on hydrogen during permeation through metal membranes. The experimental data fit this model qualitatively. Using this model, one can also obtain trapping site distributions. The simulation shows trapping clearly and obtains results rapidly. During the simulation of the trapping, one can change three parameters at the same time: binding energy, temperature, and the volume of trapping sites. If a sample has some initial hydrogen concentration before charging, the model can still be used for

simulation of hydrogen permeation because the volume of the trap sites can be adjusted.

5. The average grain size of the electrodeposited nickel membrane is around $1.5 \mu\text{m}$. The nickel electrodeposits with a thickness up to $200\mu\text{m}$ exhibit a fiber texture containing two major components, the (100) and (110). While for low current densities, the (100) texture is dominant. The application of high deposition currents allows a strong (110) fiber texture component to grow. The texture transition takes place between 30 and $50\text{A}/\text{dm}^2$. By controlling the electroplating conditions, the texture of the deposits can be manipulated. After annealing at 800°C for 1h, the deposits with (100) texture develop (111) texture.
6. Hydrogen permeation through nickel depends on the texture of the nickel membranes. Diffusion coefficients increase as one moves from (001) to (011) and (111) textured samples. The diffusion coefficient of a sample without a dominant texture is lower than the values measured for the samples with (001), (110) and (111) textures. Diffusion coefficients of (001) and (011) polycrystalline membranes are higher than (001) and (011) single crystal membranes. However, in both cases the (011) diffusion coefficient is greater than the (001) diffusion coefficient.
7. By using absorption energies of (001), (011) and (111), the three basic planes in nickel, the adsorption energies for other orientations have been calculated using the weighted average method. The absorption energies for different orientations have been shown in the form of an inverse pole figure for the direction perpendicular to the specimen. Hydrogen permeation in single crystal metals is anisotropic. Different orientations of single crystal metals have different hydrogen absorption energies. For

(001), (011) and (111) the three basic planes in fcc nickel, the absorption energies are in decreased order, the highest being for (001) orientation. For textured samples, certain orientations contribute more than other orientations to hydrogen permeation. From the acknowledged absorption data for these three orientations and from bulk diffusivity differences for single crystal nickel, one can expect that different diffusion coefficients exist for nickel membranes with different textures.

8. When nanocrystalline nickel membranes have been annealed between 200⁰C and 400⁰C, diffraction peak broadening is reduced. After annealing between 500⁰C and 900⁰C, diffraction peaks become normal and grain size increases. After annealing at 900⁰C, some of the grains in the nickel membranes are larger than 70 μ m. Annealing between 200⁰C and 900⁰C yields a texture change in the nickel membrane from (100) fiber texture to (100) fiber texture with an additional (111) texture, and further annealing gives us only one recrystallization (111) texture. The differences in grain boundary character distribution (GBCD) of nickel membranes in general are not significant after annealing nanocrystalline nickel membranes from 200⁰C to 900⁰C. A slight increase in the number of high angle (45⁰-65⁰) grain boundaries is observed as the annealing temperature is increased. There is also a small decrease in the percentage of low (0⁰-15⁰) and middle angle (30⁰-45⁰) grain boundaries.
9. When the charging current is increased, the permeation efficiency for nano-nickel membranes decreases, but the diffusion coefficients and permeation currents increases. Diffusivity and permeation currents increase slowly and approach a steady value for charging currents higher than 0.5 mA. Increasing hydrogen supply in the entry surface increases the hydrogen diffusion coefficient.

10. The diffusivity of hydrogen is six times higher in polycrystalline membranes as compared to single crystal membranes, and increases six times again in nanocrystalline membranes. As the grain boundaries become a smaller portion of the sample after annealing at 800 °C and 900 °C, the grain size cannot affect the rate of hydrogen diffusion.
11. The proportion of low angle boundaries (LAB) increases as the amount of deformation in palladium increases from 20% to 50% and then to 82%. The annealing process reduces the proportion of low angle boundaries in palladium and Pd₇₇Ag₂₃ alloy. The samples of annealed palladium and Pd₇₇Ag₂₃ have higher diffusion coefficients than those of the deformed ones. The high intensity texture and proportion of low angle grain boundaries also contribute to a delay in hydrogen diffusion. After annealing, textures of palladium and Pd₇₇Ag₂₃ become weak. Also, the number of defects and the percentage of low angle grain boundaries are reduced, thus facilitating hydrogen diffusion.
12. The defect traps (mainly dislocations), texture and grain boundary misorientation distribution are microstructural factors influencing hydrogen diffusion in deformed palladium and Pd₇₇Ag₂₃ alloy. Overall, the presence of defect traps is considered to be the major factor that influences hydrogen diffusion in deformed palladium and Pd₇₇Ag₂₃ alloy. The hydrogen permeation for palladium and Pd₇₇Ag₂₃ membranes results from the combined influence of these three factors.
13. There are four major microstructural factors: deformation defects, grain size, texture and misorientation, which affect hydrogen permeation in metals. In the polycrystalline materials, effects on hydrogen permeation in descending order of

importance depend on: crystal defects, grain size, texture and grain misorientation.

The influence of grain boundaries on hydrogen permeation is greater in nanocrystalline than in polycrystalline materials.

14. When hydrogen is charged from the nano-Ni side (NP charging) of the nano-Ni and poly-Ni composite membrane, the permeation current rises rapidly. Then the membrane releases hydrogen quickly during decay. When hydrogen is charged from the poly-Ni side (PN charging) of the same composite membrane, the permeation current gradually rises and takes a longer time to reach a steady state. Then the membrane releases hydrogen slowly during decay. Also, the permeability of a nano-poly-Ni membrane for NP charging is eight times higher than that for PN charging. The hydrogen concentration of the poly-Ni side at the interface between poly-Ni and nano-Ni layers of the nano-Ni and poly-Ni composite membrane is lower than that of the nano-Ni side at the interface during PN charging. The hydrogen concentration of the nano-Ni side at the interface between nano-Ni and poly-Ni layers for the same composite membrane is higher than that of the poly-Ni side at the interface during NP charging.
15. The diffusivity from the nano-poly-Ni direction charging is two times higher than that from the poly-nano-Ni direction charging for the same nano-poly-Ni membrane. The difference in diffusivity and permeability between the nano-poly-Ni direction and the poly-nano-Ni direction of the same composite membrane is similar to those between a single nano-Ni membrane and a single poly-Ni membrane. The diffusivity and permeability of nano-poly-Ni membranes are smaller than those for nano-Ni

membranes, but larger than those for poly-Ni membranes. Using these findings, one can manipulate hydrogen permeation through composite membranes.

16. The hydrogen permeation model for a bilayer membrane is built to simulate hydrogen diffusion in the nano-Ni layer and the poly-Ni layer of a composite membrane for two-direction charging conditions. The model can generate hydrogen concentration profiles across the membrane. The experimental data are in good qualitative agreement with the model. The model can explain the anisotropic transport phenomena in bilayer membranes.

9.2 Contribution to original knowledge

1. Proposing a new computer hydrogen trapping model:

A computer hydrogen-trapping model has been proposed and developed, which can explain effects of trapping on hydrogen permeation through thin membranes. The experimental data are in qualitative agreement with the model. If a sample has initial hydrogen concentration before charging, the model can still be used for simulation of hydrogen permeation by adjusting the trapping volume.

2. Designing and developing new multilayer membranes with strong anisotropic permeation characteristics for hydrogen:

New multilayer membranes with a nano-Ni layer and a poly-Ni layer have been designed and developed, which have strong anisotropic permeation characteristics for hydrogen. New multilayer membranes can be used to manipulate hydrogen permeation rate and flux in a variety of engineering applications.

3. Proposing hydrogen permeation model of bilayer membranes:

Experimental data obtained from the nano-Ni and poly-Ni membranes allowed to develop a computer model of hydrogen transport in two directions through bilayer membranes. This model accounts for different hydrogen permeation characteristics of nano-Ni and poly-Ni layers.

4. Discovery of effect of texture on hydrogen permeation in metal membranes:

Hydrogen permeation through nickel depends on textures of nickel membranes. Diffusion coefficients increase as one moves from (001) to (011) and (111) textured samples. The Diffusion coefficient of a sample without a dominant texture is lower than the values measured for the samples with (001), (110) and (111) textures.

5. Description grain boundary character distribution (GBCD) of the annealed nano-Ni:

Grain boundary character distribution in the annealed nano-Ni materials with different grain sizes was determined using previously developed statistical method.

6. Determining microstructural factors controlling hydrogen permeation in membranes:

The presented research will allow us to understand better a role of microstructural factors in hydrogen permeation through metal membranes, in particular a role of deformation defects, grain size, texture and grain misorientation.

7. The application of Orientation imaging microscopy (OIM) in palladium:

In this research, the state-of-the-art technique of surface imaging by OIM, was applied for the first time to view palladium macrostructures, which is difficult to analyze when using optical microscopy.

9.3 Suggestions for future work

1. Research on microstructural factors of hydrogen permeation in metal membranes

Until now, microstructural factors of hydrogen permeation in metal membranes have been systematically investigated. More quantitative study of these factors should continue. Furthermore, one should represent microstructural factors using quantitative methods.

2. Further experimental study to explain hydrogen permeation of multilayer:

The present study provides experimental data with anisotropic hydrogen permeation for nano-Ni and poly-Ni bilayer membranes. Hydrogen permeation in multilayer membranes with two different layers should be further investigated. For example, sandwich membranes like nano-Ni/poly-Ni/nano-Ni three layers and poly-Ni/nano-Ni/poly-Ni three layers should be isotropic when changing from two opposite directions. A four-layer membrane like nano-Ni/poly-Ni/nano-Ni/poly-Ni should have stronger anisotropic permeation behavior and should also have different permeation when changing from two opposite directions. Following this logic, there are isotropic hydrogen permeation behaviors if multilayer membranes have odd layers and consist of only two different kinds of films.

3. Computer modeling hydrogen permeation through multilayer membranes:

Explaining hydrogen permeation through multilayer membranes more precisely is necessary in order to develop a general computer model, which includes different microstructures. This model should incorporate the most important microstructural characteristics of the films like texture, grain boundary character distribution, dislocation density, and numbers of trapping sites. This will allow simulating the

Chapter 9: Conclusions and Further Research

effects of microstructural factors and layer-structures on hydrogen permeation. Furthermore, such model should allow us to obtain more quantitative agreement with experiments.

REFERENCE

1. Alefeld, G. and Volkl, J. (eds.), 1978, Hydrogen in Metals, I and II: Topics in Applied Physics, Vol. 28 & 29 (Springer-Verlag, Berlin)
2. Amblard, J., Epelboin, I., Froment, M., and Maurin, G. 1979, *J. Appl. Electrochem.*, **9**, 244.
3. Amblard, J., Froment, M., Maurin, G., Spyrellis, N., and Trevisansouteyrand, E. 1984, *Electrochem. Acta*, **28**, 909.
4. Andrew, P. L. and Haasz, A. A., 1991, *J. Less-Comm. Met.*, **172-174**, 732.
5. Arantes, D. R., Huang, X. Y., Marte, C. and Kirchheim, R., 1993, *Acta Metall.*, **41**, 3215.
6. Archer, M. D. And Grant, N. C., 1984, *Proc. R. Soc. Lond.*, **A395**, 165.
7. Armor, J. N., 1992, *CHEMTECH*, **9**, 557.
8. Armor, J. N., 1995, *Catalysis Today*, **25**, 199.
9. Atrens, A, Mezzanotte, D., Fiore, N. F. and Genshaw, M. A., 1980, *Corrosion Science*, **20**, 673.
10. Barbieri, G. and Di Maio, F. P., 1997, *Ind. Eng. Chem. Res.*, **36**, 2121.
11. Baskes, M. I. and Vitek, V., 1985, *Metall. Trans.*, **16A**, 1625.
12. Bath, B. and I. M. Bernstein, 1971, *Metall. Trans*, **2**, 2972.
13. Behm, R. J., Christmann, K. R. and Ertl, G., 1980, *Surf. Sci.*, **99**, 320.
14. Bellanger, G. and Rameau, J. J., 1997, *Fusion Technology.*, **32**, 94.
15. Bergenstof, C., Nielsen, A., Horsewell, Ostergaard, M. J. L., 1997, *J. Applied Electrochemistry*, **27**, 839.
16. Bernardini, J. and P. Gas, 1997, *Defect and Diffusion Forum*, **143-147**, 1343.
17. Biswas, D. R., 1986, *J. Mater. Sci.*, **21**, 2217.
18. Boes, N. and Zuchner, H., 1976, *J. Less-Common Met.*, **49**, 223.
19. Brass, A. M. and Collet-Lacoste, J. R., 1998, *Acta Metall.*, **46**, 869
20. Brass, A. M. and Collet-Lacoste, J. R., 1996a, *Hydrogen Effects in Materials*, A. W. Thompson and N. R. Moody Eds., TMS, P189-203
21. Brass, A. M., and Chanfreau, A., 1996b, *Acta Metall.*, **44**, 3823
22. Brass, A. M., and Chene, J., 1998, *Mater. Sic. Eng.*, **A242**, 210

Reference

23. Brass, A. M., Chanfreau, A. and Chene, J., 1990, *Hydrogen Effects on Materials Behavior*, TMS, P19.
24. Bruzzoni, P. and Garavaglia, R., 1992, *Corrosion Sci.*, **33**, 1797
25. Bryden, K. J. and Ying, J. Y., 1995, *Materials Sci. Eng.*, **A204**, 140.
26. Bryden, K. J. and Ying, J. Y., 1997, *Nanostructured Materials*, **9**, 485.
27. Bucur, R. V., N. O. Ersson, X. Q. Tong, 1991, *J. Less-Common Met.*, **172-174**, 748.
28. Bunge, H. J., 1982, *Texture Analysis in Materials Science*, Butterworths
29. Cao, Y., Szpunar, J. A. and Shmayda, W., 2002, *Defect and Diffusion Forum*, **203-205**, 211
30. Caskey, G. R. and Pillinger, W., 1975, *Met. Trans.*, **6A**, 467.
31. Cattania, M. G., Christmann, K., Penka, V. and Ertl, G., 1983, *Gazz. Chim. Ital.*, **113**, 433.
32. Chatterjee, S. S., Ateya, B. G. and Pickering, H. W., 1978, *Met. Trans.*, **9A**, 389
33. Christmann, K., Behm, R. J., Ertl, M. A., Van Hove, W. H. and Weinberg, J., 1979, *J. Chem. Phys.*, **70**, 4168.
34. Christmann, K., Schober, O., Ertl, G. and Neumann, M., 1974, *J. Chem. Phys.*, **60**, 4528.
35. Conrad, H., Ertl, G. and Latta, E. E., 1974, *Surf. Sci.*, **41**, 435.
36. Cullity, B.D. and Stock, S.R., 2001, *Elements of X-Ray Diffraction*, Prentice Hall Upper Saddle River, NJ
37. Czerwinski, A. , Czauderna, M., Maruszczak, G., Kiersztyn, I., Marassi, R. and Zamponi, S., 1997, *Electrochimica Acta*, **42**, 81.
38. Czerwinski, F. and Szpunar, J. A., 1999, *Corrosion Science (USA)*, **41**, 729
39. Daw, M. S. and Baskes, M. I., 1984, *Phys. Rev. B*, **29**, 6443.
40. Dederichs, P. H., K. Schroeder and R. Zeller, 1980, *Point Defects in Metals II*, (Springer-Verlag, New York), p177.
41. Delpancke, J. L., Winand, R., Dierickx, M., Lifschitz, L., 1993, *J. Electrochem. Soc.*, **140**(10), 2800.
42. DeLuccia, J. J. and Berman, D. A., 1981, *Electrochemical Corrosion Testing*, ASTM STP 727, F. Mansfeld and U. Bertocci, Eds., P 256-273
43. Devanathan, M. A. V. and Stachurski, Z., 1962, *Proc. Roy. Soc.*, **A270**, 90.
44. Dini, J. W., 1997, *Mater. and Manufacturing Processes*, **12**, 437.
45. Dong, W., Ledentu, V., Sautet, Ph., Eichler, A. and Hafner, J., 1998, *Surface Science*, **411**, 123.
46. Early, J. G., 1997, *Acta Metall.*, **26**, 1215.

Reference

47. Ebisuzaki, Y., Kass, W. J. and O'Keeffe, M., 1967, *J. Chem. Physics*, **46**, 1378.
48. El-Sherik, A. M. and Shirkhazadeh, M., 1992, *Corrosion Science*, **48**, 1001.
49. El-Sherik, A. M., Erb, U., Page, J., 1996, *Surface and Coating Tech.*, **88**, 70.
50. Eriksson, M. And Ekedahi, L., 1998, *J. Applied Physics*, **83**, 3947.
51. Flanagan, T. B. and Lynch, J. F., 1976, *J. Less-Common Met.*, **49**, 25.
52. Flanagan, T. B., Gross, G. and Clewley, J. D., 1977, 2nd Int. Cong. on Hydrogen in Metals, Paris, France, 1C3
53. Fleischmann, M. and Thirsk, H. R., 1963, *Advan. Electrochem. Eng.*, **3**, 123.
54. Fleischmann, M. ed, 1977, *Electrocrystallization, Nucleation and Phase Formation*, Faraday Symposia of the Chemical Society, No. 12
55. Flynn, C. P., 1964, *Phys. Rev.*, **133**, A587.
56. Fukai, Y., 1993, *The Metal-Hydrogen System: Basic Bulk Properties*, Springer-Verlag, Berlin, New York, P231.
57. Gleiter, H. and B. Chalmer, 1972, *Progress in Materials Science*, **16**, 90.
58. Govind, R., Atnoor, D., Zhao, R., 1991, *Key Engineering Materials*, **61-62**, 319.
59. Hamilton, J. C. and Swansiger, W. A., 1996, *Hydrogen Effects in Materials*, A. W. Thompson and N. R. Moody Eds., TMS, P271-281
60. Harris, I. R., Dillamore, I. L., Smallman, R. E. and Beeston, B. E. P., 1968, *Philosophical Magazine*, **14**, 325.
61. Harris, T. M. and R. M. Latanision, 1991, *Metall. Trans.*, **22A**, 351.
62. Harrision, L.G., 1961, *Trans. Faraday Soc.*, **57**, 1191.
63. Hart, E., 1957, *Acta Metal.*, **5**, 597.
64. Heitzinger, J. M., Avoyan, A. and Koel, B. E., 1993, *Surface Science.*, **294**, 251.
65. Heuser, B. J. and King, J. S., 1998, *Metall. Trans.*, **29A**, 1593.
66. Hirscher, M., Mossinger, J. and Kronmuller, H, 1995, *J. Alloys Comp.*, **231**, 267.
67. Hirth, J. P., 1980, *Metall. Trans.*, **11A**, 861.
68. Hong, K., 2001, *Journal of Alloys and Compounds*, **321**, 307.
69. Hu, H., Cline, R. S. and Goodman, S. R., 1961, *J. Applied Physics*, **32**, 1392.
70. Huang, X.Y., Mader, W. and Kirchheim, R. 1991 *Acta Metall. Mater.*, **39**, 893.
71. Huber, B. and Sicking, G., 1978, *Phys. Stat. Sol. (a)*, **47**, K85.
72. Hughes, D., 2001, *Surface and Interface Analysis*, **31**, 560.
73. Hull, D., 1975, *Introduction to Dislocation*, p25, Oxford, Pergamon Press
74. Hutchings, R. B., Turnbull, A. and May, A.T., 1991, *Scr. Metall.*, **28**, 2657.

Reference

75. Hutchings, R. B., Ferriss, D. H. and Turnbull, A., 1993, *British Corrosion Journal*, **28**, 309.
76. Inoue, H. and Inakazu, N., 1988, *ICOTOM 8*, The Metallurgical Society/AIME, pp. 997
77. Iyer, R. N. and Pickering, H. W., **20**, *Annu. Rev. Mater. Sci.*, 299.
78. Janssen, S., Natter, H; Hempelmann, R., Striffler, T., Stuhr, U., Wipf, H., Hahn, H and Cook, J.C., 1997, *Nanostructured Materials*, **9**, 579.
79. Johnson, H. H., 1988, *Metall. Trans.*, **19A** , 2371.
80. Johnson, O. W., 1964, *Phys. Rev.*, **136**, A248.
81. Karayannis, H.S. and Patermarakis, G., 1995, *Electrochemica Acta*, **40**, 1079.
82. Kasuya, T. and Hashiba, Y., 1999, *J. Phys. D: Appl. Phys.*, **32**, 2674.
83. Katsuta, H., Farraro, R. J. and McLellan, R. B., 1979, *Acta Metall.*, **27**, 1111.
84. Kikuchi, E., Nemoto, Y., Kajiwara, Uemiya, S. and Kojima, T., 2000, *Catalysis Today*, **56**, 75.
85. Kirchheim, R. and McLellan, R. M., 1980, *J. Electrochem. Soc.*, **127**, 2419.
86. Kirchheim, R., Huang, X. Y., Mutschele, T., 1990, *Hydrogen Effects on Materials Behavior*, N. R. Moody K. and A. W. Thompson Eds., TMS, P85-99
87. Kirchheim, R., Mutschele, T and Kieninger, W., 1988, *Mater. Sci. Eng.*, **99**, 457.
88. Kollia, C. Loizos, Z. and Spyrellis, N., 1991, *Surf. Coat. Technol.*, **45**, 155.
89. Kresse, G. and Hafner, J., 2000a, *Surface Science*, **459**, 287.
90. Kresse, G., 2000b, *Phys. Rev. B*, **62** , 8295.
91. Kumnick, A. J. and Johnson, H. H., 1974, *Metall. Trans.*, **5A**, 1199.
92. Kumnick, A. J. and Johnson, H. H., 1975, *Metall. Trans.*, **6A**, 1087.
93. Lalueze, R. , Gillard, P. and Pijolat, C., 1988, *J. Less-Comm. Metals*, **138**, 179.
94. Latanision, R. and Kurkela, M, 1983, *Corrosion NACE*, **39**, 174.
95. Lee, M. W. and Glosser, R., 1985, *J. Appl. Phys.*, **57**, 5236.
96. Lee, S. and Lee, J., 1985, *Metall. Trans.*, **17A**, 181.
97. Lewis, F. A., 1996, *Int. J. Hydrogen Energy*, **216**, 461.
98. Lewis, F., 1967, *The Palladium Hydrogen System*, Academic Press, London
99. Li, D. Y. and Szpunar, J. A., 1997, *Electrochimica Acta*, **42**, 47.
100. Luu, W., Kuo, H. and Wu, J., 1997, *Corrosion Sci.*, **39**, 1051.
101. Mackor, A., Kreuk, C. W. and Schoonman, J., 1988, *Hydrogen Embrittlement: Prevention and Control*, ASTM STP 962, Raymond, L. Ed., P90-97

Reference

102. Manohar, M. and Wilde, B. E., 1995, *Corrosion Science.*, **37**, 607.
103. Marte, C. and Kirchheim, R., 1997, *Scripta Mater.*, **37**, 1171.
104. Martinez-Madrid, M., Chan, S. L. and Charles, J. A., 1985, *Mater. Sci. Tech.*, **1**, 454.
105. *Materials Perform*, 1983, **(2)**, 57.
106. Matsushima, I., Uhlig, H. H., 1966, *J. Electrochem. Soc.*, **113**, 555
107. McNabb, A. and Foster, P. K., 1963, *Trans. TMS-AIME*, **227**, 618.
108. Merchant, H. D., 1995, *Defect Structure, Morphology and Properties of Deposits*, Merchant, H. D. ed. TMS, p1
109. *Metals Handbook: Vol 2, 9th edition*, 1980, ASM, Metals Park, Ohio, USA, P699-705
110. Mirzaev, D. A., Sokolova, A. A., Rushits, S. V. and Rudenko, V. K., 1996, *The Physics of Metals and Metallography*, **82**, 553.
111. Molnar, A., Smith, G. V. and Bartok, M., 1989, *Adv. Catal.* **36**, 329.
112. Morawiec, A., J. A. Szpunar and D. C. Hinz, 1993, *Acta Metall. Mater.*, **41**, 2825.
113. Murr, L. E., 1975, *Interfacial Phenomena in Metals and Alloys*, Addison-Wesley Publishing Co., pp 346-7
114. Mutschele, T. and Kirchheim, R., 1987a, *Scr. Metall.*, **21**, 135.
115. Mutschele, T. and Kirchheim, R., 1987b, *Scr. Metall.*, **21**, 1101.
116. Myers, S. M., Picraux, S. T. and Stoltz, R. E., 1979, *J. Appl. Phys.*, **50**, 5710.
117. Nani, L. and T. K. Nambodhiri, 1972, *J. Electrochem. Soc.*, **119**, 691.
118. Natter, H., Krajewski, T. and Hempelmann, R., 1996, *Ber. Bunsenges. Phys. Chem.*, **100**, 55
119. Nelson, H. G., 1984, *Hydrogen Energy Progress V*, Eds. Veziroglu and Talor, Pergamon Press, New York, 1841.
120. Neumann, P., 2000, *Filtration and Separation*, (7-8), 26.
121. Nishikawa, M., Shiraishi, T., Kawamura, Y. and Takeishi, T., 1996, *J. Nuclear Sci. & Technol.*, **33**, 774.
122. Oriani, R. A., 1970, *Acta Metall.*, **18**, 147.
123. Palumbo, G., Doyle, El-Sherik, A. M., Erb, U., Aust, K. T., 1991, *Scripta Mater.*, **25**, 679.
124. Park, J., Bennett, T., Schwararzmman, J. and Cohen, S. A., 1995, *J. Nucl. Mater.*, **220-222**, 827.
125. Parthasarathy, N. V., 1974, *Metal Finishing*, **72(8)**, 36.
126. Paul, J. F. and Sautet, P., 1996, *Surface Sci.*, Vol. **356**, L403.

Reference

127. Perng, T. P. and Altstetter, C. J., 1988, Metall. Trans., **19A**, 1187,
128. Pick, M. A. and Green, M. G., 1981, J. Less-Common Metals, **73**, N1.
129. Pietrzak, R., Szatanik, R. and Szuszkiewicz, M., 1997, Defect and Diffusion Forum, **143-147**, 951.
130. Pressouyre, G. M. and Bernstein, I. M., 1978, Metall. Trans., **9A**, 1571.
131. Pyun, S. and Yoon, Y., 1996, Hydrogen Effect in Materials, Eds. Thompson, A. W. and Moody, N. R., TMS, P261-269
132. Pyun, S., Lee, W. and Yang, T., 1997, Thin Solid Films, **311**, 183.
133. Rao, P. R. and Rao, K. K., 1968, J. Applied Physics, **39**, 4563.
134. Rath, B. B. and Bernstein, I. M., 1971, Metall. Trans., **2**, 2972.
135. Reed-Hill, 1973, Phys. Met. Principles 2nd Ed., p268
136. Revay, L., 1975, Electrodeposition and Surface Treatment, **3**, 139.
137. Robertson, W. M., 1973, Z. Metallkde., **64**, 436.
138. Rodrigues, J. A. and Kirchheim, R., 1983, Script. Metall., **17**, 159.
139. Ross, D. K. and Stefanopoulos, K. and Kemali, M., 1999, J. Alloy and Comp., **293-295**, 346.
140. Sakamoto, Y., S. Hirata and H. Nishikawa, 1982, J. Less-Common Met., **88**, 387.
141. Savitskii, E. M., 1969, *Palladium Alloys*, Primary Sources, New York, pp1-40.
142. Schmid, E. and Boas, W., 1950, *Plasticity of Crystals*, Chapman & Hall Ltd, London, pp299-300.
143. Schmidt, W. and Lucke, K., 1979, Texture of Cryst. Solids, **3**, pp85-112
144. Schmitz, G., Kesten, Ph. and Kirchheim, R., 1998, Phys. Rev. B, **58**, 7333
145. Schuldiner, S. and Hoare, J. P., 1956, J. Electrochem. Soc., **103**, 178.
146. Shewmon, P., 1989, *Diffusion in Solids*, 2nd Edition, TMS, p61-68.
147. Sibley, P. and Brook, P. A. (1973-74) *Electrodeposition and Surface Treatment*, **2**, pp177-190
148. Song, R. and Pyun, S., 1990, J. Electrochem. Soc., **137**, 1051.
149. Stafford, S. and McLellan, R., 1974, Acta Metall., **22**, 1463.
150. Stuhr, U., Striffler, T., Wipf, H., Natter, H., Wettmann, B., Janssen, S., Hempelmann, R. and Hahn, H., 1997, J. Alloys and Comp., **253-254**, 393.
151. Takano, N., Murakami, Y. and Terasaki, F., 1995, Scr. Metall. Mater., **32**, 401.
152. Tosti, S., Bettinali, Violante, V., 2000, Inter. J. Hydrogen Energy, **25**, 319.
153. Tsubakino, H. and Nishimura, R., 2000, Corrosion Eng., **49**, 261.

Reference

154. Turnbull, A., Ballinger, R. G., Hwang, I. S. and Gates, R. M., 1990, Hydrogen Effects on Materials Behavior, N. R. Moody K. and A. W. Thompson Eds., TMS, P121-131
155. Tyson, W. R., 1976, *J. Appl. Phys.* **47**, 459.
156. Uemiyama, S., Matsuda, T and Kikuchi, E., 1991, *J. Membrane Science*, **56**, 315.
157. Van Leeuwen, H., 1973, *Corrosion*, **29**, 197.
158. Vermyea, D. A., 1956, *J. Chem. Phys.*, **25**, 1254.
159. Vermyea, D. A., 1963, *Adv. Electrochemistry and Electrochemical Eng.* **3**, 1254.
160. Volkl, J. and Alefeld, G., 1975, *Diffusion in Solids: Recent Developments*, A. S. Nowick and J. J. Burton eds, Academic Press, New York, P231
161. Walsh, F. C. and Herron, M. E., 1991, *J. Phys. D: Appl. Phys.*, **24**, 217.
162. Walsh, L. H., Feilchenfeld, N. B. and Schwarz, J. A., 1992, *J. Vacu. Sci. Tech.*, **A10**, 1493.
163. Weil, R., 1987, *Plating & Surface Finishing*, **74**(12), 70.
164. Wert, C. A., 1983, *Ann. Res. Mater. Sci.*, **13**, 139.
165. Williamson, G. K. and Smallman, R. E., 1956, *Philosophical Mag.*, **1**, 34.
166. Winand, R., 1992, *Hydrometallurgy*, **29**, 567.
167. Winand, R., Ham, P., Colin, R and Milojevic, D., 1997, *J. Electrochem. Soc.*, **144**, 428.
168. Wipf, H. (ed.), 1997, *Hydrogen in Metals III: Topics in Applied Physics*, Vol. **73** (Springer-Verlag, Berlin,)
169. Wu, H., 1994, *J. Appl. Phys.* **75**, 814.
170. Yao, Y. and Cahoon, J., 1991, *Acta Metall. Mater.*, **39**, 119.
171. Yen, S. K., 1999, *Corrosion Science*, **41**, 2031.
172. Yoon, Y. G. and Pyun, S., 1996, *Journal of Alloys and Compounds*, **243**, 45.
173. Yoshihara, M. and McLellan, R. B., 1988, *Acta Metall.*, **36**, 3225.
174. Young, G. A. and Scully, J. R., 1998, *J. Acta Mater.*, **46**, 6337.
175. Yu, C. L. and Perng, T.P., 1991, *Acta Metall. Mater.*, **39**, 1091.
176. Zaman, J. and Chakma, A., 1994, *Journal of Membrane Science.*, **92**, 1.